

DISSERTATION

THE PATH FROM INJURY TO DEGENERATION: MULTI-MODAL
CHARACTERIZATION OF CHRONIC ROTATOR CUFF DEGENERATION

Submitted by

James W. Johnson

Department of Mechanical Engineering

In partial fulfillment of the requirements

For the Degree of Doctor of Philosophy

Colorado State University

Fort Collins, Colorado

Fall 2021

Doctoral Committee:

Advisor: Kirk C. McGilvray

Christian Puttlitz

Soham Ghosh

Jeremiah Easley

Copyright by James Walter Johnson 2021

All Rights Reserved

ABSTRACT

THE PATH FROM INJURY TO DEGENERATION: MULTI-MODAL CHARACTERIZATION OF CHRONIC ROTATOR CUFF DEGENERATION

Rotator cuff tendon tears are a prevalent issue worldwide; tears to these tendons can reduce arm mobility, cause pain, and decrease quality of life. Unfortunately, rotator cuff tendon tear repair surgeries experience unacceptable failures rates, with comorbidities such as age, chronic rotator cuff degeneration, or osteoporosis exacerbating these failures. The etiology of chronic degeneration is not fully understood, and there are no therapies or treatment capable of reversing or healing that condition. Furthermore, research is hindered due to the inability of current large animal translational models to faithfully recapitulate the wide range of changes noted in chronic degeneration.

With that in mind, this work sought to improve the understanding of chronic rotator cuff degeneration through development of a clinically translatable large animal model and study of the injury and degeneration cascade. Specifically, this work has five components that will contribute to this body of knowledge. The first aim was to generate a model through transection of one half of the width of the tendon; unfortunately, this was found to result in differential changes on the two halves of the tendon that did not match the embodiment of changes seen clinically. The inadequacy and learnings from this model led to the generation of aims two and three. It has been hypothesized that chronic degeneration can result from untreated partial tears that are not diagnosed or treated with any conservative treatment. Aim 2 was focused on generating a chronic

degeneration model through a clinically relevant bursal-side partial tear. Whereas Aim 3 was focused on creating a similar model without damaging the tendon insertion, providing the opportunity to screen therapies intended at halting or reversing the degeneration cascade. Aim 4 involved assessing tendons in an ovine model of osteoporosis for signs of degeneration as a means of determining the underlying cause for increased prevalence of rotator cuff repair failure in patients with osteoporosis. Aim 5 included characterization of the biomechanical, histological, and gene expression changes in cadaveric human rotator cuff tendons across a spectrum of ages as a means of better understanding the manifestation of chronic degeneration with the human rotator cuff. This aim was utilized as positive validation of the ovine models and as a means to generate design targets for repair scaffold mechanical properties. Aim 6 entailed generating a preliminary design of a scaffold capable of recapitulating the biomechanical properties of the healthy human supraspinatus tendons tested in Aim 5. Together, these proposed Aims provide new models of chronic rotator cuff degeneration, unique and novel data illuminating the multifactorial degeneration cascade in humans, and a prototype scaffold aimed at improving repair prognosis.

DEDICATION

To my wife, Laura. This work would not have been possible without your ceaseless support and love.

TABLE OF CONTENTS

ABSTRACT	ii
DEDICATION.....	iv
LIST OF FIGURES	x
LIST OF TABLES	xvii
LIST OF EQUATIONS.....	xviii
Chapter 1- Background	1
Rotator Cuff Tendon Injuries and Healing Dysfunction	1
Rotator Cuff Tendon Anatomy	2
Tendon.....	3
Material Composition and Macrostructure	3
Tendon Biomechanics	7
Hyperelasticity	7
Viscoelasticity	8
Modeling the Viscoelastic and Hyperelastic Properties of Tendons.....	9
Chronic Rotator Cuff Degeneration	10
Osteoporosis as a Risk Factor for Rotator Cuff Repairs	13
Current Treatment Strategies and Future Improvement Opportunities.....	14
Animal Models of Chronic Rotator Cuff Degeneration.....	15
Rodent and Small Animal Models	16
Canine Models	17
Non-Human Primate Models	17
Ovine Models	18
Summary.....	18

Specific Aims.....	20
Chapter 2- Partial Infraspinatus Tendon Transection as a Means for the Development of a Translational Ovine Chronic Rotator Cuff Disease Model ¹	25
Background.....	25
Materials and Methods	27
Human ‘Model’ – Tissue Collection	27
Ovine Model – Surgical Procedure	28
Surgical Assessment after 6 or 12 Weeks of Healing	31
Histological Analysis.....	32
Results	33
Reattachment of Medial Half of Tendon	33
Histology Results	34
Discussion.....	41
Chapter 3- Enthesis Trauma as a Means for the Development of Translatable Chronic Rotator Cuff Degeneration in an Ovine Model.....	44
Background.....	44
Methods	47
Human tissue collection.....	47
Ovine model – surgical procedures	48
Biomechanical testing.....	50
Histological analysis.....	51
Histomorphological assessment of collagen fiber alignment	51
RNA sequencing	52
Statistical analysis	53
Results	54
Mechanical Testing	54

Histopathology Results	58
Histomorphological assessment of collagen fiber alignment	60
RNA sequencing	60
Correlation Analysis	64
Conclusions.....	66
Chapter 4- Tendon Midsubstance Trauma as a Means for the Development of Translatable Chronic Rotator Cuff Degeneration in an Ovine Model	72
Background.....	72
Methods	74
Ovine Models – Surgical Procedure.....	74
Biomechanical Testing	77
Histological Analysis.....	78
Histomorphological assessment of collagen fiber alignment and intramuscular adipose content.....	79
RNA sequencing	80
Statistical analysis	81
Results	81
Biomechanical Results	82
Histology Results	85
Histomorphology Results	87
RNA sequencing	88
Correlation Analysis.....	91
Conclusions.....	94
Chapter 5- Bisphosphonate Impacts Tendon Mechanical Degradation in An Ovine Model of Osteoporosis	100
Introduction.....	100

Materials and Methods	102
Ovine OP Model Development	102
Tendon Mechanical Analysis	103
Bone μ CT Analysis	104
Histomorphological Analysis	105
Histopathological analysis	107
Viscoelastic Modeling	109
Statistical analysis	111
Results	112
Micro-CT	112
Histomorphological assessment of collagen fiber alignment	115
Histopathology Results	116
Viscoelastic Modeling	119
Correlation Analysis	124
Discussion	127
Conclusions	132
Chapter 6- Form and Function: Biomechanical, Pathological, and Gene Expression Changes Secondary to Aging In The Human Rotator Cuff	134
Introduction	134
Materials and Methods	136
Tendon Dissection Procedure	136
Tendon Biomechanical Testing Procedures	136
Viscoelastic Modeling	137
Histomorphological Analysis	140
Histopathological analysis	141
Gene Expression Analysis	142

Statistical analysis	142
Results	143
Tendon Biomechanical Testing.....	143
Viscoelastic Modeling	145
Histomorphological assessment of collagen fiber alignment and intramuscular adipose content.....	153
Histopathology Results.....	154
Gene Expression Analysis	158
Correlation Analysis.....	161
Discussion.....	164
Conclusions.....	167
Chapter 7- Implementation of Healthy Human Supraspinatus Tendon Hyperelastic Properties Into a Finite Element Analysis Package.....	168
Introduction.....	168
Materials and Methods	169
Results	170
Discussion.....	172
Chapter 8- Conclusion.....	173
Summary of Work.....	173
Human Cadaver Data Validates Sheep Models of Chronic Rotator Cuff Degeneration	176
Biomechanical Comparisons.....	176
Histological Comparisons.....	179
Future Work.....	180
References	182

LIST OF FIGURES

Figure 1. Muscles and Fascia of the Shoulder, Supraspinatus, Scapula, Humerus, Deltoid, Infraspinatus, Teres minor and major, Latissimus Dorsi, Triceps brachii. Image taken from Gray’s Anatomy, Plate 412 existing in the Public Domain.3

Figure 2. Structural organization of a tendon. Image made available under the Creative Commons CCO 1.0 Universal Public Domain Dedication.4

Figure 3. Ovine enthesis, H&E (10x). Yellow line illustrates transition from tendon to non-mineralized fibrocartilage. Orange line illustrates transition from non-mineralized to mineralized fibrocartilage. Green line illustrates transition from mineralized fibrocartilage to bone.5

Figure 4. Ovine tendon, H&E (400x). Illustrates the highly organized collagen structure (light pink) and sparse spindle-shaped tenocytes (purple) between collagen fibrils.6

Figure 5. Chronically degenerated human tendon, H&E (200x). Increased tenocyte presence throughout, a specific region with increased tenocyte population is provided as an example (square). Region with increased vascularization (diamond). Region with increased presence of ground substance (arrow).13

Figure 6. Surgical photos (A) Transected infraspinatus tendon capped with Gore-tex™, (B) Uncapped transected infraspinatus tendon, (C) Histologic biopsy locations. (1) Proximo-lateral muscle, (2) Proximo-medial muscle, (3) Disto-medial musculotendinous junction, (4) Disto-lateral musculotendinous junction, (5) Transected medial tendon (shown capped with Gore-Tex™), (6) Non-transected lateral infraspinatus tendon.30

Figure 7. Photomicrographs of hematoxylin and eosin stained human and ovine tendons. (A) Normal infraspinatus tendon, 20x. (B) Human rotator cuff supraspinatus tendon, 10x. Asterisk = cartilaginous metaplasia. (C) and (D) Transected portions of the sheep infraspinatus tendon, 10x. Asterisk = proliferations of stromal cells. Arrowhead = palestaining collagen fibers. Arrows = neo-vascularization. (E) and (F) Non-transection portions of the sheep infraspinatus tendon, 10x. Asterisk = collagen fiber structure, arrows = nuclei per lacunae. (G) Proximo-medial aspect of the sheep infraspinatus musculotendinous junction, 10. Asterisk = myocyte bundles, arrows = adipocytes. (H) Mucinous degeneration, 20x.35

Figure 8. Intra-operative image illustrating location of surgical insult at the midpoint of the tendon insertion (left) and digital illustration of surgical insult and relevant tissue (center). Rectangular box outlines the tendon insertion, arrow highlights the surgical cut. Image of biomechanical testing (right).49

Figure 9. (Left) Tendon cross-sectional area (CSA) measurements. (Middle) Peak stress from the stress-relaxation testing at both stretch levels. (Right) Percent relaxation from the stress-relaxation testing at both stretch levels. P-values are indicated for all pairwise comparisons which met the significance threshold (P<0.05).55

Figure 10. For each image, the black scale bars on the bottom right corner of the image are 500 μm . Representative micrographs of H&E-stained slides for all tendon groups. Marked increase of tenoblast population (square). Deposition of ground substance (arrow). Tenoblast lacunae (triangle). Increased vascularization (diamond).57

Figure 11. (Left) Overall Bonar degeneration score calculated by summing semi-quantitative scoring in the following categories: tenocytes, ground substance, collagen, and vascularity. (Right) Area of organized collagen normalized to total region analyzed as measured with polarized light microscopy and Picro-Sirius red staining. P-values are indicated for all pairwise comparisons which met the significance threshold ($P < 0.05$).59

Figure 12. Gene expression changes in Tendon following sharp transection. (A) PCA plot illustrating the gene expression variance between the different timepoints of the Sharp Transection model and uninjured. Same time points grouped according to color (legend shown in top right corner). (B) Volcano plot comparing 12-week gene expression count to uninjured. X axis shows fold change y axis shows p value. Significant genes with p value < 0.05 and fold change > 2 or < -2 shown in bright red and green gradient with ratio scale on top right. At the six-week timepoint, there were 164 significantly upregulated genes and 62 significantly downregulated genes. (C) Volcano plot comparing 16-week gene expression count to uninjured. 225 significantly upregulated genes and 20 significantly downregulated genes. (D) Volcano plot comparing 18-week gene expression count to uninjured. 937 significantly upregulated, 437 significantly downregulated.....62

Figure 13. GSEA analysis of gene expression changes following sharp transection. Bubble plot illustrating results of GSEA using the GO BP gene set. The top 30 gene sets by normalized enrichment score (NES) ($\text{FDR-}q < 0.05$ and $\text{NOM-}p < 0.01$) of the following analyses are shown: all ST vs. uninjured (A), 6-week ST vs. uninjured (B), 12-week ST vs. uninjured (C), and 18-week ST vs. uninjured (D). Bubble colors correspond to biological process category, bubble size according to gene count, and bubble location according to NES.63

Figure 14. (Left) Scatterplot illustrating the relationship between the non-destructive biomechanical response of the tendons as related to the pathologic degeneration scoring. Peak stress was markedly and significantly decreased in samples that evidenced increased pathologic characteristics ($\rho = -.72$, $P < .01$). (Right) Scatterplot illustrating the relationship between the non-destructive biomechanical response of the tendons and their respective cross-sectional areas. Peak stress was markedly and significantly decreased in samples with increased CSA ($\rho = -.67$, $P < .01$).66

Figure 15. Photos illustrating model generation and biomechanical testing. (Left) Intra-operative image depicting the location and direction of microtrauma on the ovine infraspinatus tendon. Square box indicated the enthesis. Dotted lines represent location and direction of the combed fenestrations (only 4 of the 16 cuts are illustrated). (Right) Image of biomechanical testing (image from previously published article “Enthesis trauma as a means for the development of translatable chronic rotator cuff degeneration in an ovine model” [Figure source: <http://dx.doi.org/10.21037/atm-21-354>; use permitted under the Creative Commons Attribution License the CC BY-NC-ND 4.0].76

Figure 16. Biomechanical testing results. (Left) Cross-sectional area (CSA) measurements of tendon specimens. (Middle) Peak stress values from the stress-relaxation testing ($\lambda=1.06, 1.08$). (Right) Percent relaxation values from the stress-relaxation testing ($\lambda=1.06, 1.08$). P-values are indicated for all pairwise comparisons which met the significance threshold ($P < 0.05$); individual data points are marked with symbols according to their respective groups (i.e., square (Control), triangle up (6-wk), triangle down (12-wk), diamond (18-wk)).82

Figure 17. Representative sections of H&E-stained specimens for all treatment groups. 3A) Uninjured ovine tendon. 3B) Degenerated human tendon. 3C) Combed fenestration (CF) Model 6wks. 3D) CF Model 12wks. 3E) CF Model 18wks. Square indicates regions containing representative increases to tenoblast populations. Arrow indicates regions containing increased deposition of ground substance. Triangle indicates regions containing tenoblasts within lacunae. Diamond indicates representative regions with increased vascularization. For each image, the black scale bars on the bottom right corner of the image are 500 μm . Uninjured and human chronic degenerated group images included from previously published article “Enthesis trauma as a means for the development of translatable chronic rotator cuff degeneration in an ovine model” [Figure source: <http://dx.doi.org/10.21037/atm-21-354>; use permitted under the Creative Commons Attribution License the CC BY-NC-ND 4.0].....86

Figure 18. Pathological scoring and histomorphometry results. (Left) Overall Bonar degeneration score (Center) Percent organized collagen. (Right) Percent intramuscular adipose area. P-values are indicated for all pairwise comparisons which met the significance threshold ($P < 0.05$); individual data points are marked with symbols according to their respective groups (i.e., square (Control), circle (Degenerated Human), triangle up (6-wk), triangle down (12-wk), diamond (18-wk)).....87

Figure 19. Gene expression changes in tendon following sharp transection. 5A) Principal component analysis (PCA) plot illuminating the temporal changes in gene expression in the Combed Fenestration (CF) model and uninjured. 5B) Volcano plot comparing 6-week gene expression count to uninjured. X axis shows fold change; y axis shows p value. Significant genes with p value < 0.05 and fold change > 2 or < -2 shown in bright red and green gradient with ratio scale on top right. At the six-week timepoint, there were 70 significantly up-regulated genes and 28 significantly down-regulated genes. 5C) Volcano plot comparing 18-week gene expression count to uninjured. 1,063 significantly up-regulated genes and 172 significantly down-regulated genes. 5D) Volcano plot comparing gene expression of all CF samples count to uninjured. 172 significantly up-regulated, 13 significantly down-regulated.89

Figure 20. Bubble plot demonstrating outcomes of gene set enrichment analysis (GSEA). 6A) All CF samples vs uninjured. 6B) 6-week CF vs. uninjured. 6C) 18-week CF vs. uninjured. Bubble colors correspond to biological process category, bubble size according to gene count, and bubble location according to NES.90

Figure 21. Representative scatterplots illustrating relationships between several outcome parameters. (Left) Peak stress was distinctly and significantly reduced in samples that demonstrated increased pathologic characteristics ($\rho = -.69, P = .001$). (Right) Peak stress was markedly and significantly decreased in samples with increased CSA ($\rho = -.69, P = .001$). Individual

data points are marked with symbols according to their respective groups (i.e., circle (Control), square (6-wk), triangle up (12-wk), triangle down (18-wk)).....92

Figure 22. Experimental design/treatment timeline. Ovariectomy occurred in all OP sheep at zero weeks. Intramuscular steroid injections were administered every three weeks starting at 2 weeks and ending at 16 weeks post-OVX. Beginning 16 weeks post-OVX, the BP and PBS group sheep were given weekly injections of their respective treatments. Sheep were euthanized at 28 weeks post-OVX. 103

Figure 23. Representative microCT images. (A) Circle illustrates microCT analysis region. Square indicates tendon enthesis (insertion). (B) Representative image of a sample from the Control group. (C) Representative image of a sample from the PBS group. (D) Representative image of a sample from the BP group. The samples chosen for each group exhibited the median bone volume fraction value for their respective group. 106

Figure 24. MicroCT outcome parameters. (A) Bone volume fraction was reduced in both the PBS ($p < 0.001$) and BP ($p < 0.001$) groups as compared to the Control group. (B) Trabecular number was decreased in both the PBS ($p = 0.001$) and BP ($p = 0.013$) groups. (C) Trabecular thickness was decreased in both the PBS ($p < 0.001$) and BP ($p = 0.002$) groups. (D) Trabecular spacing was increased in both the PBS ($p = 0.001$) and BP ($p = 0.013$) groups. (E) The specific bone surface was increased in the PBS ($p = 0.001$) and BP ($p = 0.007$) groups. (F) The connectivity density was decreased in both the PBS ($p < 0.001$) and BP ($p < 0.001$) groups. (G) The structure model index was increased in the PBS ($p < 0.001$) and BP ($p < 0.001$) groups. (H) The degree of anisotropy was similar for all groups. Statistical test: one-way ANOVA with Tukey's post hoc test (A,C,E,F,G,H) and Kruskal-Wallis test (B,D). Box plot indicates median and interquartile range; whiskers indicate maximum and minimum values. Individual datum points are overlaid..... 114

Figure 25. Tendon pathological scoring and histomorphometry analyses results. (A) No differences were noted in tendon collagen organization between treatment groups. (B) Increased intramuscular adipose content was measured in the PBS ($p = 0.037$) and BP ($p = 0.066$) groups as compared to the Control group. (C) No significant differences were noted in tendon degenerative pathological scoring results between treatment groups. (D) Increased semi-quantitative interdigitation scores were noted in the PBS ($p = 0.097$) and BP ($p = 0.017$) groups. Statistical test: one-way ANOVA with Tukey's post hoc test (A,B) and Kruskal-Wallis test (C,D). Box plot indicates median and interquartile range; whiskers indicate maximum and minimum values. Individual datum points are overlaid. 115

Figure 26. Representative histology micrographs of the Control, PBS, and BP groups. (A,B,C) H&E-stained sections of tendon mid-body specimens. Decreased collagen organization noted in the PBS (B) and BP (C) samples throughout. Increased tenocytes (*) and increased ground substance (†) were noted in the PBS (B) and BP (C) samples. (D,E,F) H&E-stained sections of tendon enthesis specimens. As compared to the Control samples (D, arrow), the PBS (E) and BP (F) samples exhibited decreased tidemark (arrow) symmetry and prominence. The PBS samples exhibited a notable decrease in cellularity within the fibrocartilage (‡). The BP samples demonstrated increased mesenchymal cell population within the fibrocartilage (§). (G,H,I) Trichrome stained sections of tendon enthesis specimens. As compared to Control samples (G), the PBS (H) and BP (I) samples exhibited increased interdigitation of the of the bone to MFC

junction. Sections are 5 μ m thick, formalin fixed, trifluoroacetic acid demineralized, and paraffin embedded. Scale bar: 50 μ m (A,B,C), 100 μ m (D,E,F), and 200 μ m (G,H,I). 118

Figure 27. Hyperelastic strain energy function fitting results. (A) A decrease in the Ogden μ term was noted in the PBS group as compared to the Control group ($p=0.083$). The BP group exhibited increased μ term values as compared to the PBS group ($p=0.073$) which were similar to those exhibited by the Control group ($p>0.999$). (B) An increase in the Ogden non-linearity term (α) was noted in the PBS group as compared to the Control group ($p=0.026$), while the BP group exhibited values closer to the Control group ($p=0.463$). (C) RMSE values were below 0.5 MPa for all groups. (D) Normalized fitting errors across all groups were below 3.2%. (E) No significant differences were noted in tendon CSA between treatment groups. (F) Young's modulus vs Stretch plot. Symbols indicate group means, shaded regions illustrate standard deviation of the group samples, and dotted lines indicate best-fit nonlinear regressions. Statistical test: one-way ANOVA with Tukey's post hoc test (C,D) and Kruskal-Wallis test (A,B,E). Box plot indicates median and interquartile range; whiskers indicate maximum and minimum values. Individual datum points are overlaid. An Extra Sum-of-Squares F Test was performed to reject the null-hypothesis that one curve could adequately fit all data ($p<0.0001$; F). 121

Figure 28. Young's modulus values for all groups at discrete stretch levels ($1.00 \leq \lambda \leq 1.10$). Statistical test: Kruskal-Wallis test (all). Box plot indicates median and interquartile range; whiskers indicate maximum and minimum values. Individual datum points are overlaid. 122

Figure 29. Viscoelastic fitting results. (A) The BP group exhibited increased G1 term values as compared to the PBS group ($p=0.058$) and the Control group ($p=0.229$). (B) The BP group demonstrated decreased G2 term values as compared to the PBS group ($p=0.075$) and the Control group ($p=0.526$). (C) The BP group displayed similar G3 term values as the PBS group ($p>0.999$) and the Control group ($p>0.999$). (D) The BP group exhibited similar G4 term values as the PBS group ($p>0.999$) and the Control group ($p=0.633$). (E) The PBS group demonstrated decreased G_{∞} term values as compared to the Control group ($p=0.136$) and the BP group ($p=0.306$). (F) Mean reduced relaxation modulus function for each group is plotted against time. Symbols indicate group means and solid lines connect adjacent points. Points graphed 1 every 3 seconds. Differences in the short-term relaxation behavior is evident between the Control and OP groups. Statistical test: one-way ANOVA with Tukey's post hoc test (A,B,E) and Kruskal-Wallis test (C,D). Box plot indicates median and interquartile range; whiskers indicate maximum and minimum values. Individual datum points are overlaid..... 123

Figure 30. Correlation plots for Ogden hyperelastic terms and other outcome parameters. Spearman correlation values and p-values are listed in Table 1..... 126

Figure 31. Stress-relaxation testing results. A) Peak stress ($\lambda=1.06$). The aged infraspinatus and subscapularis samples exhibited significantly decreased peak stress as compared to their respective younger age group samples. B) Peak stress ($\lambda=1.08$). The aged infraspinatus and subscapularis samples exhibited significantly decreased peak stress as compared to their respective younger age group samples. C) Percent relaxation ($\lambda=1.06$). The aged infraspinatus samples exhibited significantly increased percent relaxation as compared to the younger infraspinatus samples. D) Percent relaxation ($\lambda=1.08$). The aged subscapularis samples demonstrated significantly increased percent relaxation as compared to the younger subscapularis samples. Statistical test: Welch's t-

test. Box plot indicates median and interquartile range; whiskers indicate maximum and minimum values..... 145

Figure 32. One-term Ogden hyperelastic modeling parameters. A) Ogden μ -term. The aged infraspinatus and subscapularis samples exhibited significantly decreased μ -term values as compared to their respective younger samples. B) Ogden α -term. The aged subscapularis samples exhibited significantly increase α -term values as compared to the younger subscapularis samples. Statistical test: Welch's t-test. Box plot indicates median and interquartile range; whiskers indicate maximum and minimum values..... 147

Figure 33. Young's modulus vs Stretch plots. A) Aged and Younger Supraspinatus fits. B) Aged and Younger Infraspinatus fits. C) Aged and Younger Subscapularis fits. D) Aged and Younger Teres Minor fits. Extra Sum-of-Squares F Tests were performed between aged and younger groups for each tendon to confirm separate fits should be performed for each age group (all $p < 0.0001$). Shaded regions illustrate ± 1 standard deviation from respective group means..... 148

Figure 34. Young's modulus values for all groups at discrete stretch levels ($1.00 \leq \lambda \leq 1.10$). Statistical test: Welch's t-test. Box plot indicates median and interquartile range; whiskers indicate maximum and minimum values..... 151

Figure 35. Prony series values representing the reduced relaxation moduli for all four tendons in the aged and younger groups. A) G1 Prony term. The aged infraspinatus samples exhibited significantly increased G1 values as compared to the younger infraspinatus samples. B) G2 Prony term. The aged teres minor samples exhibited significantly increased G2 values as compared to the younger teres minor samples. C) G3 Prony term. No significant differences were noted between age groups in any tendons. D) G4 Prony term. No significant differences were noted between age groups in any tendons. E) G_∞ Prony term. No significant differences were noted between age groups in any tendons. Statistical test: Welch's t-test. Box plot indicates median and interquartile range; whiskers indicate maximum and minimum values. 152

Figure 36. Reduced relaxation modulus vs. time plots. A) Aged and Younger Supraspinatus fits. B) Aged and Younger Infraspinatus fits. C) Aged and Younger Subscapularis fits. D) Aged and Younger Teres Minor fits. 153

Figure 37. Histomorphometry and histopathology results. A) Percent organized collagen across aged and younger groups in all four tendons. No significant differences were noted between age groups in any tendons. B) Intramuscular adipose content. The aged infraspinatus and teres minor muscle biopsies exhibited significantly increased intramuscular adipose content as compared to their respective younger groups. C) Bonar degeneration scores. The aged infraspinatus samples demonstrated significantly increased pathological degenerative characteristics as compared to the younger infraspinatus samples. Statistical test: Welch's t-test. Box plot indicates median and interquartile range; whiskers indicate maximum and minimum values..... 157

Figure 38. Representative histology micrographs of healthy (A,C) and degenerated (B,D) tendon and muscle sections. Increased tenocytes (*) and increased ground substance (†) typical of degenerated samples. Increased intramuscular adipose content (‡). Scale bars are 100 μ m. 158

Figure 39. Gene expression changes across all four human rotator tendons secondary to aging and degeneration. A) Principal component analysis (PCA) plot illuminating the differential expression secondary to degeneration. Points colored according to Bonar score. B) Volcano plot comparing the aged and younger samples illustrating the 725 significantly regulated genes with fold change greater than ± 2 . C) Volcano plot comparing the healthy and degenerated samples illustrating the 445 significantly regulated genes with fold change greater than ± 2 160

Figure 40. Mesh convergence results using longitudinal strain and strain energy. 171

Figure 41. Longitudinal strain in rectangular bar. 171

Figure 42. Longitudinal stress of rectangular bar. 172

Figure 43. Peak stress for all timepoints of ST and CF models as well as younger and aged cadaver groups. 178

Figure 44. Peak stress for all timepoints of ST and CF models as well as younger and aged cadaver groups. 179

Figure 45. Bonar score results for all timepoints of ST and CF models as well as younger and aged cadaver groups. 180

LIST OF TABLES

Table 1. Histologic scoring of tendon biopsies. Human samples N=10. Ovine 6 and 12-week, transected and non-transected samples N=3.....	36
Table 2. Histologic scoring of musculotendinous junction and muscle biopsies. Ovine 6 and 12-week, transected and non-transected samples N=3.....	39
Table 3. Biomechanical and geometric properties for tendon samples. Data are shown as means \pm SD.....	56
Table 4. Correlation of changes in gene expression with mechanical testing results and pathological characteristics. 172 genes were selected from 6-, 12-, and 18-week time points compared to uninjured control, based on a fold change of >2 or <-2 . For n=11 sheep, gene expression in RPKM was compared to numerical values of mechanical scoring. Significant values were filtered out based on $p<0.05$ in correlation analysis. This table shows list of genes with high correlation to mechanical testing categories in collagen organization, percent relaxation, and Bonar degeneration score.....	65
Table 5. Biomechanical and geometric properties for tendon samples.	84
Table 6. Correlation analyses results.	93
Table 7. Spearman correlation values for Ogden hyperelastic coefficients with other outcome parameters.....	125
Table 8. Sample sizes.	143
Table 9. Best-fit values for Young's modulus vs. stretch curves for all age groups and tendons.	149
Table 10. Viscoelastic modeling prediction errors.	150
Table 11. Categorical Bonar degeneration scoring results.....	155
Table 12. Correlation analysis results.....	161

LIST OF EQUATIONS

Equation 1.....	8
Equation 2.....	9
Equation 3.....	10
Equation 4.....	10
Equation 5.....	109
Equation 6.....	110
Equation 7.....	110
Equation 8.....	110
Equation 9.....	111
Equation 10.....	138
Equation 11.....	138
Equation 12.....	138
Equation 13.....	139

Chapter 1- Background

Rotator Cuff Tendon Injuries and Healing Dysfunction

Rotator cuff tendon tears (RCTs) can cause pain, instability, and an inability to perform day-to-day tasks. RCTs are the most common soft tissue injuries in the shoulder, causing pain and dysfunction; with 250,000 repairs being performed annually in the USA (\$3.44B annual societal impact in the USA) ⁽¹⁻⁶⁾. The original insult causing the cuff tears can be multifaceted, but generally stems from an acute injury resulting in chronic degeneration or emanates from a combination of overloading and degeneration ^(7,8). Previous studies of cadaveric shoulders have found that 18.5% of the general population has at least partial tears of rotator cuff tendons ^(9,10). As these partial tears do not typically result in significant impairment of the arm's function, conservative treatment is generally implemented in lieu of surgical repair ⁽¹¹⁾. However, growing clinical and basic science evidence suggests that these partial tears result in a deleterious degenerative cascade of the rotator cuff tendon / muscle group, leading to fatty infiltration, loss of muscle strength, and most importantly, increased probability of full thickness tears at a later point in life ^(12,13). Additionally, this chronic degeneration of the tendon(s) (a.k.a., tendinopathy) has a negative impact on the clinical outcome of repair surgeries on torn tendons, which currently have unacceptable re-tear rates. Specifically, re-tear rates of arthroscopic repairs have been reported to be as high as 94% depending on exacerbating risk factors such as tear size, patient's age, smoking history, obesity, fatty degeneration, tendon retraction, and quality of the surgical repair ⁽¹⁴⁻¹⁷⁾. Therefore, there exists a need for basic science research to better understand the degeneration cascade and to investigate potential therapies to improve repair prognosis. The background presented in the following

sections is included to provide the necessary information and justification for the research outlined in the Specific Aims section.

Rotator Cuff Tendon Anatomy

The rotator cuff is a group of tendons in the shoulder that are responsible for stability and mobility of the arm. Specifically, the rotator cuff is comprised of four tendons: supraspinatus, infraspinatus, subscapularis, and teres minor. These tendons attach to the upper humerus and are responsible for glenohumeral stability and motion of the humerus with respect to the shoulder (Figure 1). While complex motions are typically accomplished through activation of two or more of these tendons, each tendon is responsible for specific basic arm motion. The subscapularis allows internal rotation of the shoulder. The supraspinatus allows for abduction of the arm. The infraspinatus and teres minor provide for the external rotation. As such, dysfunction or tears to any of these tendons can cause significant impairment to arm movement and associated pain.

As seen in Figure 1, these tendons insert on the humerus with muscles originating from the scapula, thus passing through the joint capsule. When passing through the joint capsule, these tendons meld with the joint capsule resulting in a musculotendinous collar that surrounds the anterior, posterior, and superior aspects of the humeral head⁽¹⁸⁾.

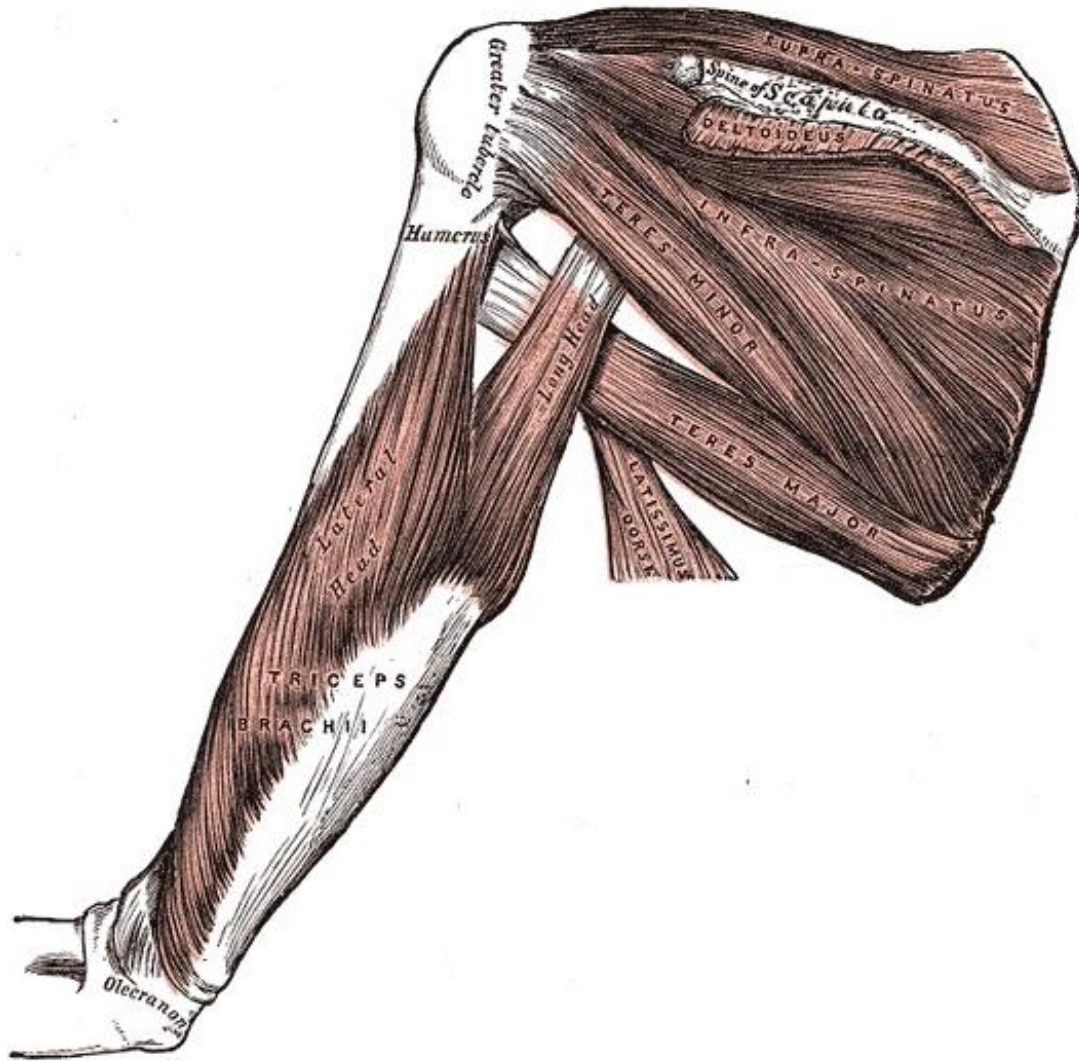


Figure 1. Muscles and Fascia of the Shoulder, Supraspinatus, Scapula, Humerus, Deltoid, Infraspinatus, Teres minor and major, Latissimus Dorsi, Triceps brachii. Image taken from Gray's Anatomy, Plate 412 existing in the Public Domain.

Tendon

Material Composition and Macrostructure

Tendons play an integral role in skeletal connection and locomotion, being the tissue that connects muscle to bone. As such, they exhibit complex material properties that allow transmission of large

forces while simultaneously allowing flexibility for adequate mobility of joints. To accomplish this, tendons are a natural composite material with a specific geometry and unique biomechanical properties, following their form-function relationship.

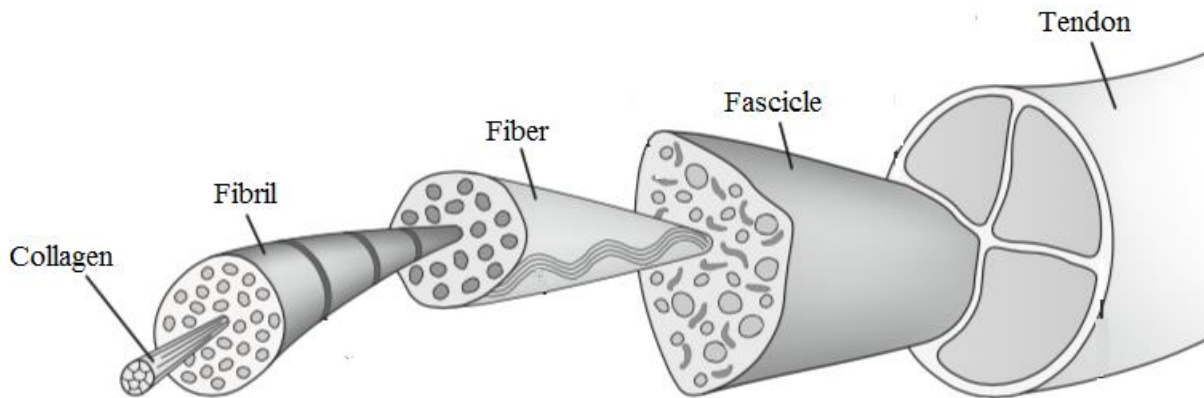


Figure 2. Structural organization of a tendon. [Image](#) made available under the [Creative Commons CCO 1.0 Universal Public Domain Dedication](#).

Tendons are arranged in an organized, hierarchical manner. By weight, collagen fibers comprise the majority of the tissue's dry weight ⁽¹⁹⁾ and are primarily type I collagen ⁽²⁰⁾. These collagen fibers are organized into microfibrils, sub-fibrils, fibrils, and fascicles, which ultimately comprise the tendon (

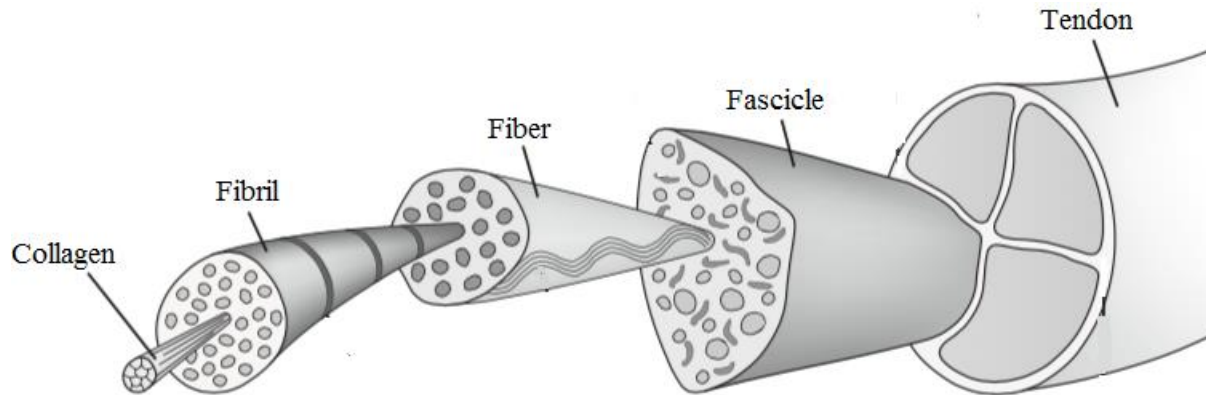


Figure 2). Proteoglycans are a major component of the ground substance which binds the individual collagen fibers together, comprising less than 1% of the dry weight of tendons ⁽²¹⁾. These collagen fibers are highly organized in parallel, crimped waveforms that align with the long axis

of the tendon (Figure 3). The combination of molecular bonding between collagen fibrils and collagen crimping is believed to provide the underlying mechanisms behind the complex viscoelastic properties exerted by the tendons ⁽¹⁹⁾. The endotenon is a fascicular sheath which separates the fascicles and reduces the friction between adjacent fascicles, allowing the fascicles to slide with respect to each other, promoting tendon plasticity as the joint articulates.

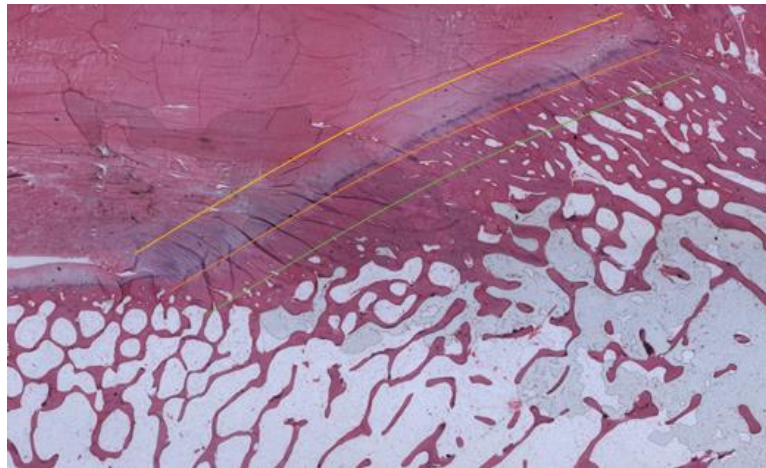


Figure 3. Ovine enthesis, H&E (10x). Yellow line illustrates transition from tendon to non-mineralized fibrocartilage. Orange line illustrates transition from non-mineralized to mineralized fibrocartilage. Green line illustrates transition from mineralized fibrocartilage to bone.

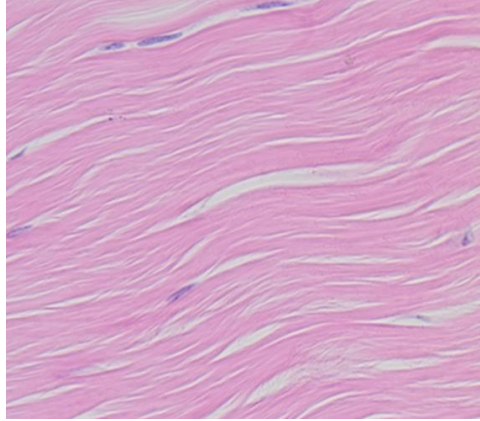


Figure 4. Ovine tendon, H&E (400x). Illustrates the highly organized collagen structure (light pink) and sparse spindle-shaped tenocytes (purple) between collagen fibrils.

The transitional zone in which the tendon inserts to the bone is referred to as the enthesis. The enthesis region is complex and composed of several distinct regions including tendon, non-mineralized fibrocartilage, mineralized fibrocartilage, and bone (Figure 3). Differences in stiffness between the tendon and the bone result in a large stress concentration at the interface; thus, the insertion zone is crucial in providing a gradient in material stiffness, reducing the concentration of stress and improving the robustness of the connection^(20,22). Cellularity also varies across this transitional region. Cellularity within the tendon is relatively low, being composed primarily of specialized fibroblasts, referred to as tenocytes, interspersed between tendon fibrils (Figure 4). In a healthy tendon, these tenocytes present as spindle-shaped cells aligned with the loading axis of the tendon. Tenocytes are responsible for generation of the ground substance and fibrillogenesis, which occur as a result of mechanobiological signaling⁽²³⁻²⁵⁾. Cell populations are composed of fibrochondrocytes within the fibrocartilaginous region and by osteoblasts, osteocytes, and osteoclasts within the bone^(22,26). Changes to the tenocyte population with injury and degeneration are described in the *Chronic Rotator Cuff Degeneration* section of this document.

Tendon Biomechanics

The collagen structure/molecular bonding within the tendon body and the fibrocartilaginous insertion play crucial roles in tendon strength, structural integrity, and biomechanical properties. Tissue loading *in vivo* is highly dynamic, with immense, dynamic loading imposed on the tissue. As mentioned previously, tendons exhibit viscoelastic behavior. While elastic material stress response can be calculated solely based on deformation, viscoelastic material stress response is a function of both deformation and time. Additionally, the large deformations exhibited by soft tissues like tendon result in highly nonlinear stress-strain relationships, formally referred to as hyperelasticity. Therefore, the typical material properties reported for engineering materials that rely on the assumption of infinitesimal strain are not relevant or appropriate for tendons. As such, knowledge of these topics is requisite to characterize tendon biomechanical properties before and after injury. Brief introductions to hyperelasticity and viscoelasticity are provided in the following two sections.

Hyperelasticity

Hyperelasticity describes the stress-strain relationship in materials that exceed the finite strain assumption of Hooke's law. When materials undergo large strains, referred to as stretch at these large magnitudes, the relationship between stress and strain can no longer be modelled as linear. Biologic soft tissues, such as tendon, frequently undergo strains well beyond the infinitesimal strain assumption of 0.1%, thus necessitating hyperelastic constitutive theories to describe their stress-stretch behaviors. The most common theory used to characterize tendons is referred to as the Ogden hyperelastic model⁽²⁷⁾. This model compensates for the non-linear stress-stretch

relationship by modeling the strain energy according to the following equation (assuming no change in volume):

$$W(\lambda_1, \lambda_2) = \sum_{p=1}^N \frac{\mu_p}{\alpha_p} (\lambda_1^{\alpha_p} + \lambda_2^{\alpha_p} + \lambda_1^{-\alpha_p} \lambda_2^{-\alpha_p} - 3)$$

Equation 1

In this formulation, the variable W represents the strain energy, μ represents the shear modulus, α represents the non-linearity, and λ (1,2,3) represent the principal stretches. Through use of this empirical model, the μ and α terms can be fit to the experimental λ data, allowing modeling of the nonlinear stress stretch characteristics of the material.

Viscoelasticity

Viscoelasticity describes material behavior that exhibits time-dependent properties. There are several different viscoelastic theories that have been used to describe material behavior. Linear viscoelasticity provides for time-dependent relaxation that is independent of strain magnitude. Quasi-linear viscoelasticity describes the time-dependent relaxation that is linearly proportional to the strain magnitude. Non-linear viscoelasticity removes the linear assumption of quasi-linear viscoelasticity, describing materials for which the relaxation is a function of time and strain magnitude. Stress relaxation testing allows for quantification of the viscoelastic properties of materials. Briefly, a strain is imposed on the material being tested and held constant for a period of time. The force is measured over the entire static hold period; viscoelastic materials will exhibit a decrease in force at a constant strain. The changes in that force over the static hold period can be

utilized to quantify the viscoelastic properties of the material being tested. Measurements such as peak stress (highest stress during static hold period) and percent relaxation (percent of load decrease over static hold period) can be reported to allow comparisons between materials. Viscoelastic material properties can be derived such that material behavior can be modeled *in silico*.

Modeling the Viscoelastic and Hyperelastic Properties of Tendons

To investigate the change in tendon material properties associated with injury, it is necessary to characterize/model the hyperelastic and viscoelastic material properties of the tendon(s). It has previously been demonstrated that quasilinear viscoelasticity (QLV) can successfully be implemented to describe the non-linearity seen in soft tissue elastic and viscous responses to arbitrary strain inputs⁽²⁸⁻³⁰⁾. As outlined by Fung⁽³¹⁾, tissue response to uniaxial loading (the method physiologic loads are applied to tendons) can be approximated in terms of engineering strain by:

$$\sigma[\varepsilon(t), t] = \int_0^t G(t - \tau) \frac{d\sigma^e(\varepsilon)}{d\varepsilon} \frac{d\varepsilon(\tau)}{d\tau} d\tau$$

Equation 2

where $G(t)$ represents the reduced relaxation modulus which captures the viscous behavior, and $\sigma^e(\varepsilon)$ represents the non-linear elastic (i.e., instantaneous hyperelastic) behavior. $G(t)$ can be modeled through implementation of a Prony series defined as:

$$G(t) = G_{\infty} + \sum_{i=1}^4 G_i e^{-t/\tau_i}.$$

Equation 3

In this formulation, the relaxation modulus terms (G_i) are constrained to be positive and their sum equal to one. Time constants can be assigned to appropriately capture the time-mediated tissue response. To model the hyperelastic behavior of the tendons, a 1-term Ogden constitutive equation can be implemented:

$$\sigma^e(\varepsilon) = \frac{2\mu}{\alpha} [(\varepsilon + 1)^{\alpha-1} - (\varepsilon + 1)^{-\alpha/2-1}],$$

Equation 4

where μ and α represent the shear modulus and the non-linearity terms, respectively. This formulation would result in a number of fitted terms depending on the number of time constants being implemented. These terms would include: μ , α , and $\sum G_i$. Using these modeling approaches has enabled researchers to probe the differences between healthy and diseased biological tissues⁽³²⁾. However, to date there is limited data regarding the Viscoelastic and Hyperelastic Properties of Tendons, which makes it intractable for researchers to understand the biomechanical changes secondary to chronic rotator cuff degeneration.

Chronic Rotator Cuff Degeneration

The etiology of chronic tendon degeneration is complex, and the mechanistic underpinnings are not yet fully understood. The rotator cuff tendon itself is not typically capable of healing naturally from a full-thickness tear⁽³³⁾, and degeneration is exacerbated by several factors including, but not

limited to, low blood supply within the tendon, the lack of acute treatment in most patients, and the aggressive degeneration cascade observed in collagenous tissues^(7,34,35). Chronic degeneration is known to entail several pathological changes in tendons, including a proliferation of tenocytes, excess proteoglycan content, disorganized collagen fibers, and increased vascularization (Figure 5)⁽³⁶⁻³⁹⁾. These changes are well-documented and scoring systems have been proposed with the goal of providing a uniform methodology for quantifying the degree of pathologic manifestation of degenerative changes. The most prominent of these scoring systems is the ‘Bonar score’, which incorporates the aforementioned degenerative characteristics to generate a “degeneration” score⁽⁴⁰⁾. Specifically, tenocyte reactivity (Figure 5), angiogenesis (Figure 5), collagen organization (Figure 5), and ground substance presence (Figure 5) are graded semi-quantitatively on a scale from zero to three, with a score of zero representing healthy and three indicating severe pathology. The scores from the four individual categories are summed, yielding one score that represents the overall degeneration level of the specimen being analyzed.

The changes that can be quantified via the Bonar scoring rubric are understood to be mediated through molecular signaling as evidenced by differential gene expression in injured tendons as compared to uninjured tendons⁽⁴¹⁻⁴⁵⁾. The study of molecular signaling in tendon degeneration is in early stages, with recent studies developing biomarkers of tendon degeneration⁽⁴⁴⁾ and exploring changes in collagen and matrix metalloproteinase gene expressions^(46,47) secondary to tendon injury. Some studies have investigated whole transcriptome changes via RNA sequencing^(48,49); unfortunately, the peer-reviewed data for this is lacking, with few studies investigating changes in controlled injuries (i.e., comparative animal models) or in relevant human populations (i.e., healthy and diseased) with adequate sample sizes (i.e., having statistical power) and temporal differences.

Therefore, studies investigating the temporal transcriptome changes in a controlled injury model and in representative human populations are sorely needed. These data would provide valuable insight for researchers into the changes to gene expression resulting from degeneration and could potentially help illuminate therapeutic targets to arrest the molecular pathways of degeneration.

Regrettably, changes are not limited to the tendon tissue; marked fatty infiltration and atrophy of the associated muscle groups is another hallmark of rotator cuff degeneration. There is no consensus on a single underlying cause leading to chronic rotator cuff degeneration, but it is hypothesized that the degeneration cascade stems from factors such as overuse or history of tendon injury (i.e., previous partial width tears)^(50,51). The manifestations of chronic rotator cuff degeneration lead to decreased quality of life and diminished prognosis of surgical repair to torn tendons; however, chronic degeneration of the rotator cuff tendons is not the only contributor to decreased rotator cuff repair surgery failures.

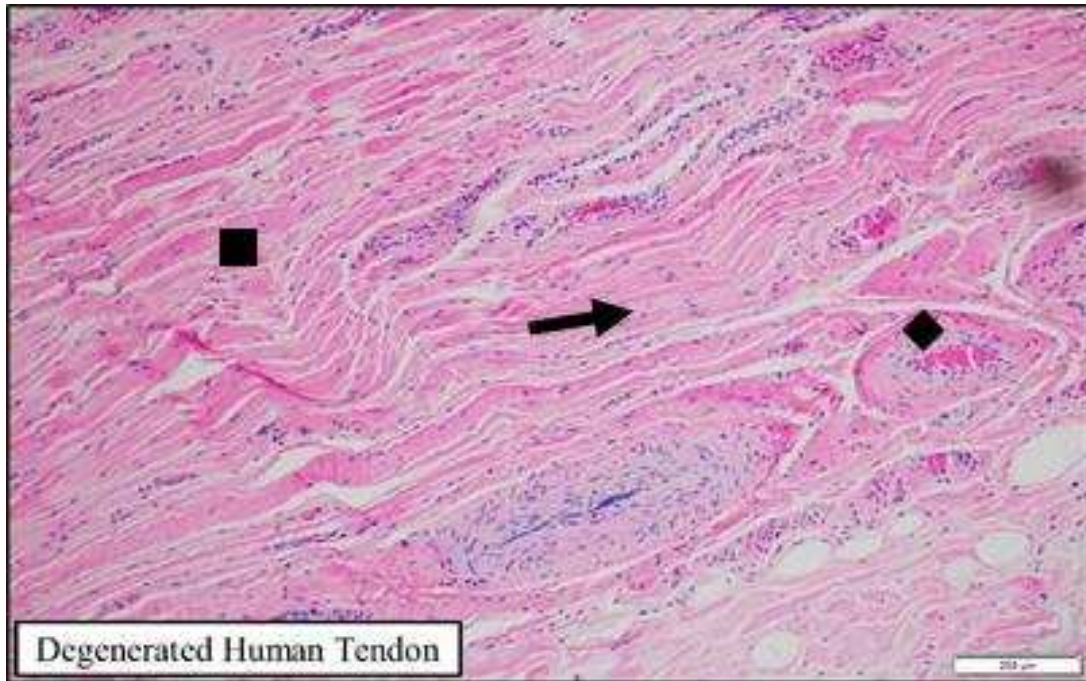


Figure 5. Chronically degenerated human tendon, H&E (200x). Increased tenocyte presence throughout, a specific region with increased tenocyte population is provided as an example (square). Region with increased vascularization (diamond). Region with increased presence of ground substance (arrow).

Osteoporosis as a Risk Factor for Rotator Cuff Repairs

Interestingly, rotator cuff repair surgeries exhibit increased prevalence in patients with osteoporosis (OP), with OP patients experiencing 1.6-7.25 times the repair failure rate of patients without OP⁽⁵²⁻⁵⁴⁾. This is a startling realization, considering that greater than 10 million people within the United States have OP, with that number expected to grow⁽⁵⁵⁾. OP is a diagnosis given to patients with diminished bone density; as such, most research regarding this condition is focused on restoring bone mineral density as a means to reduce fracture risk. Research investigating the cause for the increased prevalence of rotator cuff repair failures in OP patients is lacking, especially considering that most OP patients are older, which is an additional risk factor for full-thickness

rotator cuff tears. Additionally, the effect of OP therapies on tendons has not been investigated thoroughly. Therapies such as bisphosphonates⁽⁵⁶⁾ and Teriparatide⁽⁵⁷⁾ have been widely used to improve bone mineral density, yet their effect on tendons has not been well documented, highlighting yet another reason to investigate these conditions and therapy effect on tendons.

Current Treatment Strategies and Future Improvement Opportunities

For patients (both “normal” and those with OP) with full-thickness rotator cuff tears, it is oftentimes necessary to pursue surgical treatment if functional impairment and persistent symptoms persist after conservative treatment⁽⁵⁸⁾. Despite advanced approaches for rotator cuff repair, most surgical repairs experience a high rate of failure^(14,59). In 20% to 94% of patients, the surgical repair fails to heal, with the failure rate correlating with the size of the tear, time from the initial injury, tendon quality, fatty atrophy within both the tendon and adjacent muscle, and the surgical repair technique^(14,16,51,58,60-63).

Several strategies have been investigated to improve the prognosis of rotator cuff tendon repairs, including improved suturing techniques⁽⁶⁴⁾, the implementation of biologically derived injectables⁽⁶⁵⁾, and repair augmentations through implementation of biologic and synthetic scaffolds^(3,66-72). Unfortunately, these strategies have failed to recapitulate the natural tendon insertion zone in humans, and as mentioned previously, the recreation of this specific insertion zone mechanical gradient is necessary to restore the natural strength and durability of the tendon insertion⁽²⁰⁾.

Current scaffolds have been designed to either deliver biologically active ingredients, such as mesenchymal stem cells^(20,73-79), or to improve the acute strength of the repair^(3,67,68,80). While both of these strategies are addressing fundamental issues seen in current repair failures; however, both are not addressing an important strategy that may improve healing outcomes. As mentioned previously, it has been shown that biomechanical cues are the regulating mechanism for fibroblasts to initiate fibrillogenesis⁽²⁴⁾. As such, scaffold biomechanics should be designed to not only improve time zero repair strength, but they should also aim to replicate native tendon biomechanical properties throughout the insertion gradient, providing the mechanobiological cues for collagen growth, tendon regeneration, superior osseointegration, and ultimate tendon repair durability.

Animal Models of Chronic Rotator Cuff Degeneration

The poor prognosis and high frequency of rotator cuff damage necessitates continued research into new surgical techniques and therapeutics to improve upon currently inadequate clinical outcomes. To investigate the tendinopathy of rotator cuff injuries, it is necessary to have controlled experimental platforms. As it is not possible to control extent of injury or to simulate the degeneration cascade with human cadavers, translational comparative animal models are considered to be the most appropriate and allow for the simulation of physiology of injury and repair. A variety of translational comparative animal models (e.g., murine, leporine, canine, ovine, and non-human primates) have been used in attempts to simulate the human degeneration cascade; however, none have been able to faithfully recapitulate the broad spectrum of changes that are seen

in humans⁽⁸¹⁻⁸⁵⁾. The following sections provide a brief background on previous injury simulations used on different animal platforms, highlighting their inadequacies and justifying our pursuit of a more translatable model.

Rodent and Small Animal Models

Murinae and leporines have been implemented as animal models for investigating the rotator cuff^(81,86-88). Previous research^(81,89) has compared the similarity of the different animals to human, comparing shoulder musculature, bony anatomy, articulations, and motions of the joint. This research indicated that due to similar anatomy, including an acromion arch, the rat could act as a model for rotator cuff degeneration and injury. The original model that was promoted involved either an intratendinous injection of collagenase or a tendon allograft to simulate impingement, which was originally believed to be the cause of chronic tendon degeneration⁽⁸¹⁾. Both alterations were able to produce increased cellularity and decreased collagen organization, both of which are pathological traits that have been noted clinically in human with chronic rotator cuff degeneration⁽⁴⁰⁾. However, small animals have been documented⁽⁸⁹⁾ to have increased natural healing capacity which may confound the ability to discern whether treatments have a positive effect (i.e., scar tissue will form between the tendon and bone in absence of treatment). Additionally, the inherently small size of some of these animal models precludes the assessment of physiologically-relevant sized devices or comparable dosages of cellular therapies intended for use in humans. While small animal models such as the aforementioned rat models have shown great utility in researching the initial injury cascade and some biologic healing mechanisms, certain

limitations restrict their use in investigations of strategies such as surgical techniques and scaffold implementation, thus, necessitating relevant large animal models.

Canine Models

Canine models have been explored as a means to simulate rotator cuff injuries and degeneration in a large animal model^(70,83). These models were produced through transection of a portion of the tendon followed by immediate repair, with the reasoning that injuring a portion of the tendon may replicate the single tendon tear seen in humans clinically. While deleterious biomechanical changes were noted and histopathological changes were seen with similar indications to those noted in degenerated human tendons, studies have only investigated single timepoints, precluding the temporal changes associated with this model^(70,83). Furthermore, societal concerns with utilizing dogs for research have presented a large barrier to the implementation of this model.

Non-Human Primate Models

Advanced non-human primates have the potential to present the most anatomically accurate preclinical model for rotator cuff injury, as they are the only species that have an actual rotator cuff spanning a joint capsule that utilize overhead motions similar to humans. Additionally, primates frequently perform overhead motions with their arms, similar to humans. Some researchers have investigated their use as a model through complete transection and reattachment of the supraspinatus tendon⁽⁸⁵⁾. This model was capable of producing similar changes to humans, including neovascularization, added fibrous tissue overlaying the injury, and decreased collagen

organization. No histologic commentary was provided regarding cellular activity. Unfortunately, the exorbitant costs, societal concerns, implemented restrictions of use imposed by regulatory bodies such as the Food and Drug Administration (FDA), and management issues associated with these animals precludes their use in meaningful quantities of research.

Ovine Models

The lower translatability of rodent/small animal models and societal concerns of canine / primate models has led some researchers to propose the use of ewes (a.k.a., sheep and/or ovine) as a translational model for rotator cuff injury due to their similarity to humans in tendon size (eliminating the necessity to scale devices being tested), healing rates, stoicism (pain tolerance), and societal acceptance ^(71,90,91). One of the first ovine models used as a means to generate degenerative changes to tendons in shoulder involved a full transection of the infraspinatus tendon with a delayed repair⁽⁹²⁾. This model was considered the gold-standard for some time^(3,92,93); However, it has recently been demonstrated that this model leads to severe tendon retraction and increased pathological characteristics, which is not observed clinically and results in repair surgery complications⁽⁹⁴⁾. These limitations are, in part, the driving factors for the work proposed within; with the ultimate goal of improving upon the previously considered gold standard model.

Summary

The current prognosis for rotator cuff repair surgeries is not acceptable, especially considering the increase in failure rate associated with the chronically degenerated tendons frequently found in the

aging population. Unfortunately, the underlying mechanisms for the chronic degeneration seen clinically is not fully understood, warranting additional basic science and translational research. Ideally, research could be conducted using chronically degenerated human tendon; however, the ethical concerns and inability to control the injury and usage history preclude the study of many important factors with these tissues. Animal models better allow for control of injury and use history, but current animal models cannot accurately replicate the spectrum of changes that have been documented clinically in humans.

With this in mind, the goal of this dissertation project is to investigate and characterize the pathologic and biomechanical tendon changes in novel ovine injury models and to validate these changes using human cadaver tissue. In order to meet these objectives, this project is focused on: (1) the investigation of a partial transection ovine model of chronic rotator cuff degeneration, (2) the characterization of an ovine model of chronic rotator cuff degeneration induced through entheses damage, (3) the characterization of an ovine model of chronic rotator cuff degeneration induced without entheses damage, (4) investigation of the underlying mechanisms causing the increased prevalence of rotator cuff repair failures in patients with osteoporosis, (5) the validation of these models through human cadaveric experiments, and then use this information to (6) design a computational model of a prototype instructive scaffold that approximates the gradient of mechanical properties seen in healthy human supraspinatus tendon (i.e., bone to fibrocartilage to tendon).

It is hypothesized that through surgical insult to the enthesis or tendon mid-body, pathologic changes to the tendon will be induced that will replicate what has been documented clinically in humans with chronic rotator cuff degeneration. The second goal of this work is to document the viscoelastic and pathologic changes in tendons from osteoporotic animals to illuminate the underlying mechanism for increased prevalence of rotator cuff repair failures in patients with osteoporosis. Finally, human data will be utilized to develop computational models of an instructive scaffold designed to replicate the gradient of mechanical properties seen in the human supraspinatus tendon.

Specific Aims

In order to address the aforementioned basic science gaps in the data regarding chronic rotator cuff degeneration, incrementally complex ovine models of chronic rotator cuff degeneration have been implemented and characterized, with the goal of creating an accurate translational model. As such, the following specific aims were pursued:

Specific Aim 1: Investigate the ability of a ‘partial release’ of the ovine infraspinatus tendon to replicate the chronic tendon degeneration seen in human rotator cuff tendons.

Previous models for chronic rotator cuff degeneration have completely transected the tendon and attached at a later date (i.e., follow degeneration). It has been found that the pathologic changes induced by this surgical model are of increased severity and reactivity as compared to what is seen clinically in chronically degenerated human rotator cuff tendons. Therefore, the goal of this aim

was to investigate the severity of changes that occur if only a portion of the width of the tendon's bony insertion is transected. It was hypothesized that this model would represent a partial thickness tendon tear and thus would alter the strain imposed on the tendon (i.e., half of the tendon unstrained/unloaded and half of the tendon over strained/over loaded), and thus the pathologic changes induced would be more similar (as compared against previous ovine models) to what occurs naturally in humans with chronically degenerated rotator cuff tendons. This model was assessed via histopathology at multiple timepoints. The results of Specific Aim 1 provided the justification for Specific Aims 2 and 3.

Specific Aim 2: Develop a large animal model of chronic rotator cuff degeneration induced by sharp partial transection (enthesis damage).

It was found that by releasing one half of the tendon (i.e., partial release model), severe pathologic changes were noted in the released half of the tendon that did not represent what has been noted in humans. Thus, it was hypothesized that partial release of the tendon is not an appropriate method to induce chronic degeneration in an ovine model. With this in mind, this goal of this aim, Specific Aim 2, was to investigate whether a clinically translatable ovine model of chronic rotator cuff degeneration could be induced through controlled enthesitis damage, herein referred to as Sharp Partial Transection (ST). Succinctly, in this model 50% of the enthesitis site was released in an attempt to recapitulate a partial thickness bursal-sided tear which is commonly seen in humans. To determine the translatability of this model it will be characterized at multiple timepoints through biomechanical, histopathological, histomorphological, and gene expression analyses.

Specific Aim 3: Develop a large animal model of chronic rotator cuff degeneration induced by combed fenestration (mid-substance damage).

Previous large animal models of chronic rotator cuff degeneration rely on enthesis disruption as a means of model generation. While this type of model provides valuable insight into a tendon's healing response post-injury and potential methods to re-establish the native enthesis gradient, it precludes the testing of therapies that are designed at reversing chronic degeneration prior to full-thickness tears occur. Therefore, the goal of Specific Aim 3 was to generate and characterize a clinically translatable model of chronic rotator cuff degeneration that does not rely on enthesis disruption as a means of induction, herein referred to as Combed Fenestration (CF). This model would provide a valuable platform with which to screen therapies aimed at reversing or halting the progress of chronic rotator cuff degeneration, while simultaneously allowing the comparison of the degeneration cascade through different injury modalities (i.e., as compared to enthesis damage). To enable direct comparison of this model to that tested in Specific Aim 2, the timepoints and analysis methodologies were replicated in this aim.

Specific Aim 4: Investigate the underlying mechanisms behind increased prevalence of rotator cuff repair failures in patients with osteoporosis.

As outlined in the Osteoporosis as a Risk Factor for Rotator Cuff Repairs section, human patients with osteoporosis experience elevated levels of rotator cuff repair failure; however, the underlying mechanism behind these failures is currently unknown. The goal of this aim was to explore changes to tendon mechanics and pathology in an ovine model of osteoporosis and compare those changes to what was found in Specific Aims 2 and 3. The goal of these comparisons was to elucidate

potentially similar pathway(s) responsible for the decreased rotator cuff repair surgical prognosis for patients with osteoporosis in the hopes that it could direct future work aimed at improving those repairs in OP patient populations.

Specific Aim 5: Characterize and correlate the biomechanical, histopathological, microstructural, and gene expression changes that occur naturally in human rotator cuff tendons.

Previous research has documented some biomechanical, histopathological, microstructural, and gene expression changes seen in human rotator cuff tendons as they age, yet none have performed these tests in a way that allows for the correlation of these data sets (i.e., there are no publications that have documented all of these data sets on the same samples). Furthermore, none have offered comparisons between changes seen in each of the four rotator cuff tendons. Therefore, the goal of this aim was to characterize and correlate the biomechanical, histopathological, microstructural, and gene expression changes that occur naturally in aging human rotator cuff tendons. This not only provided unique and new clinically relevant data, but it also served as validation for the models proposed in Specific Aims 2 and 3 while also providing the necessary data for Specific Aim 6.

Specific Aim 6: Utilizing computational modeling techniques, design a prototype instructive scaffold that approximates the gradient of mechanical properties seen in the human supraspinatus tendon.

As outlined earlier (Current Treatment Strategies and Future Improvement Opportunities), recent work has shown that mechanobiology can play an important role in driving the healing response after an injury. Scaffolds have previously been used as a means to bolster the time zero mechanical strength of a rotator cuff repair or to introduce biologically active compounds. However, no scaffolds have been designed that replicate the gradient of mechanical properties seen in a tendon insertion. As such, it is hypothesized that implementation of a scaffold with tailored mechanical properties will drive improved healing outcomes and graft incorporation in patients. Therefore, the goal of this aim was to use computational modelling techniques to design a prototype scaffold that has mechanical properties similar to human supraspinatus tendons (Specific Aim 5), providing the framework for future scaffold development that can potentially improve repair prognosis clinically.

Chapter 2- Partial Infraspinatus Tendon Transection as a Means for the Development of a Translational Ovine Chronic Rotator Cuff Disease Model¹

Background

Rotator cuff tears represent the most common soft tissue injuries in the shoulder, resulting in debilitating pain and dysfunction^(1-3,6). Around 250,000 rotator cuff tear repairs are performed annually in the USA, with a \$3.44B annual societal impact^(4,5). The original insult causing these types of tears can be multifaceted, but generally stem from an acute injury resulting in chronic degeneration or emanates from a combination of overloading and degeneration^(7,8). Despite advanced approaches for rotator cuff repair, most surgical repairs experience a wide spectrum of failure rates (20 – 94%)^(14,59).

To investigate the pathogenesis of rotator cuff injuries and potential therapeutic options, it is necessary to have controlled experimental models. At this time, there is not a reproducible animal model to perform translational research on the factors that influence the healing of a chronic, degenerative rotator cuff tear. Leporine⁽⁸²⁾, murine⁽⁹⁵⁾, canine⁽⁸³⁾, ovine⁽⁸⁴⁾, and non-human primates⁽⁸⁵⁾ have been proposed as potential animal model candidates for investigating the etiology and pathology of rotator cuff tears; however, none of these aforementioned models have been able to adequately emulate what is seen in chronically degenerated human tendons. Previous models have suffered from disadvantages such as incomparable healing rates^(88,95,96), dissimilar tendon

¹ Easley, J., et al. (2020). "Partial Infraspinatus Tendon Transection as a Means for the Development of a Translational Ovine Chronic Rotator Cuff Disease Model." *Veterinary and Comparative Orthopaedics and Traumatology*.

size (precluding ability to test human devices without scaling), tendon retraction, and increased magnitudes of tendon and muscle degeneration as compared to human tissues^(84,90,92).

The shortcomings in these models lead to a critical need to refine and re-develop a clinically relevant large animal model of the chronically degenerated rotator cuff injury. Although ovine shoulders lack an acromion arch, previous work has demonstrated that the infraspinatus tendon of the previous ovine models are an appropriate model for the human supraspinatus tendon, allowing devices designed for humans to be tested^(90,97). Unfortunately, previous ovine chronic large rupture models have been unsuccessful in mimicking what is seen in the human chronic massive-tear condition⁽⁹⁰⁾. Regardless, previous research by our group, and others, have shown that the ovine model still provides a more robust platform for evaluation of basic science questions, as well as a platform to develop novel orthopaedic devices or techniques^(3,65,68,92,98-102). However, the current chronic ovine rotator cuff tear model has limitations, including significant tendon retraction during the degeneration cascade and increased magnitudes of tendon and muscle degeneration as compared to human tissues^(84,90,92). The inability to anatomically oppose the tendon to its original insertion increases the difficulty of repair surgeries, which when combined with the severe degenerative changes, make it a less-than-ideal platform with which to investigate new devices such as orthobiologics designed for humans.

It has been shown that muscular and tendinous tissues will undergo degenerative changes if they are not loaded for an extended period⁽¹⁰³⁾. It was theorized that by unloading half of the tendon and attached muscle body via the partial transection method, sheep would be able to ambulate normally while ideally still inducing mild, degenerative changes similar to those seen in humans with a

chronic rotator cuff tear. Therefore, the purpose of this study was to evaluate the time-dependent changes occurring in an ovine infraspinatus partial tendon transection model (i.e., partial transection), with the ultimate goal of improving upon the translatability of current ovine chronic rotator cuff model (i.e., full transection). Specifically, the injury characteristics of a partially transected infraspinatus tendon model in sheep were compared to the injury characteristics of a chronically injured rotator cuff in humans. Additionally, it was thought that a partial rotator cuff tear of the sheep infraspinatus tendon would be more easily repairable than a full transection model following the degeneration period and that its characteristics (i.e., histopathologic changes) would more closely mimic chronic rotator cuff tendinopathy characteristics noted in humans.

Materials and Methods

All surgeries were performed at the Preclinical Surgical Research Laboratory at Colorado State University (Fort Collins, CO) under Institutional Animal Care and Use Committee (IACUC approval 15-6202A). Human tissue was collected from Rush Medical Hospital (Chicago, IL) under Institutional Research Board approval (IRB approval 16110707-IRB01).

Human ‘Model’ – Tissue Collection

Human tissue samples (20 x 10mm, with the smaller dimension aligned with tendon fibers) of the supraspinatus tendon were harvested from seventeen patients (n=17 samples) undergoing primary reverse shoulder arthroplasty. Due to the infeasibility of obtaining degenerated tissue during normal rotator cuff tear repair procedures, it was determined that this tissue would serve as the

most appropriate positive control of chronic rotator cuff tendinopathy in humans. This patient cohort had an average age of 68 ± 7 years, all demonstrated symptoms of chronic tendon degeneration and most had histories of previously failed rotator cuff tear repair surgeries. Tissue samples were collected intra-operatively and were placed in 10% neutral buffered formalin for fixation at the time of collection. Due to the IRB protocol for these patients and the nature of the surgery, muscle and musculotendinous junction specimens were not collected.

Ovine Model – Surgical Procedure

Six (n=6) skeletally mature *Ovis aries* ewes (≥ 3.5 years of age) were utilized in this study. Ewes were fed a grass/alfalfa mix hay and provided with tap water *ad libitum*. The sheep were divided between two sacrificial time points; three sheep were humanely euthanized at 6 weeks and three sheep at 12-week post-surgical (with respect to the creation of the tear).

All ewes were fasted 12 hours prior to surgery and premedicated with procaine G penicillin (3 million units/kg, subcutaneous (SQ) – PenOne Pro™, Norbrook Laboratories Limited, Newry, Ireland), oral phenylbutazone (1 gm oral (PO) – Bute Buloses, VEDCO, Inc., St. Joseph, MO, USA) and transdermal fentanyl patches (100 mcg, 50 mcg – Fentanyl Transdermal System, Watson Pharma, Inc., Corona, CA, USA; one patch applied to the forelimb) 24 hours before surgery.

The sheep were prepared for unilateral surgery and placed in left lateral recumbency under general anaesthesia. The skin over the right shoulder joint was prepared for aseptic surgery using alternating scrubs of povidone-iodine (Betadine) and alcohol. The shoulder joint was draped for aseptic surgery. A skin incision approximately 12 cm in length was made over the point of the shoulder. The *m. subcutaneous coli* was divided in line with the incision and the *m. deltoideus* was split along the tendinous division between the heads of the acromion and scapula. The superficial head and insertion of the infraspinatus tendon was isolated, followed by sharp transection/detachment of the cranial 50% of the infraspinatus tendon at its insertion to the greater tuberosity of the humerus (Figure 6A). This portion of the tendon was chosen as the transection region at this location was deemed to be repeatable during surgery. The released portion of infraspinatus tendon was then capped/wrapped with an approximately 3 cm x 3 cm patch of Gore-Tex™ using metric 3 Nylon in a mattress pattern (Figure 6B). The purpose of the Gore-Tex™ was to inhibit scarring of the tendon to the surrounding soft tissue, while still allowing some nutrition to diffuse to the covered aspect of the tendon^(3,104).

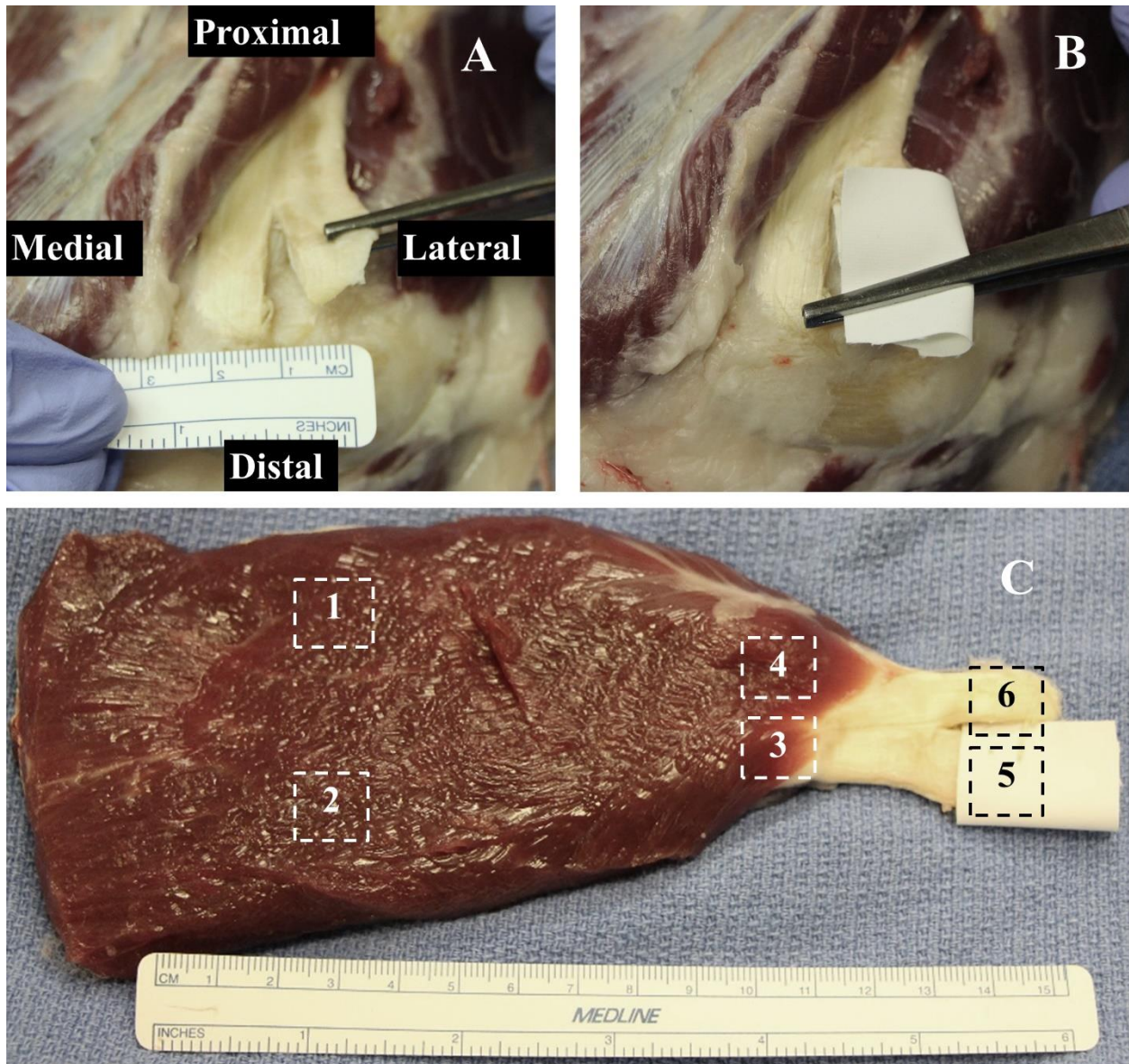


Figure 6. Surgical photos (A) Transected infraspinatus tendon capped with Gore-tex™, (B) Uncapped transected infraspinatus tendon, (C) Histologic biopsy locations. (1) Proximo-lateral muscle, (2) Proximo-medial muscle, (3) Disto-medial musculotendinous junction, (4) Disto-lateral musculotendinous junction, (5) Transected medial tendon (shown capped with Gore-Tex™), (6) Non-transected lateral infraspinatus tendon.

The capped end of the tendon was not re-attached to the original site of insertion on the humerus (Figure 6B). Two 1.2 mm Kirschner wire markers were inserted along the lateral edge of the

humeral insertion site to serve as anatomical landmarks indicating the site of partial transection. After Kirschner wire insertion, the brachial fascia and subcutaneous tissues were closed as separate layer using 2-0 absorbable suture material (Polysorb), followed by skin closure with stainless steel staples. Following complete recovery, the sheep were allowed to eat and ambulate *ad libitum*. The sheep were monitored daily throughout the study period for any signs of adverse events or complications and to evaluate pain, lameness/ambulatory function, and incisional site healing.

Surgical Assessment after 6 or 12 Weeks of Healing

Prior to sacrifice of both the 6 and 12-week time point animals, surgical assessment of scar tissue formation of the capped portion (i.e., was the scar tissue removable or affixed) and tendon retraction measurement were performed under general anaesthesia. After the *m. deltoideus* was split along the tendinous division between its acromial and scapular head, the acromial head of the *m. deltoideus* was reflected with malleable retractors. Overlying fibrous scar tissue was dissected away, and the Gore-Tex™ patch capping the transected portion of the infraspinatus tendon was localized and removed. The capped portion of tendon was assessed, and the retraction distance from the proximal end of the tendon to the anatomical insertion on the humeral head was measured (utilizing a sterile surgical ruler). Surgical reattachment of the transected portion was simulated by two board certified veterinary surgeons and a medical doctor familiar with the acute repair technique. This “simulation” served as a means to determine the relative level of tension required to achieve normal tendon apposition to the anatomical insertion of the humeral head, thus providing insight into the potential feasibility of repair surgery (a necessity for utilizing this animal model to test orthopaedic devices in a pre-clinical setting). Following the surgical assessment, all

animals were humanely euthanized, and the infraspinatus tendon samples were collected within one hour of sacrifice. Samples were then placed in 10% neutral buffered formalin for fixation.

Histological Analysis

Tendon biopsies from both the transected and non-transected sides were taken from the proximal end of the tendon (approximately 1cm in length) (Figure 6C). Muscle and myotendinous junction specimens were obtained from locations outlined in Figure 6C. Following the tissue collection and fixation for both the human and ovine samples, standard paraffin-embedding techniques were used, and one section was cut through the midportion in the sagittal plane from each formalin-fixed sample and stained with hematoxylin & eosin. Hematoxylin & eosin stain was used to highlight and quantify the amount of muscle and fat within the samples. Sections were evaluated using a semi-quantitative scoring system based on an adaptation of the scheme put forth by Long et al⁽³⁷⁾. As samples were collected in close proximity to the enthesis of the tendon, care was taken to analyze both proximal and distal aspects of the tendon to ensure that any variations in structure and constituents were not structural or cellular changes associated with the insertional region of the tendon. Tenocyte reactivity, stromal cell proliferation, inflammation, neo-vascularization, discreteness of muscle-tendon junction, and myocyte degeneration/atrophy were evaluated. Slides were scored on a five-point scale where zero corresponds to normal, 1 with minimal change, 2 with mild change, 3 with moderate change, and 4 with severe change as compared to healthy controls. A board-certified veterinary pathologist unblinded to species but blinded to tendon/muscle section (medial versus. lateral) performed the histopathological analysis on all samples. The pathologist who performed the analysis of the specimens in this study utilized

samples from previous studies^(3,65,68,71,92,102) to generate and calibrate to a baseline of uninjured ovine tendons before performing the analysis on the specimens in this study.

As this study was intended to be a pilot study, the low sample size of each experimental group precluded meaningful statistical analysis of the results. Therefore, all results are reported as mean \pm standard deviation.

Results

All six animals survived to the 6 and 12-week time points with 3 shoulders being used from each time point. No intra- or post-operative complications were noted. At both time-points the capped portion of the tendon was covered with a moderate amount of scar tissue that was easily removed via surgical dissection to expose the Gore-Tex™ capped tendon.

Reattachment of Medial Half of Tendon

At the 6-week time point, the detached portion of the infraspinatus tendon was able to be re-attached to the humeral footprint to create an anatomically correct repair (3 out of 3 samples); the average retraction of the detached portion at the 6-week time point was 1.6 ± 0.2 cm (mean \pm standard deviation). It was not possible to re-attach the infraspinatus tendon to the humeral footprint at the 12-week time point due to significant retraction (2.2 ± 0.6 cm) and fibrosis of the detached tendon section (2 out of 3 samples).

Histology Results

Tendon Region

The medial infraspinatus tendon section within the ovine model that underwent transection (Figure 7B) was primarily composed of stromal cell proliferation and tenocyte reactivity, the latter was characterized by tenocytes containing large nuclei with open chromatin and increased numbers of plump, reactive, mesenchymal/stromal cells, often times arranged in dense streaming bundles which separated and replaced normal tendon collagen (Figure 7C and D). The ovine 12-week transected and human samples had mild-moderate changes in the tenocyte reactivity and stromal cell proliferation category, demonstrating a decrease from the 6-week timepoint which had moderate-severe changes (Table 1). Multifocally, ovine tendon collagen also frequently appeared degenerate, characterized by loss of the tightly packed parallel fiber arrangement, collagen fiber pallor, with increased waviness, separation, and disorganization of collagen bundles (Figure 7C and D). Both the 6 and 12-week samples showed similarity to what was seen in the human condition regarding levels of inflammation (mild level), although they were still graded as slightly

more inflamed than the human condition (minimal) (Table 1). All ovine tendon samples demonstrated evidence of neo-vascularization, characterized by the presence of variably sized blood vessels lined by plump endothelium, often located between parallel bundles of collagen

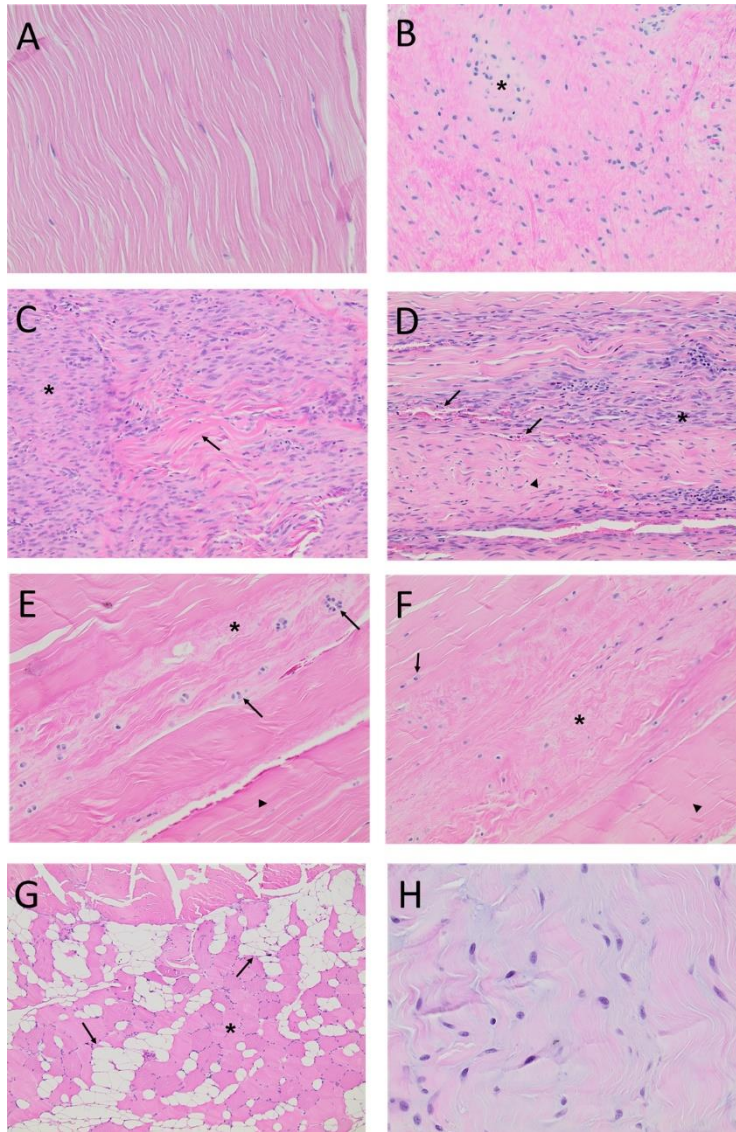


Figure 7. Photomicrographs of hematoxylin and eosin stained human and ovine tendons. (A) Normal infraspinatus tendon, 20x. (B) Human rotator cuff supraspinatus tendon, 10x. Asterisk = cartilaginous metaplasia. (C) and (D) Transected portions of the sheep infraspinatus tendon, 10x. Asterisk = proliferations of stromal cells. Arrowhead = palestaining collagen fibers. Arrows = neo-vascularization. (E) and (F) Non-transection portions of the sheep infraspinatus tendon, 10x. Asterisk = collagen fiber structure, arrows = nuclei per lacunae. (G) Proximo-medial aspect of the sheep infraspinatus musculotendinous junction, 10. Asterisk = myocyte bundles, arrows = adipocytes. (H) Mucinous degeneration, 20x.

(Figure 7D). Overall, ovine samples scored higher than the human samples in the tendon neo-vascularization category (Table 1). In the ovine samples, infiltrates of mononuclear inflammatory cells, primarily composed of lymphocytes, with fewer plasma cells and rare macrophages, were often present between collagen bundles and surrounding neo-vessels (Figure 7C and D).

Table 1. Histologic scoring of tendon biopsies. Human samples N=10. Ovine 6 and 12-week, transected and non-transected samples N=3.

		Human	Ovine: 6-Week	Ovine: 12-Week	
		Mean ± SD	Mean ± SD	Mean ± SD	
Tendon Histologic Scoring	Inflammation	0.59 ± 0.87	1.83 ± 0.85	1.00 ± 0.00	Transected
			1.50 ± 0.71	1.33 ± 0.47	Non-Transected
	Neo-Vascularization	2.24 ± 1.03	3.67 ± 0.47	3.33 ± 0.94	Transected
			3.00 ± 0.00	3.00 ± 1.41	Non-Transected
	Tenocyte Reactivity & Stromal Cell Proliferation	2.44 ± 0.79	3.67 ± 0.47	2.67 ± 0.94	Transected
			3.33 ± 0.47	2.00 ± 0.82	Non-Transected

In contrast, histological changes within the lateral (non-transected) ovine infraspinatus tendon (Figure 7E and F) were typified by a less inflamed and reactive process, but instead more chronic degenerative histological changes. These changes were characterized by diffuse pallor, marked separation, and haphazard arrangement of collagen bundles, with loss of collagen fiber structure.

All of these lateral tendon sections also contained multifocal regions of mucinous degeneration of collagen, and multifocally, tenocytes and their nuclei resembled chondrocytes and were forming clusters of chondrocytes with multiple nuclei per lacunae, consistent with chondroid metaplasia.

In brief, the most consistent histological feature present within the human tendons was the loss of the tight, parallel organization of collagen bundles, with haphazard arrangement, fibrillation, and separation of collagen fibers. Additionally, multifocal regions of increased tenocyte reactivity and stromal cell proliferation were also present, again characterized by increased overall tendon cellularity, enhanced prominence of tenocytes between collagen bundles, and occasional streaming bundles of plump, reactive mesenchymal cells. In addition, the overall tinctorial properties of the tendon collagen was markedly different from normal tendons, characterized by diffuse pallor (pale pink staining) which coincided with marked loss of normal collagen bundle architecture and the presence of variably sized regions of chondroid metaplasia and mucinous degeneration, and less frequently, smaller foci of collagen hyalinization. Multifocal, mild neovascularization was present in the majority of samples, while inflammation was minimal to often times essentially non-existent (Figure 7A). Similar gross histological findings were noted across all animals at both 6 and 12-weeks and severity of tendon changes did not seem to progress beyond the 6-week healing period (Figure 7C, D, E, and F).

Musculotendinous Junction Region

For human patients, only tendon tissue samples were obtainable due to the nature of the primary reverse shoulder arthroplasty; thus, comparisons of ovine muscle and musculotendinous regions to human tissues could not be performed. Importantly however, the infraspinatus

musculotendinous junction in this sheep model was characterized by varying degrees of infiltration and separation of myocyte bundles by adipocytes. Also present were multifocal areas of myofiber atrophy and fibrosis. These pathological changes observed within the proximal infraspinatus muscle and musculotendinous junction, are somewhat similar to those described for “fatty atrophy” of human rotator cuff muscles⁽¹⁰⁵⁾ (Figure 7G). The data demonstrated that the level of neo-vascularization decreased slightly on the transected side of the musculotendinous junction during the final 6 weeks of the study. Similarly, tenocyte reactivity and stromal cell proliferation decreased in going from the 6-week to 12-week time-point on the transected and non-transected portion (Table 2).

Table 2. Histologic scoring of musculotendinous junction and muscle biopsies. Ovine 6 and 12-week, transected and non-transected samples N=3.

		Ovine: 6-Week	Ovine: 12-Week		
		Mean ± SD	Mean ± SD		
Musculotendinous Junction	Discreteness of Muscle-	2.50 ± 0.87	1.67 ± 0.47	<i>Transected</i>	
	Tendon Junction	1.00 ± 0.82	1.50 ± 0.50	<i>Non-Transected</i>	
	Neo-Vascularization		1.25 ± 0.43	1.00 ± 0.00	<i>Transected</i>
			0.33 ± 0.47	0.50 ± 0.50	<i>Non-Transected</i>
	Tenocyte Reactivity & Stromal Cell Proliferation		2.75 ± 0.83	1.00 ± 0.00	<i>Transected</i>
			1.00 ± 0.82	0.50 ± 0.50	<i>Non-Transected</i>
	Muscle	Inflammation &	1.08 ± 0.84	0.83 ± 0.69	<i>Transected</i>
		Cellular Composition	0.20 ± 0.40	0.17 ± 0.37	<i>Non-Transected</i>
Neo-Vascularization			0.92 ± 0.45	0.50 ± 0.50	<i>Transected</i>
			0.00 ± 0.00	0.17 ± 0.37	<i>Non-Transected</i>
Myocyte		2.17 ± 0.69	1.83 ± 0.69	<i>Transected</i>	
Degeneration / Atrophy		0.80 ± 0.75	1.42 ± 0.61	<i>Non-Transected</i>	

Infraspinatus Muscle Region

Evaluation of the histological scoring of the infraspinatus muscle biopsies demonstrated a clear difference in the degree of inflammation between the transected and non-transected sides at both 6 and 12 weeks, with the non-transected side showing minimal to no evidence of inflammation. The level of atrophy seen on the transected side was much greater than the non-transected side at the 6-week time point (

Table 2). The muscle tissue from the transected half had a noticeably increased degree of neovascularization as compared to the non-transected portion.

Discussion

This translational animal model development study described an ovine model of chronic rotator cuff degeneration. To our knowledge this is the first study to include serial histological analysis of the pathological effects on the tendon originating muscle at multiple time points^(70,106). As compared to the degenerated human condition, sheep tendons were characterized by a more acute to subacute reactive and reparative pathological process, as evidenced by increased inflammation, neovascularization, and markedly increased tenocyte reactivity and stromal cell proliferation. These changes were most evident within the transected infraspinatus tendon. In contrast, histological changes within the human tendons evaluated in this study were characterized by more diffuse, chronic, degenerative changes, which contrasts with the acute, reactive, and reparative changes more frequently observed in the transected portions of the sheep tendons. Unexpectedly, we observed that these histological changes in our human rotator cuff tendon samples appeared more similar to those observed in the lateral non-transected sheep infraspinatus tendons, which were also predominantly characterized by chronic degeneration of tendon collagen, with pale staining, separation, and haphazard arrangement of collagen bundles. As compared to the transected portion of the tendon, the non-transected infraspinatus tendon showed more mild changes, which appeared more chronic and degenerative in nature as opposed to the reactive/reparative changes observed for the transected tendons.

Other studies have noted similar pathological findings in partial tendon transection ovine models. Smith et al performed a partial tendon transection ovine model and analyzed histological results at the 4-week time point⁽¹⁰⁶⁾. While this was a shorter time point than what we had analyzed, increased vascularity and decreased collagen fiber alignment were likewise noted. Another large animal partial tendon transection model was tested by Derwin et al, which found comparable levels of tendon retraction in their canine model⁽⁷⁰⁾. Increased cellularity was also a key finding of a rat model of partial transection⁽¹⁰⁷⁾. Jacobsen et al. utilized a partial equine flexor tendon injury to investigate changes that occur in both the injured and non-injured halves of the tendon. They found that there were no significant differences between pathologic parameter between the transected and non-transected sides of the tendon. This is in contrast to what was observed in this ovine model. Specifically, pathologic changes (e.g., inflammation and cellularity) were observed in both sides of the ovine tendon, with these changes being more severe in the transected⁽¹⁰⁸⁾.

As with all translational animal models, there are limitations correlating the results from this study to clinical human cases. The main limitation of this study is that our low sample size (n=3 tendons at each time points) resulted in low statistical power (0.22), which precludes statistical conclusions and analysis of further time-points. This study compared the transected and non-transected sides of the muscle, musculotendinous junction, and tendon; however, only half of the tendon was transected. Since the distal portion of the tendon was not split in half (and therefore was still attached), the degenerative effects may be seen in both sides of the muscle and musculotendinous junction. As previously mentioned, human tissue samples were limited to only tendon, therefore a direct comparison between human and ovine muscle and musculotendinous sections was not possible. One of the primary purposes of preclinical models is to analyze the effects of different

treatments in repair scenarios. Due to the level of tendon retraction seen, reattachment of these ovine tendons at delayed timepoints during any subsequent repair surgeries would most likely be infeasible. As such, the testing of musculoskeletal implants in a delayed setting utilizing this model would be intractable, thus significantly impairing the usefulness of this model.

Development of a more clinically translatable chronic rotator cuff injury model is critical to advancing the surgical and medical treatment of human rotator cuff tears. Currently, there remains no reproducible large animal model to perform translational research investigations on factors that influence healing of a chronic, degenerative rotator cuff tear. While this model does not completely emulate all aspects of chronic tendon degeneration seen in humans, it has the advantage of having a tendon of similar structural characteristics as the human supraspinatus tendon, allowing for the study of safety and efficacy of controlled variables including implantable devices, cellular therapies, prevention of degenerative changes, rehabilitation options, or novel surgical techniques.

Chapter 3- Enthesis Trauma as a Means for the Development of Translatable Chronic Rotator Cuff Degeneration in an Ovine Model²

Background

The rotator cuff is a group of tendons in the shoulder that are responsible for stability and motion of the arm; tears to these tendons can cause pain, instability, and an inability to perform day-to-day tasks. Previous studies of cadaveric shoulders have found that 18.5% of the general population has at least partial tears of rotator cuff tendons^(9,10). As these partial tears do not typically result in significant impairment of the arm, conservative treatment is generally implemented in lieu of surgical repair⁽¹¹⁾. However, growing clinical and basic science evidence suggests that these partial tears result in a deleterious degenerative cascade of the rotator cuff tendon / muscle group, leading to fatty infiltration, loss of muscle strength, and most importantly, increased probability of full thickness tears at a later point in life^(12,13). Additionally, this chronic degeneration of the tendon(s) (a.k.a., tendinopathy) has a negative impact on the clinical outcome of repair surgeries on torn tendons, with re-tear rates of arthroscopic repairs as high as 94% depending on exacerbating risk factors⁽¹⁴⁻¹⁷⁾.

The etiology of chronic tendon degeneration is complex, and the mechanistic underpinnings are not yet fully understood. Chronic degeneration is known to entail several pathological changes in tendons, including a proliferation of tenocytes, excess proteoglycan content, disorganized collagen fibers, and increased vascularization⁽³⁶⁻³⁹⁾. Changes are not limited to the tendon tissue; marked

² Johnson, J., et al. (2021). "Enthesis trauma as a means for the development of translatable chronic rotator cuff degeneration in an ovine model." *Annals of Translational Medicine* 9(9): 741-741.

fatty infiltration of the associated muscle groups is another hallmark of rotator cuff degeneration. There is no consensus on a single underlying cause leading to chronic rotator cuff degeneration, but it is hypothesized that the degeneration cascade stems from factors such as overuse or history of tendon injury (i.e., previous partial width tears)^(50,51).

The poor prognosis and high frequency of rotator cuff damage necessitates continued research into new surgical techniques and therapeutics to improve upon currently inadequate clinical outcomes. A variety of translational comparative animal models (e.g., murine, leporine, canine, ovine, and non-human primates) have been used in attempts to simulate the human degeneration cascade; however, none have been able to faithfully recapitulate the broad spectrum of changes that are seen in humans⁽⁸¹⁻⁸⁵⁾. Furthermore, the inherently small size of some of these animal models (i.e., ‘small animals’) precludes the assessment of physiologically-relevant sized devices or comparable dosages of cellular therapies intended for use in humans. This has led some researchers to propose the use of ewes as a translational model for rotator cuff injury^(71,90,91). One of the first ovine models used as a means to generate degenerative changes to tendons in the rotator cuff involved a full transection of the infraspinatus tendon with a delayed repair⁽⁹²⁾. While this model was considered the gold-standard for some time^(3,92,93), it has since been demonstrated that this model leads to severe tendon retraction, which is not observed clinically and results in repair surgery complications⁽⁹⁴⁾. To overcome this shortcoming, a partial transection model in which half of the infraspinatus’ width was transected from the enthesis, followed by a delayed repair was created^(70,83,91,106). Unfortunately, this model was also found to create pathologic changes that are best described as an acute reparative injury process (amplified tenocyte reactivity, neo-

vascularization, and inflammation), in contrast to what has been noted clinically in patients with tendinopathy⁽¹⁰⁹⁾ ⁽¹¹⁰⁾.

Considering the inability of the current large-animal translational models to accurately replicate the chronic, degenerated human condition (i.e. haphazard collagen organization, increased cellularity, increased vascularity, etc.⁽¹¹¹⁾), there is a clear need to explore new models that can more closely replicate the magnitude and characteristics of the human tendon degeneration cascade. Therefore, the purpose of this study was to investigate a novel ovine model of chronic rotator cuff degeneration. We hypothesized that surgically induced damage at the tendon-bone enthesis (i.e., sharp surgical transection through 50% of the enthesis; akin to a partial tear), while still leaving the entire width of the tendon attached, would initiate a degree of degeneration which parallels that observed in degenerated human tendons clinically, as evidenced by comprehensive biomechanical, histopathological, histomorphological, and gene expression analyses. The rationale for this approach was that by leaving the entire width of the tendon attached (as opposed to previous full or partial transection models), the severity of pathologic changes would more closely match what has been documented in human cases. We present the following article in accordance with the MDAR reporting checklist.

Methods

All surgeries were performed with approval from Institutional Animal Care and Use Committee (IACUC, Colorado State University #18-7854A). Human tissue was collected with Institutional Research Board approval (IRB, Rush Medical University #16110707-IRB01).

Human tissue collection

Human supraspinatus tendon tissue (10 x 20 mm; length x width) was obtained from seventeen patients (n=17 samples) undergoing primary reverse shoulder arthroplasty (PRSA). Inclusion criteria were that the patients were undergoing PRSA and had indications of chronic, degenerative rotator cuff tendinopathy. All patients gave informed consent prior to taking part in this study. PRSA was performed on arthritic patients with well documented chronic rotator cuff injuries. Succinctly, the rotator cuff injuries in these patients are often severe and the tendons exhibit symptoms of chronic degeneration that would prohibit normal shoulder motion if a normal arthroplasty were performed^(112,113). Due to the severe level of degeneration, portions of rotator cuff tendons must be removed, enabling tissue collection for this study. This patient cohort had an age of 68 ± 7 years, all demonstrated clinical signs of chronic tendon degeneration (i.e., MRI assessment of tendon injury including fatty infiltration of the associated muscles⁽¹¹⁴⁾) and some having histories of previously failed rotator cuff tear (RCT) repair surgeries (6 out of 17 patients). Tissue samples were collected intra-operatively and were placed in 10% neutral buffered formalin for fixation at the time of collection. Collected and fixed samples were allocated to histopathologic assessment. Due to the small size of tissue biopsies, it was deemed infeasible to mechanically test the human tissue samples. Previously published gene expression data from human subjects with

chronic tendon degeneration was used as a representative population for genetic expression comparisons⁽⁴¹⁾.

Ovine model – surgical procedures

Bilateral surgical damage was created to the infraspinatus tendons in twenty skeletally mature (≥ 3.5 years of age) *Ovis aries* ewes resulting in n=40 treated shoulders. Rams were not utilized in this study due to husbandry difficulties and aggressive behavior. The sheep were prepared for bilateral surgery and placed in dorsal recumbency under general anesthesia. The surgical models (model 1: sharp partial transection of the entheses (n=20 treated shoulders); model 2: combed fenestration of the enthesis and tendon mid-substance (n=20 treated shoulders – data not shown in this manuscript)) were alternated between shoulders to eliminate the potential of a left/right side bias.

A standard surgical preparation and approach was followed; the *m. subcutaneous coli* was divided in line with the incision, and the *m. deltoideus* was split along the tendinous division between the heads of the acromion and scapula. The superficial head and insertion of the infraspinatus tendon was isolated, followed by creation of the surgical insult. The enthesis damage model, “sharp transection” (ST), was generated by cutting the tendon fibers perpendicularly through the midportion of the attachment site on the humerus (i.e., the footprint) (Figure 8). This was done to simulate damage at the tendon insertion that does not result in a complete separation of the tendon from the humerus, similar to what is hypothesized to occur in humans that have suffered a partial

thickness tear at the enthesis. Following model generation, standard surgical closure procedures were followed. The sheep were allowed to eat and ambulate *ad libitum* during convalescence. Sheep were monitored daily throughout the study period for any signs of adverse events or complications and to evaluate pain, lameness/ambulatory function, and incisional site healing.

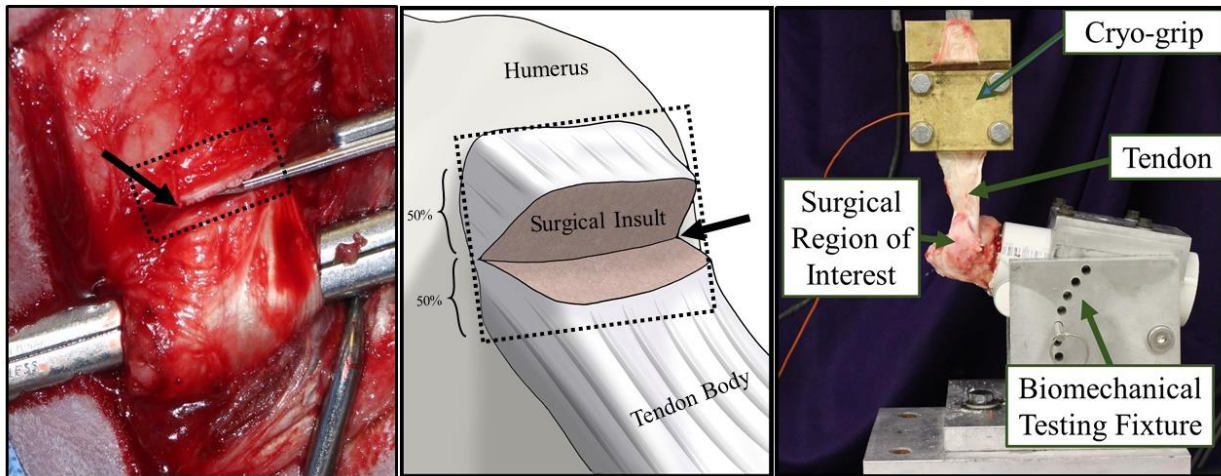


Figure 8. Intra-operative image illustrating location of surgical insult at the midpoint of the tendon insertion (left) and digital illustration of surgical insult and relevant tissue (center). Rectangular box outlines the tendon insertion, arrow highlights the surgical cut. Image of biomechanical testing (right).

Animals were humanely euthanized at 6, 12, and 18-weeks. The humerus-infraspinatus tendon constructs (HTCs) were immediately harvested following euthanasia. Six uninjured shoulders were harvested from sheep utilized in unrelated studies to use as controls. HTCs were isolated and denuded of soft tissues with great care as to not damage the infraspinatus tendon. A small portion (5mm x 20mm, width x length) of tendon on the caudal/ventral side was taken immediately upon dissection and snap frozen in liquid nitrogen to be used for RNA sequencing. Pilot experiments

(data not shown) demonstrated that RNA biopsy collections did not compromise the mechanical competency of the tendon.

Biomechanical testing

Three cross-sectional area (CSA) measurements of all tendons were taken proximal to the insertion with an area micrometer that applied 0.12 MPa of load parallel to the cross section of the tendon^(68,71,115,116). The minimum of these CSA measurements was used to transform force to stress, resulting in values that indicate the highest level of stress in each tendon. For purposes of reporting tendon overall cross-sectional area, these measurements were averaged. The humeri were subsequently mounted in polyvinyl chloride (PVC) sleeves using a strong two-part hard casting resin (SmoothCast 321, Smooth-On, Macungie, PA) and mounted in a custom fixture attached to a servo-hydraulic load frame (Model 805, MTS Corp., Eden Prairie, MN) which allowed anatomically accurate loading of the tendon (Figure 8)^(3,71). Prior to biomechanical testing, tendons underwent a pre-loading phase to normalize viscoelastic effects in which a static preload of 5N was applied for a duration of two minutes^(68,117-121). Gage length of the tendon was measured at the end of the preload period, allowing transformation of the testing data from displacement to stretch. Non-destructive stress relaxation tests were then performed for 100 seconds at physiologically relevant stretch levels of 1.06 and 1.08^(120,122), with peak stress (MPa), peak force (N), and percent relaxation (%) being measured⁽¹²³⁾. Recovery periods of 1,000 seconds between tests were implemented to allow samples to come to viscoelastic equilibration⁽¹²⁰⁾. Tendon hydration was maintained with physiological saline during the entire preparation and mechanical testing procedure.

Histological analysis

Immediately following mechanical testing, samples were removed from their potting sleeves and bisected through the enthesis to improve infiltration of the fixative agent⁽⁷¹⁾. These humerus-infraspinatus tendon constructs were then fixed in 10% neutral buffered formalin (≥ 7 days), demineralized in 8% trifluoroacetic acid, embedded in paraffin, sectioned at the mid-tendon-body, and mounted on a glass slide. Two 5 μm thick slides were cut from each sample; one slide was stained with hematoxylin and eosin (H&E) and the other slide was stained with Picro-Sirius red.

H&E slides were graded by a blinded veterinary pathologist in residency using the semiquantitative Bonar tendinopathy scale via bright-field and polarized light microscopy assessing: (1) tenocyte reactivity, (2) angiogenesis, (3) tendon bundle organization and polarization, and (4) deposition of ground substance⁽⁴⁰⁾. Each of these four characteristics were graded on a 4-point scale ranging from 0 (normal/healthy) to 3 (markedly “degenerated” / pathologic)⁽⁴⁰⁾. These scores were then summed to give an overall score between 0 (pathologically normal) and 15 (pathologically degenerated) for each tendon section.

Histomorphological assessment of collagen fiber alignment

Picro-Sirius red stained slides were utilized to assess collagen fiber organization in all ovine and human tissues. Slides contained 40 mm of the proximal infraspinatus tendon and enthesis/bone

were prepared and imaged using polarized brightfield microscopy at 2x magnification (Olympus BX61VS, Center Valley, PA). All samples were imaged in one session with 40ms exposure to ensure no variation in imaging capture process or polarization lens configuration. A complex machine learning algorithm (Image-Pro Plus, RRID:SCR_007369) was programmed to calculate percent area of the organized / disorganized collagen seen within the injury region of the tendon. Region of analysis included the most proximal 25mm of tendon but did not include the fibrocartilaginous enthesis zone. To ensure the accuracy of the program the veterinary pathologist in residency verified the algorithm's ability to differentially identify organized and disorganized regions of collagen for a subset of samples.

RNA sequencing

Tendon samples for gene expression analysis were taken immediately during fine dissection and flash frozen in liquid nitrogen to prevent RNA degradation. Tendon samples were pulverized then lysed (TRizol™ Invitrogen, Carlsbad, CA) to enable precipitation of RNA followed by purification using chloroform method as previously described⁽¹²⁴⁾ with increased incubation time to account for the size of the tendon biopsy. Commercially available kits (RNeasy, Qiagen, Hilden, Germany) were then used to purify extracted RNA following manufacture protocol.

Frozen RNA samples were sent to a commercial genomics center (Novogene Inc., Sacramento, CA) for quality analysis and sequencing. RNA quality was verified by electrophoresis (2100 Bioanalyzer Instrument, Agilent, Santa Clara, CA). The cDNA library was constructed with a

commercially available kit following manufactures instructions (Ribo-Zero, Illumina, San Diego, CA). Paired end reads were obtained (HiSeq 2500, Illumina, San Diego, CA), and gene expression data were processed using a statistical and visualization analyses package (Partek Genomics Suite, RRID:SCR_011860). After adapter trimming and filtering for Phred score >20, paired end reads were aligned to **Oar_v3.1 genome assembly** using TopHat⁽¹²⁵⁾. Gene counts were obtained using Partek E/M annotation model. Differentially expressed genes were calculated for each timepoint compared to uninjured samples using Partek GSA (gene specific analysis) and non-parametric ANOVA.

Statistical analysis

All comparisons between groups were made using a one-way ANOVA followed by Fisher's *post-hoc* test (Minitab, RRID:SCR_014483). All data passed Anderson-Darling normality test. Data that did not pass Levene test for equal variance were transformed with Box Cox transformation. Final sample sizes were chosen to achieve 80% statistical power using results from pilot animals. Sample numbers in each grouping were: n=6 shoulders at the 6 and 12-week timepoints, n=8 shoulders at the 18-week timepoint, and n=6 shoulders for the uninjured control group. Ewes were randomly assigned to sacrifice timepoints. No specimens/samples were excluded from this study. Correlation analysis were performed, results of Pearson correlation coefficients and associated P-values were reported.

Results

All twenty animals survived to the 6, 12, and 18-week timepoints. No intra- or post-operative complications were noted.

Mechanical Testing

There were marked, significant increases in cross-sectional area (CSA) at all timepoints as compared to the uninjured control group with the ST tendons exhibiting increases in CSA of 60.3% (P=.038), 62.5% (P=.032), and 58.8% (P=.032) at the 6, 12, and 18-week timepoints, respectively (Figure 9). Additionally, the ovine tendons that underwent sharp transection demonstrated decreased biomechanical properties (*Table 1*). At all timepoints the injured tendons exhibited marked, significant reductions in peak stress at both stretch levels (Figure 9), with the ST tendons exhibiting decreases of: 50.0% (6-wk, $\lambda=1.06$, P=.036), 65.9% (6-wk, $\lambda=1.08$, P=.001), 69.1% (12-wk, $\lambda=1.06$, P=.005), 74.2% (12-wk, $\lambda=1.08$, P=.001), 45.6% (18-wk, $\lambda=1.06$, P=.037), and 61.4% (18-wk, $\lambda=1.08$, P=.001). The viscous response of the tendons was also altered, with increases in percent relaxation (as compared to uninjured) at both stretch magnitudes (Figure 9), with the ST tendons exhibiting decreases of: 69.6% (6-wk, $\lambda=1.06$, P=.024), 51.7% (6-wk, $\lambda=1.08$, P=.115), 96.5% (12-wk, $\lambda=1.06$, P=.003), 52.5% (12-wk, $\lambda=1.08$, P=.110), 88.7% (18-wk, $\lambda=1.06$, P=.003), and 73.1% (18-wk, $\lambda=1.08$, P=.021).

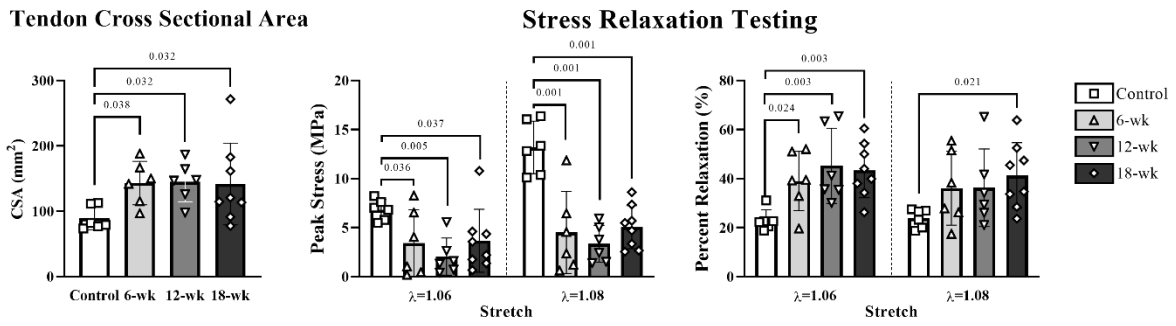


Figure 9. (Left) Tendon cross-sectional area (CSA) measurements. (Middle) Peak stress from the stress-relaxation testing at both stretch levels. (Right) Percent relaxation from the stress-relaxation testing at both stretch levels. P-values are indicated for all pairwise comparisons which met the significance threshold ($P < 0.05$).

Table 3. Biomechanical and geometric properties for tendon samples. Data are shown as means \pm SD.

Timepoint	Stretch	Percent Relaxation (%)	Peak Load (N)	Peak Stress (MPa)	Area (mm²)
Control	$\lambda=1.06$	23.0% \pm 3.9% (-)	582 \pm 101 (-)	6.8 \pm 1 (-)	89.3 \pm 16.3 (-)
	$\lambda=1.08$	23.8% \pm 3.5% (-)	1108 \pm 161 (-)	13.2 \pm 2.4 (-)	
6 Weeks	$\lambda=1.06$	39.0% \pm 11.0% (0.02)	438 \pm 372 (0.38)	3.4 \pm 3.1 (0.04)	143.1 \pm 30.4 (0.04)
	$\lambda=1.08$	36.1% \pm 13.7% (0.11)	564 \pm 396 (<0.01)	4.5 \pm 3.8 (<0.01)	
12 Weeks	$\lambda=1.06$	45.2% \pm 14.0% (<0.01)	281 \pm 228 (0.07)	2.1 \pm 1.7 (<0.01)	145.1 \pm 28.0 (0.03)
	$\lambda=1.08$	36.3% \pm 14.4% (0.11)	457 \pm 269 (<0.01)	3.4 \pm 1.7 (<0.01)	
18 Weeks	$\lambda=1.06$	43.4% \pm 10.4% (<0.01)	342 \pm 246 (0.12)	3.7 \pm 3 (0.04)	141.8 \pm 58.7 (0.03)
	$\lambda=1.08$	41.2% \pm 12.6% (0.02)	490 \pm 137 (<0.01)	5.1 \pm 2 (<0.01)	

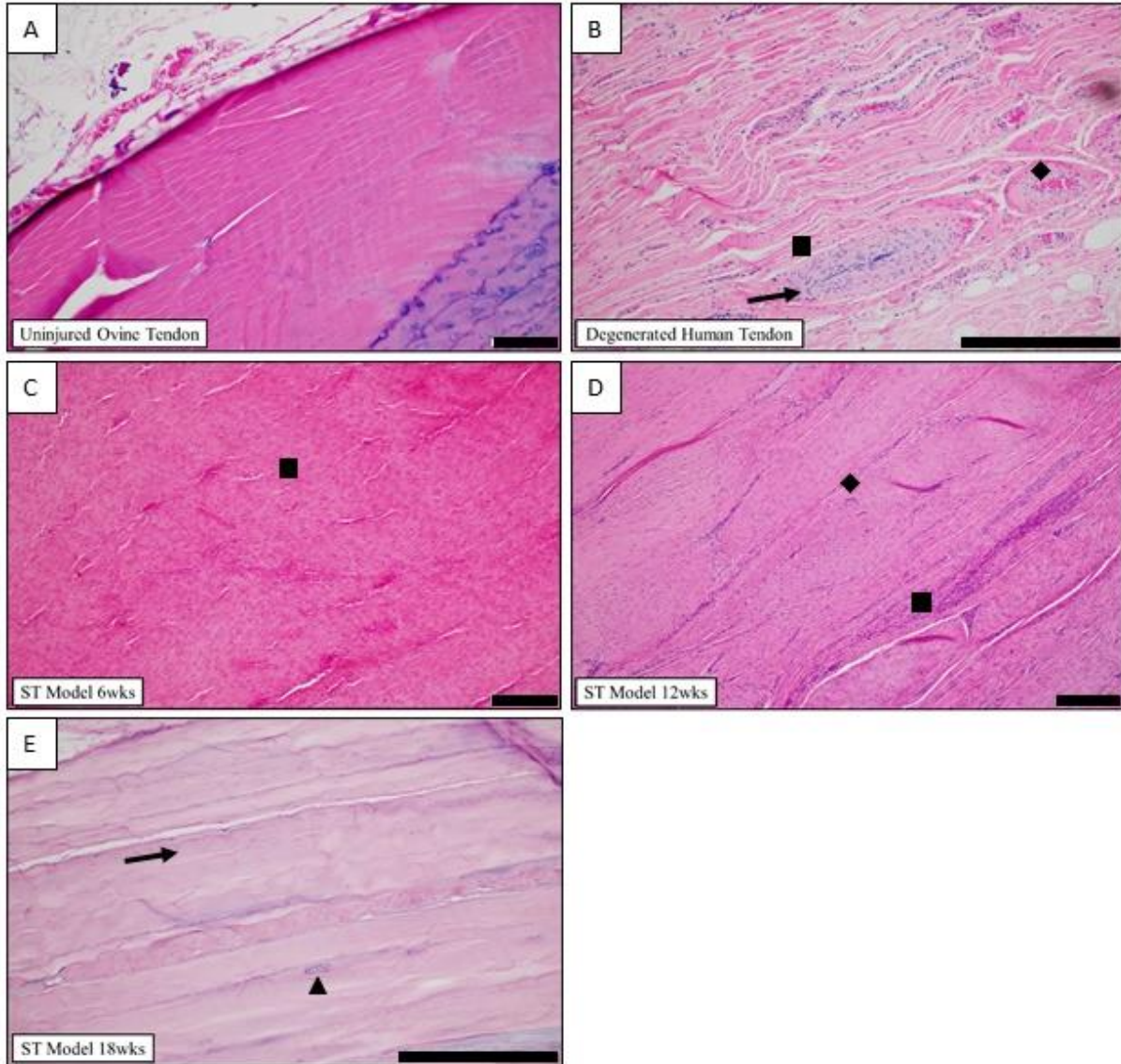
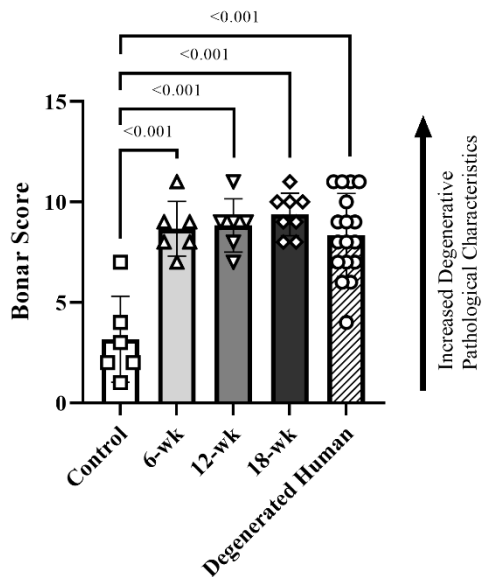


Figure 10. For each image, the black scale bars on the bottom right corner of the image are 500 μm. Representative micrographs of H&E-stained slides for all tendon groups. Marked increase of tenoblast population (square). Deposition of ground substance (arrow). Tenoblast lacunae (triangle). Increased vascularization (diamond).

Histopathology Results

In contrast to the uninjured ovine samples (Figure 10A), the sharply transected ovine tendons (Figure 10B, C, and D) exemplified pathological degeneration characteristics of human tendinopathy (Figure 10E). There was marked disruption of the superficial tendon abutting or adjacent to the enthesis in this ovine model. These changes in the ovine model were further characterized by loss of lamellar bundle organization, marked expansion of tenoblast (a.k.a., immature tenocyte) populations (Figure 10, square), and deposition of ground substance (Figure 10, arrow) which all contribute to the expansion of the tendon thickness. Tenoblasts rarely form lacunae (Figure 10, triangle) suggestive of early chondroid metaplasia. Arising from the superficial, adjacent humeral head and overlying this area of the tendon was a variably thick band of dense granulation tissue with prominent angiogenesis that extended into the tendon body. At times capillary clusters were prominent throughout the tendon body but were always most dense within the area of injury and the overlying granulation tissue (Figure 10, diamond). There is variable enthesophyte formation at the superficial enthesis.

Semi-Quantitative Pathological Scoring



Collagen Organization

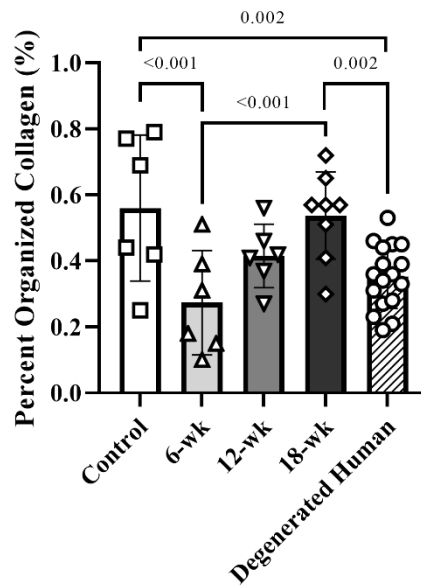


Figure 11. (Left) Overall Bonar degeneration score calculated by summing semi-quantitative scoring in the following categories: tenocytes, ground substance, collagen, and vascularity. (Right) Area of organized collagen normalized to total region analyzed as measured with polarized light microscopy and Picro-Sirius red staining. P-values are indicated for all pairwise comparisons which met the significance threshold ($P < 0.05$).

Biopsies of human supraspinatus tendon body were comprised of dense connective tissue demonstrating similar histologic features to the ovine sharp transection model adjacent to the site of injury. There was severe loss of lamellar collagen bundle organization and expansion of tenoblast populations (Figure 10, square) with rare lacunae formation, increased numbers of capillary profiles (Figure 10, diamond) and moderate amounts of ground substance (Figure 10, arrow) separating collagen bundles.

Results of the semi-quantitative Bonar scoring for tendon degeneration characteristics are summarized in Figure 11. At all timepoints the ST ovine model and the degenerated human samples scored significantly higher than uninjured ovine samples (8.67 ($P<.01$), 8.83 ($P<.01$), and 9.38 ($P<.01$), for the 6, 12, and 18-week timepoints, respectively).

Histomorphological assessment of collagen fiber alignment

The surgical disruption of the enthesis resulted in marked disorganization of collagen fibers throughout tendon in the ST model. Analysis of the amount of organized collagen fibers revealed marked decrease in organization in both the human and ST tendon samples (Figure 11), with reductions (as compared to the uninjured ovine group) of 51.0% ($P=.001$), 25.7% ($P=.071$), 4.4% ($P=.738$), and 37.1% ($P=.002$) for the 6-week ST, 12-week ST, 18-week ST, and degenerated human groups, respectively.

RNA sequencing

To investigate the gene expression profile changes related to the ovine tendon injury cascade, RNA sequencing was performed on two or three tendon biopsies per time point (12-week $n=3$, 16-week $n=3$, 18-week $n=2$). RNA-seq revealed gene expression patterns consistent with tendon degeneration over the entire 18-week observation period. Analysis of the resultant principal component analysis (PCA) plot, which depicts the differences in the 17,230 transcripts found using spatial positioning; the 12-week samples appear to be the most divergent from the control group

(uninjured ovine) (Figure 12A). Specifically, the significantly upregulated genes increased from 164 at 6 weeks post-surgery (Figure 12B), to 226 at 12 weeks (Figure 12C), and vastly increase again to 937 at 18 weeks (Figure 12D).

Gene Ontology of Biological Processes (GO BP) was assessed to document gene set enrichment that may be used for comparison in future studies. RNA gene counts were tabulated, grouped by time point and run in GSEA (gene set enrichment analysis software version 4.1.0) using the GO_BP gene set (version 7.2). Each time point was challenged with the uninjured group individually (i.e., 6-week ST vs. uninjured) and as a pooled “injured” group (i.e., all ST samples vs. uninjured). The top 30 normalized enrichment scores with false discovery rates less than 5% (FDR- $q < 0.05$) were selected from each data set for graphical analysis (Figure 13). Gene sets were grouped by shared biological process ontology categories (Mouse Genome Informatics (MGI), RRID:SCR_006460).

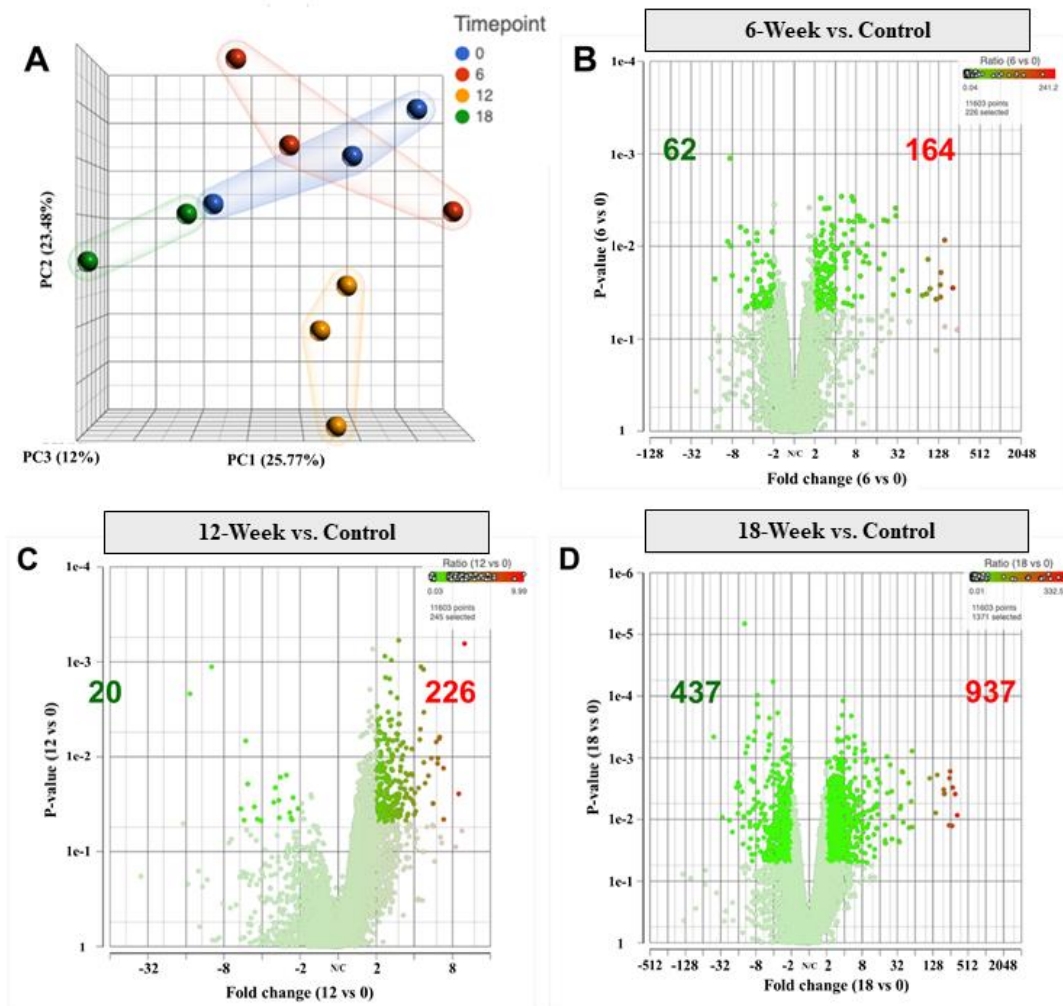


Figure 12. Gene expression changes in Tendon following sharp transection. (A) PCA plot illustrating the gene expression variance between the different timepoints of the Sharp Transection model and uninjured. Same time points grouped according to color (legend shown in top right corner). (B) Volcano plot comparing 12-week gene expression count to uninjured. X axis shows fold change y axis shows p value. Significant genes with p value <0.05 and fold change >2 or <-2 shown in bright red and green gradient with ratio scale on top right. At the six-week timepoint, there were 164 significantly upregulated genes and 62 significantly downregulated genes. (C) Volcano plot comparing 16-week gene expression count to uninjured. 225 significantly upregulated genes and 20 significantly downregulated genes. (D) Volcano plot comparing 18-week gene expression count to uninjured. 937 significantly upregulated, 437 significantly downregulated.

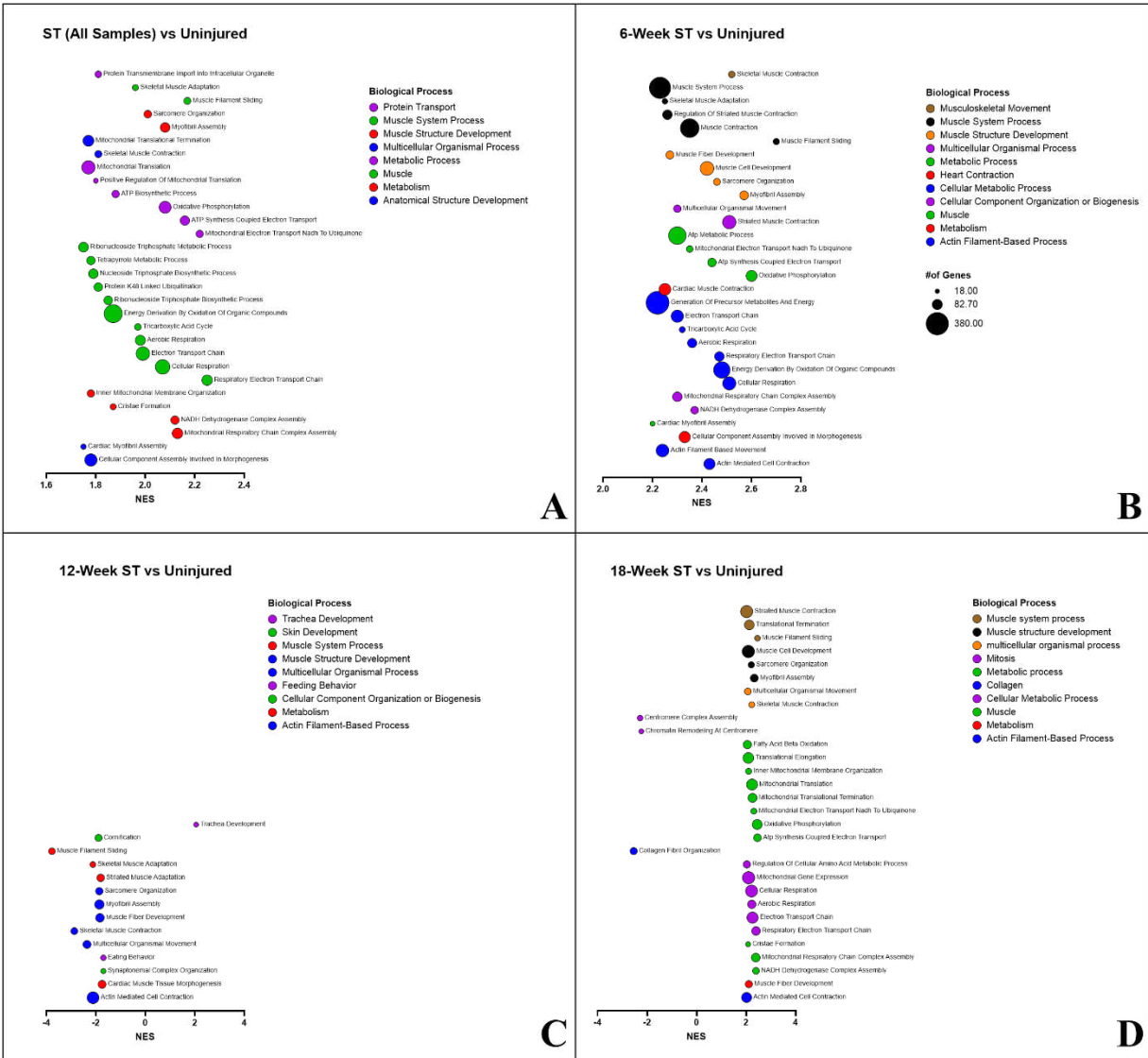


Figure 13. GSEA analysis of gene expression changes following sharp transection. Bubble plot illustrating results of GSEA using the GO BP gene set. The top 30 gene sets by normalized enrichment score (NES) (FDR-q<0.05 and NOM-p<0.01) of the following analyses are shown: all ST vs. uninjured (A), 6-week ST vs. uninjured (B), 12-week ST vs. uninjured (C), and 18-week ST vs. uninjured (D). Bubble colors correspond to biological process category, bubble size according to gene count, and bubble location according to NES.

Correlation Analysis

Significant correlations were observed between gene expression, mechanical testing, and pathologic scoring data. To compare the RNA-seq results to the mechanical testing and tendon pathology, 172 genes were selected for changes in expression levels present throughout the 18-week timepoints (Table 4). Temporal gene expression levels in RPKM (reads per kilobase transcript) were compared to Bonar score, collagen organization, CSA, maximum stress, and percent relaxation. There were significant gene expression correlation results (22 genes) found with collagen organization, percent relaxation, and Bonar scoring as shown in *Table 2*, all of which are protein coding genes. Several of the gene correlations with Bonar score had Pearson coefficients with magnitudes greater than 0.7: TRIM11 ($\rho=.774$, $P=.01$), PCDHGA1 ($\rho= -.772$, $P=.01$), and THAP1 ($\rho=.724$, $P=.01$), indicating that the RNA sequencing was able to illuminate some of the underlying cellular pathways associated with tendinopathy.

The mechanical properties were also compared to the pathologic criteria. The Bonar score was found to be strongly and significantly correlated with the peak stress ($\lambda=1.08$) of the tendons ($\rho= -.72$, $P<.01$, Figure 14), percent relaxation ($\lambda=1.08$, $\rho=.49$, $P=.01$), and CSA of the tendons ($\rho=.51$, $P<.01$). The peak stress was strongly and significantly correlated with the CSA of the tendons ($\lambda=1.06$: $\rho= -.68$, $P<.01$; $\lambda=1.08$: $\rho= -.76$, $P<.01$; Figure 14) and the ratio of organized collagen at both stretch magnitudes ($\lambda=1.06$: $\rho= .48$, $P=.01$; $\lambda=1.08$: $\rho= .42$, $P=.03$).

Table 4. Correlation of changes in gene expression with mechanical testing results and pathological characteristics. 172 genes were selected from 6-, 12-, and 18-week time points compared to uninjured control, based on a fold change of >2 or <-2. For n=11 sheep, gene expression in RPKM was compared to numerical values of mechanical scoring. Significant values were filtered out based on $p < 0.05$ in correlation analysis. This table shows list of genes with high correlation to mechanical testing categories in collagen organization, percent relaxation, and Bonar degeneration score.

	Gene ID	ρ	<i>P</i>-value
Col. Org. (%)	LRRC25	-0.664	0.03
Percent Relaxation (%) ($\lambda=1.08$)	ANKRD34A	0.662	0.03
	SSUH2	0.646	0.03
	FGB	0.684	0.02
Bonar Score	TRIM11	0.774	0.01
	THAP1	0.724	0.01
	SLC16A10	0.692	0.02
	PAQR8	0.682	0.02
	CAPN15	0.680	0.02
	URM1	0.680	0.02
	COMMD4	0.671	0.02
	DOK2	0.667	0.03
	RHOF	0.663	0.03
	NUP210	0.655	0.03
	CD274	0.650	0.03
	MAP4K1	0.632	0.04
	IL18R1	0.630	0.04
	CYTIP	0.626	0.04
	SLC6A17	-0.615	0.04
	FGFR3	-0.632	0.04
	PKDREJ	-0.684	0.02
PCDHGA1	-0.772	0.01	

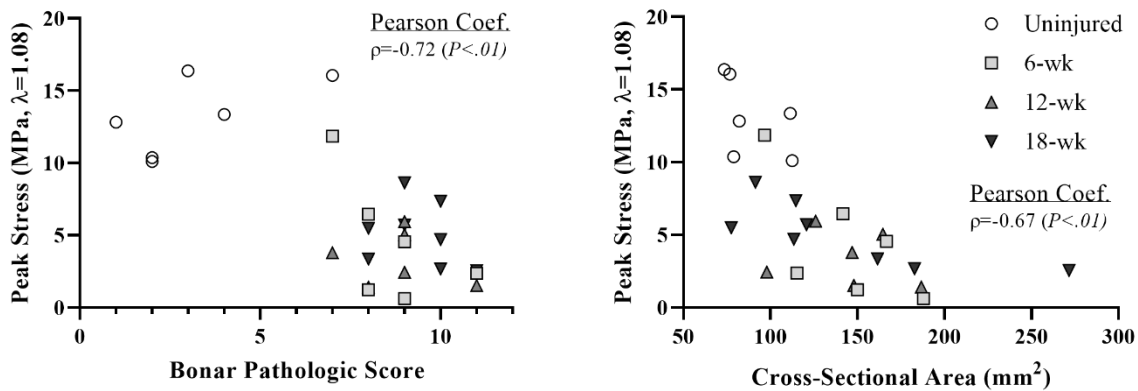


Figure 14. (Left) Scatterplot illustrating the relationship between the non-destructive biomechanical response of the tendons as related to the pathologic degeneration scoring. Peak stress was markedly and significantly decreased in samples that evidenced increased pathologic characteristics ($\rho= -.72$, $P<.01$). (Right) Scatterplot illustrating the relationship between the non-destructive biomechanical response of the tendons and their respective cross-sectional areas. Peak stress was markedly and significantly decreased in samples with increased CSA ($\rho= -.67$, $P<.01$).

Conclusions

Several ovine models have been attempted in an effort to emulate the degenerative changes seen in humans clinically^(92,106,110). Unfortunately, these models have led to degenerative changes that did not fully match the severity or form of what has been noted in humans. In contrast to the previous models, this new model of controlled entheses injury was able to produce similar levels of tenocyte reactivity, angiogenesis, collagen organization, and ground substance deposition that were hallmarks of the degenerated human sample group. These changes were measured through both the histomorphometric quantification of organized collagen and the semiquantitative pathologic scoring. This model has also demonstrated inferior mechanical properties, thus highlighting the multimodal manifestation of degenerative-like changes. These changes were still

witnessed at the latest timepoint, 18-weeks. This suggests that the changes occurring in these tendons are long-term and lead to a similar cascade of changes that are used to describe chronic degeneration of human RCT.

These data presented above highlight the deteriorations in mechanical performance of the ST tendons at all timepoints, as illustrated by both peak stress and percent relaxation. Multiple groups have performed destructive testing on ovine infraspinatus tendons and reported decreases in ultimate load between 2,754.3 N (78.3%)⁽³⁾ and 3,301.2 N (78.4%)⁽⁶⁵⁾ for acutely repaired tendons as compared to intact tendons. Similar results have been reported in a canine repair model; Derwin et al. reported a reduction in ultimate force of 927 N (58.1%)⁽⁷⁰⁾. Unfortunately, direct comparisons between destructive and non-destructive biomechanical testing are not valid, the results of these studies lend credence to our data indicating decreased mechanical performance associated with injury and deterioration. Furthermore, Derwin et al. reported between 84% and 303% increase in CSA of the canine tendons at 6 and 12-weeks, respectively. This increase in CSA which was noted at all timepoints in the ST tendons.

Histopathologic changes for this ST model demonstrate similar pathology to what was previously described in people^(111,126-128). Translatable changes include those defined in the semi-quantitative Bonar scoring (Figure 11). Collagen disruption was marked, with mild cartilaginous to rarely osseous metaplasia. There was also moderate deposition of ground substance with rare scattered mononuclear infiltrates. Angiogenesis was marked with highest density within the surgical site

and extension into the adjacent tendon with increased vessel prominence throughout the tendon body. Similar to previous ovine models of tendon injury, while damage was isolated to a portion of the enthesis, pathologic changes were noted throughout the tendon body, extending distal towards the muscle belly⁽⁹¹⁾.

Upon analyzing the relationship between the data collected at both the macroscopic and microscopic levels, it can be seen that the cellular activity and microstructure significantly impact the tendon mechanics. These data reveal a strong, significant relationship between the peak stress and the Bonar pathologic score ($\rho=-0.72$, Figure 14). As collagen is the primary load-carrying component of tendons, it is evident that pathologic scoring criteria that assess collagen organization and degeneration could predict the mechanical performance of the tendons to some degree. The relationship between tendon microstructure and mechanical competence is further bolstered by the strong, significant correlation between peak stress and the CSA of the tendons ($\rho=-0.67$, Figure 14). These data highlight the relationship between length-scales of the tendon – with the cell-level changes driving the ultimate functionality of the tendon.

Gene expression patterns in these tendons were changed similarly to what has been documented in literature regarding injured human rotator cuff tendons. Jelinsky et al. [dataset]⁽¹²⁹⁾ measured global gene expression patterns in diseased human tendons obtained intraoperatively; however, the main findings included Flexor-Pronator, supraspinatus and extensor carpi radialis brevis tendons, whereas the present study was controlled to a single tendon type (Accession number

GSE26051). At the 12-week timepoint, the ovine tendons exhibited similar expression patterns of collagen genes compared to the human study in 21 out of the 26 collagen genes that were regulated in our study. Interestingly, this similarity dissipated at the 18-week timepoint, with only 7 out of the 26 genes matching expression patterns. Upon comparison of the lesioned supraspinatus tendon vs. the non-lesioned subscapularis tendon data from Jelinsky et al. using the GEO2R tool, (Gene Expression Omnibus (GEO), RRID:SCR_005012), out of 2,642 significant DEGs, there was a 66.7% match of gene expression pattern in our 12-week ST ovine samples (both up- or down-regulated in sheep and human datasets). This change in expression pattern between the ovine model timepoints highlights the temporal nature of tendon injury, degeneration, and healing phases. Less is known regarding the gene expression patterns of chronic tendon damage over long periods of time in humans. Ireland et al⁽¹³⁰⁾ using RT-PCR showed that late stage degenerated Achilles tendons in humans have increased expression of type III and type I collagen, tenascin, which matches the magnitude of changes we observed in our ST model at 12-weeks. An additional study by Ireland et al⁽¹³¹⁾ showed upregulation of MMP-2, FN1 (ITGB1), VEGF, MAPK in chronic Achilles tendinosis, which was also seen in similar magnitudes in the 12-week ST samples. These similarities help to strengthen our conjecture that this ST model is an appropriate translational model of human tendinopathy. Specifically, it appears that the 12-week timepoint most closely matches the gene expression pattern that has been documented in human cases of tendinopathy, thus suggesting it may be the most appropriate timepoint at which to analyze and study chronic tendon degeneration.

This study has several limitations that should be considered when interpreting the results. Most previous studies have relied on destructive biomechanical testing to benchmark the properties of injured and repaired tendons, with the general idea that improved ultimate force or stress would be correlated with improved surgical outcomes. While this reasoning is sound, destructive testing precludes the ability to perform subsequent histological analysis on the samples. This study utilized non-destructive stress relaxation testing to tease out differences in tendon mechanical properties, while still enabling subsequent histological analysis – enabling direct correlation between the mechanical properties, pathologic characteristics, and gene expression levels of the tendons at various timepoints. Unfortunately, non-destructive viscoelastic properties of degenerated human tendons have not yet been studied, rendering a comparison of changes between this model and what happens in humans intractable. A further limitation of this research is that the histological sections were scored semi-quantitatively. Although an established grading scheme was followed, exact amounts or levels of features of interest such as cellularity were not calculated. Ongoing work entails examining the non-destructive viscoelastic properties of degenerated and healthy cadaveric human tendons, followed by subsequent histopathologic, histomorphometric, and gene expression analysis – providing researchers new understanding of the relationships between macrostructural properties and the underlying microstructural arrangement and cellular activity in human samples. By better exploring the connections between the biophysical and biochemical length-scales, researchers will be enabled to better understand and develop biological therapies that will ultimately improve the prognosis of tendon repair surgeries.

This new translational model of enthesis damage is a vital step towards improving the understanding of the pathogenesis of chronic rotator cuff degeneration, laying the framework for better understanding the impact of future biologics and therapies aimed at improving tendon repair surgeries. Arguably this reproducible model is the most accurate large animal model capable of reproducing pathologic changes similar to those witnessed in the human rotator cuff degenerative cascade. This model is especially powerful considering the similarities in size, structure, and healing capacity between sheep and humans, thus providing an effective platform with which to test new therapies and treatments for this condition. However, it is worth noting that this model fundamentally was designed to replicate degenerative changes that occur secondary to enthesis trauma. Therefore, there still is a necessity for future work to investigate the impact of mid-substance damage and to compare the way in which these two types of damage manifest in the tendon degeneration cascade.

This novel translational ovine model shows similar changes in tenocyte reactivity, angiogenesis, collagen organization, and ground substance deposition to what is seen in humans with chronic rotator cuff degeneration. Furthermore, this model was able to produce gene expression pattern changes that are similar to those documented in humans, thus lending to the accuracy and translatability of this model. Specifically, the 12-week timepoint appears to most accurately embody the characteristics of chronic tendon degeneration seen clinically. This model has the potential to improve the understanding of the underlying pathways that lead to the degenerative state seen in humans, thus providing researchers a valuable platform in which to research new treatments and therapies.

Chapter 4- Tendon Midsubstance Trauma as a Means for the Development of Translatable Chronic Rotator Cuff Degeneration in an Ovine Model³

Background

Rotator cuff tear (RCT) incidence is prominent, with some cadaver studies finding that roughly 30% of the population have tears to these tendons. Injuries to the rotator cuff decrease quality of life, with patients experiencing significant pain and decreased mobility of the arm. Unfortunately, failure rates of RCT repair surgeries are unacceptably high, with reported failure rates reaching 94% depending on exacerbating risk factors⁽¹⁴⁻¹⁷⁾ such as chronic degeneration. Specifically, chronic degeneration of the rotator cuff tendons describes a state of diminished tissue quality which subsequently increases rate of injury and hampers the surgical repairs^(11,13).

Chronic degeneration, also known as tendinopathy, is a pathologic condition which describes changes to the tendon including increased cellularity, hypervascularization, surplus proteoglycan content, and decreased collagen organization^(36,38,39,111,132,133). Tendinopathy originates from a combination of extrinsic and intrinsic factors, such as overuse⁽¹³⁴⁾, impingement⁽¹³⁵⁾, aging⁽³⁵⁾, changes in biology⁽¹³²⁾, and reduced mechanical properties⁽¹³²⁾. As mentioned previously, chronic degeneration is a complicating risk factor to RCT repairs. Therefore, an interventional therapy that could reverse the cascade of chronic rotator cuff tendon pathology prior to injury would

³ Johnson J, v. S. D., Regan D, Easley J, and D. S. Chow L, Romeo T, Schlegel T, McGilvray K (2021). "Tendon midsubstance trauma as a means for the development of translatable chronic rotator cuff degeneration in an ovine model." *Ann Translation Medicine*.

revolutionize the treatment of rotator cuff injuries. Unfortunately, such a therapy has yet to be developed.

Preclinical animal testing is a vital step in the development and validation of therapies. Current animal models of chronic rotator cuff degeneration almost exclusively utilize enthesis trauma as a means to induce pathology that replicates the hallmarks of chronic degeneration (3,68,70,83,91,92,106,109). Previous large-animal models have been implemented through a variety of surgical insults, ranging from complete transection with delayed repair⁽⁹²⁾, partial transection with delayed repair⁽⁹¹⁾, and partial transection of the enthesis⁽¹³⁶⁾. Early models (i.e., full or partial transection with delayed repairs) produced tendon tissue with severe and reactive pathology beyond what has been noted clinically, while also generating severe tendon retraction that precludes repair. While these models play a vital role in testing devices intended at improving repair integrity, the presence of trauma at the enthesis is not representative of a chronically degenerated tendon pre-tear (i.e., older patients with a history of overuse without tendon tears). It is well known that reestablishment of the native fibrocartilaginous insertion is not currently possible⁽¹³⁷⁾; with tendon mechanics permanently altered following enthesis disruption. With this in mind, it is evident that these tear models do not lend themselves to the testing of therapies intended at restoring the midsubstance environment of a healthy tendon.

Therefore, the goal of this work was to generate and characterize a model of chronic tendon degeneration that does not originate from direct enthesis damage. Furthermore, the magnitude and

manifestations of the histopathological and gene expression changes exhibited by this model at multiple timepoints were to be compared to a positive control (i.e., degenerated human rotator cuff tendon tissue) in order to validate and prove translatability of this model. We hypothesized that surgical micro-trauma to the mid-tendon body without direct enthesis trauma would induce pathologic changes that accurately emulate the chronic degenerative condition seen in humans, as measured by exhaustive mechanical, pathological, structural, and gene expression analyses. We present the following article in accordance with the ARRIVE and MDAR reporting checklists.

Methods

The study was conducted in accordance with the Declaration of Helsinki (as revised in 2013). The study was approved by institutional ethics board of the Rush Medical University (No.: 16110707-IRB01) and informed consent was taken from all the patients. Animal experiments were performed under a project license (NO.: 18-7854A) granted by institutional committee board of Colorado State University, in compliance with United States national or institutional guidelines for the care and use of animals.

Ovine Models – Surgical Procedure

Bilateral surgical insults were completed on the infraspinatus tendons in twenty *Ovis aries* ewes (≥ 3.5 years of age) generating forty treated shoulders. Rams were excluded from this study as a result of animal husbandry concerns. The surgical models were alternated between shoulders to

eliminate the potential of a left/right side bias and are detailed as follows: (1) sharp partial transection of the entheses (n=20 treated tendons – data published previously ⁽¹³⁶⁾) and (2) combed fenestration of the enthesis and tendon mid-substance (n=20 treated tendons)).

The surgical procedure has been detailed previously ⁽¹³⁶⁾. The surgical midsubstance trauma model, a.k.a., “combed fenestration” (CF), was generated by creating 16 longitudinal cuts within the top third of the infraspinatus tendon thickness (Figure 15). This insult was chosen to simulate micro-trauma of the tendon that did not result in separation of the tendon from the humerus, with the objective to replicate what is hypothesized to occur in humans with chronic degeneration prior to tendon tears. The underlying reasoning for this surgical insult was that by inducing micro-trauma on the tendon, the strain profile within the tendon would be altered, leading to similar degenerative changes that have been documented in humans clinically. Additionally, the creation of micro-trauma causing separation of the tendon collagen, extra-cellular matrix, and vasculature, would lead to a wound healing cascade, impacting tendon quality and function. Upon completion of model generation, standard surgical closure procedures were followed. The ewes were permitted to ambulate and eat *ad libitum* for the duration of the study. On a daily basis, sheep were monitored for all signs of complications and to evaluate incisional site healing, lameness/ambulatory function, and pain.

Sheep were sacrificed humanely at 6-, 12-, and 18-weeks to acquire the temporal tissue response to injury and subsequent degeneration. Immediately following sacrifice (<20 min.), the humerus-

infraspinatus tendon constructs (HTCs) were harvested and subsequently isolated and denuded of soft tissues, ensuring no damage was imparted on the infraspinatus tendon. As detailed previously⁽¹³⁶⁾, a small portion (5mm x 20mm) of tendon was snap frozen for the purpose of RNA sequencing.

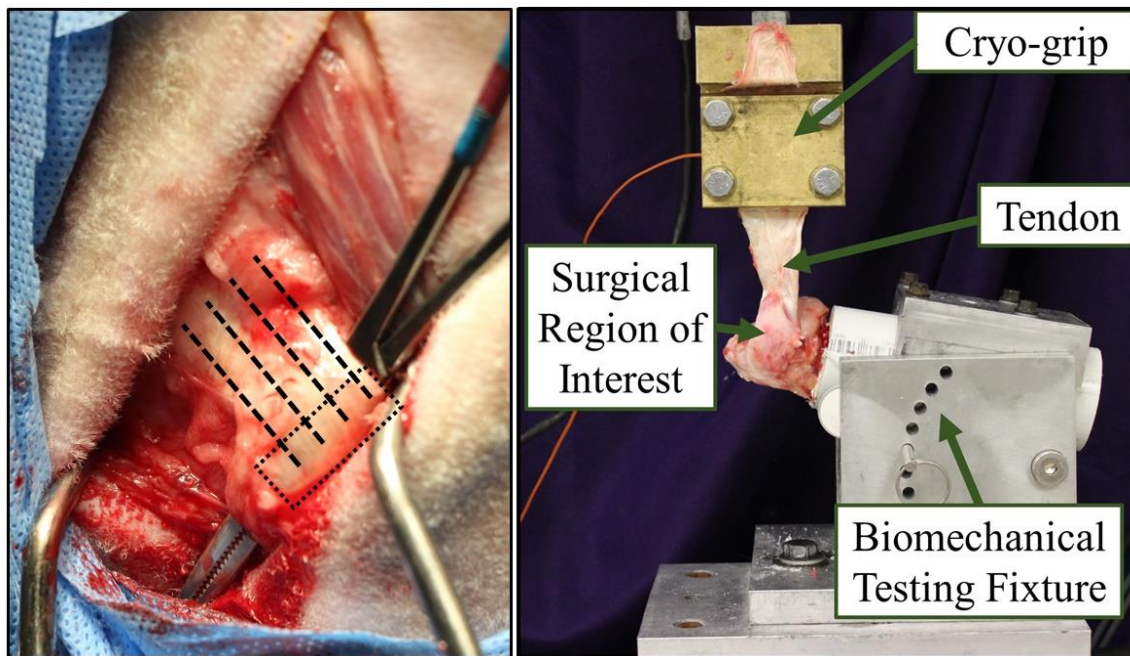


Figure 15. Photos illustrating model generation and biomechanical testing. (Left) Intra-operative image depicting the location and direction of microtrauma on the ovine infraspinatus tendon. Square box indicated the enthesis. Dotted lines represent location and direction of the combed fenestrations (only 4 of the 16 cuts are illustrated). (Right) Image of biomechanical testing (image from previously published article “Enthesis trauma as a means for the development of translatable chronic rotator cuff degeneration in an ovine model” [Figure source: <http://dx.doi.org/10.21037/atm-21-354>; use permitted under the Creative Commons Attribution License the CC BY-NC-ND 4.0].

Biomechanical Testing

HTCs were tested non-destructively to determine their viscoelastic material properties as previously described ⁽¹³⁶⁾. These properties were assessed as a means to benchmark the altered biomechanical properties of the tendon tissue at multiple timepoints, such that the effectiveness of future therapies could be assessed against these values. Tendon cross-sectional area (CSA) measurements were taken in triplicate proximal to the insertion ^(68,71,115,116). To ensure the highest level of stress in each tendon was reported, force was transformed to stress using the minimum of the three CSA measurements. The mean of the three CSA measurements was taken to determine the tendon overall CSA. Subsequently, the humeri were affixed in polyvinyl chloride (PVC) sleeves using a strong two-part hard casting resin (SmoothCast 321, Smooth-On, Macungie, PA). PVC sleeves were gripped in a custom fixture attached to a servo-hydraulic load frame (Model 858, MTS Corp., Eden Prairie, MN), enabling anatomically accurate loading of the tendon (Figure 15) ^(3,71). Tendons underwent a pre-loading phase (5N static force, 2 minutes duration) prior to biomechanical testing to normalize viscoelastic effects ^(68,117-121). Following the pre-loading phase, gage length of the tendon was measured, allowing transformation of the displacement (mm) data into stretch (mm/mm). Non-destructive stress relaxation testing was then performed on each sample, wherein a physiologically relevant stretch (i.e., 1.06 and 1.08) was applied for a duration of 100 seconds ^(120,122). Outcome parameters included peak stress (MPa), peak force (N), and percent relaxation (%) ⁽¹²³⁾. To allow samples to come to viscoelastic equilibrium ⁽¹²⁰⁾, tendons were subjected to a 1,000 second recovery period between tests. Physiological saline spray was used to ensure adequate tendon hydration throughout the entire preparation and biomechanical testing processes.

Histological Analysis

To determine microstructural and cellular characteristics of the tendons, samples underwent histological processing following biomechanical testing as previously described ⁽¹³⁶⁾. Upon completion of biomechanical testing, specimens were fixed in 10% neutral buffered formalin, decalcified in 8% trifluoroacetic acid⁽¹³⁸⁾, and subsequently processed using standard paraffin embedding techniques. Two 5 µm thick slides were produced from each specimen, with one slide allocated to hematoxylin and eosin (H&E) staining and the other Picro-Sirius red staining.

A blinded veterinary pathologist in residency utilized the Bonar tendinopathy scale to assess H&E slides for: (1) tenocyte reactivity, (2) angiogenesis, (3) tendon bundle organization and polarization, and (4) deposition of ground substance⁽⁴⁰⁾. All categories were graded on a 4-point scale ranging from 0 (normal/healthy) to 3 (markedly “degenerated” / pathologic) ⁽⁴⁰⁾. The summation of these scores was used to generate an overall degeneration score ranging from 0 (normal) to 12 (degenerated) for each specimen. These scores were assessed to enable comparison of the tendon tissue generated in this model to the positive control of chronically degenerated human tendon tissue.

Histomorphological assessment of collagen fiber alignment and intramuscular adipose content

To quantify the degree of collagen organization within the tendons, histomorphological analyses were performed as described previously ⁽¹³⁶⁾. Briefly, polarized light microscopy in conjunction with Picro-Sirius red stained slides were assessed for collagen fiber organization, as a means to quantify the microstructural changes within the tendon collagen and to compare against the positive control of chronically degenerated human tendon tissue. The percent area of organized collagen seen within the region of interest (25mm of tendon adjacent to insertion) was quantified using commercially available software (Image-Pro Plus, RRID:SCR_007369).

Intramuscular adipose content was also quantified through histomorphometry analysis as a means to quantify the temporal changes of fatty atrophy. Muscle biopsies from the center of the infraspinatus muscle belly were taken during dissection. Samples were fixed in 10% neutral buffered formalin and processed using standard paraffin embedding techniques. Slides were stained with hematoxylin and eosin and imaged at 40x using standard optical microscopy. The area of adipose tissue and total tissue area (excluding adipose area) were quantified (Image-Pro Plus, RRID:SCR_007369). To account for differences in histological artifacts, the adipose area was normalized to the total area (i.e., the sum of the adipose area and the tissue area) providing percent adipose area. To remove area selection bias, this value was calculated at three randomly chosen uniformly sized regions across each sample. The mean of these three values was taken yielding one value representing the average percent adipose tissue area for each sample.

Segmentation images were reviewed by a veterinary pathologist in residency to ensure accuracy and consistency across all samples.

RNA sequencing

To determine the gene expression changes secondary to tendon injury and enable comparison to those documented in human samples previously, RNA sequencing was performed on the tendons as outlined previously ⁽¹³⁶⁾. During fine dissection, tendon biopsies were taken and flash frozen in liquid nitrogen to prevent RNA degradation. Biopsies were pulverized then lysed (TRizol™ Invitrogen, Carlsbad, CA) to precipitate RNA. The chloroform method ⁽¹²⁴⁾ was used to isolate the RNA, with increased incubation time to account for the size of the tissue. Commercially available kits (RNeasy, Qiagen, Hilden, Germany) were then used to purify extracted RNA.

The RNA sequencing details have been described in our previous manuscript reporting the other half of this study⁽¹³⁶⁾. Differentially expressed genes were calculated for each timepoint compared to uninjured samples (data from previous work⁽¹³⁶⁾) using Partek GSA (gene specific analysis) and non-parametric ANOVA.

Statistical analysis

Comparisons across timepoints and treatments were carried out using a one-way ANOVA followed by Fisher's *post-hoc* test (Minitab, RRID:SCR_014483) ($\alpha=0.05$). All data passed Anderson-Darling normality test (peak force, peak stress, percent relaxation, cross-sectional area, Bonar score, percent organized collagen, and intramuscular adipose content). A Box Cox transformation was implemented for data that failed the Levene test for equal variance (Peak Force, $\lambda=1.06$). Utilizing results from pilot animals, sample sizes were selected to achieve 80% statistical power. Sample numbers in each grouping were: n=6 shoulders at the 6 and 12-week timepoints, and n=7 shoulders at the 18-week timepoint. Uninjured ovine data from our previous publication⁽¹³⁶⁾ was used as a negative control for all data sets, such that changes to the tendon tissue as a result of the model could be assessed. Human samples of chronically degenerated tendons from previous work⁽¹³⁶⁾ were used as positive control for histopathological and histomorphological comparisons, such that this model could be adequately validated and translatability could be verified. Pearson correlation coefficients were generated as a result of correlation analyses between all outcome parameters. No specimens/samples were excluded from this study.

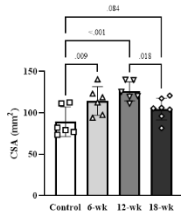
Results

No animals were lost during this study. No surgical complications or otherwise were noted in any animals.

Biomechanical Results

A marked increase in CSA was noted in the CF tendons at all three timepoints, with percent increases as compared to the uninjured group of 28.1% ($P=.009$), 41.6% ($P<.001$), and 16.9% ($P=.084$) at the 6, 12, and 18-week timepoints, respectively. Moreover, the CF treatment groups exhibited diminished biomechanical properties (Table 5). The CF tendon samples displayed marked, significant decreases in peak stress (Figure 16), with decreases of: 60.3% (6-wk, $\lambda=1.06$, $P=.002$), 55.3% (6-wk, $\lambda=1.08$, $P=.004$), 55.9% (12-wk, $\lambda=1.06$, $P=.005$), 55.3% (12-wk, $\lambda=1.08$, $P=.004$), 41.2% (18-wk, $\lambda=1.06$, $P=.025$), and 39.4% (18-wk, $\lambda=1.08$, $P=.026$). The viscoelastic properties of the CF tendons were also altered, as evidenced by increases in percent relaxation (as compared to uninjured) at both stretch magnitudes (Figure 16), with the CF tendons exhibiting relative decreases (as compared to uninjured) of: 55.2% (6-wk, $\lambda=1.06$, $P=.118$), 44.5% (6-wk, $\lambda=1.08$, $P=.134$), 18.7% (12-wk, $\lambda=1.06$, $P=.584$), 10.5% (12-wk, $\lambda=1.08$, $P=.712$), 81.7% (18-wk, $\lambda=1.06$, $P=.021$), and 75.6% (18-wk, $\lambda=1.08$, $P=.035$).

Tendon Cross Sectional Area



Stress Relaxation Testing

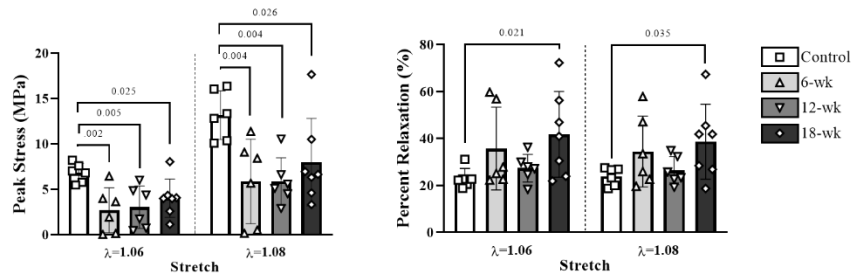


Figure 16. Biomechanical testing results. (Left) Cross-sectional area (CSA) measurements of tendon specimens. (Middle) Peak stress values from the stress-relaxation testing ($\lambda=1.06, 1.08$). (Right) Percent relaxation values from the stress-relaxation testing ($\lambda=1.06, 1.08$). P-values are

indicated for all pairwise comparisons which met the significance threshold ($P < 0.05$); individual data points are marked with symbols according to their respective groups (i.e., square (Control), triangle up (6-wk), triangle down (12-wk), diamond (18-wk)).

Table 5. Biomechanical and geometric properties for tendon samples.

Time point	Stretch	Percent Relaxation (%)		Peak Load (N)		Peak Stress (MPa)		Area (mm ²)	
			<i>P</i> value		<i>P</i> value		<i>P</i> value		<i>P</i> value
Control	$\lambda=1.06$	23.0% \pm 4.2%	-	582 \pm 111	-	6.8 \pm 1.0	-	89 \pm 18	-
	$\lambda=1.08$	23.8% \pm 3.8%	-	1108 \pm 176	-	13.2 \pm 2.7	-		
6 Weeks	$\lambda=1.06$	35.7% \pm 17.6%	0.118	292 \pm 285	0.031	2.7 \pm 2.5	0.002	114 \pm 17	0.009
	$\lambda=1.08$	34.4% \pm 15.1%	0.134	629 \pm 512	0.027	5.9 \pm 4.7	0.004		
12 Weeks	$\lambda=1.06$	27.3% \pm 5.9%	0.584	355 \pm 274	0.085	3.0 \pm 2.4	0.005	126 \pm 12	<0.001
	$\lambda=1.08$	26.3% \pm 6.0%	0.712	702 \pm 323	0.056	5.9 \pm 2.6	0.004		
18 Weeks	$\lambda=1.06$	41.8% \pm 18.3%	0.021	373 \pm 159	0.099	4.0 \pm 2.1	0.025	104 \pm 13	0.084
	$\lambda=1.08$	38.6% \pm 16.0%	0.035	718 \pm 304	0.057	8.0 \pm 4.8	0.026		

Data presented as mean \pm SD. P values indicate difference with uninjured control group at same stretch level (bold when $P < .05$).

Histology Results

At all timepoints in the CF samples, the superficial third of the tendon adjacent to the enthesis was mildly thickened and markedly disrupted by disorganized collagen with loss of lamellar bundle organization and increased vascular density with noteworthy expansion of immature tenocyte populations which occasionally formed lacunae (Figure 17). A band of dense granulation tissue with prominent angiogenesis was found overlying this area and extending from the associated humeral head . Capillary clusters were prominent and often dense within the area of injury and the overlying granulation tissue (Figure 17). Enthesophyte formation of the superficial humeral head was variable.

Throughout the 6-, 12-, and 18-week timepoints there was a consistent trend toward organization of the granulation tissue overlying the injured tendon. The changes are characterized by decreased fibroblast density, smaller, less frequent blood vessels, and increased collagen disorganization with decreased tinctorial intensity. These features are consistent with a transition toward scar tissue with indistinct borders to the underlying, pre-existent tendon. Throughout the superficial tendon body in the area of injury there was a mild decrease in tendon fibroblast density over time.

The CF samples exhibited markedly increased pathologic characteristics as measured by semiquantitative Bonar scoring (Figure 18). Specifically, increases in the Bonar score were noted at all timepoints in the CF groups as compared to the uninjured group, with relative increases in

Bonar scores of 173.7% ($P < .001$), 136.8% ($P < .001$), and 152.6% ($P < .001$) for the 6, 12, and 18-week timepoints, respectively.

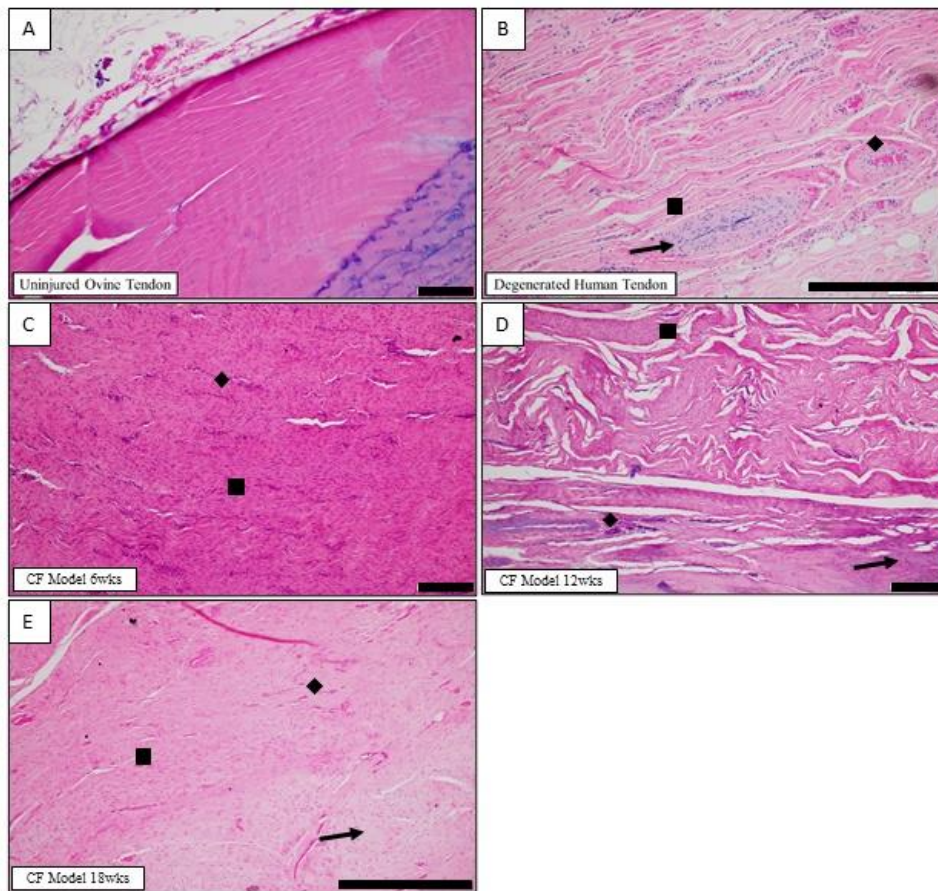


Figure 17. Representative sections of H&E-stained specimens for all treatment groups. 3A) Uninjured ovine tendon. 3B) Degenerated human tendon. 3C) Combed fenestration (CF) Model 6wks. 3D) CF Model 12wks. 3E) CF Model 18wks. Square indicates regions containing representative increases to tenoblast populations. Arrow indicates regions containing increased deposition of ground substance. Triangle indicates regions containing tenoblasts within lacunae. Diamond indicates representative regions with increased vascularization. For each image, the black scale bars on the bottom right corner of the image are 500 μm . Uninjured and human chronic degenerated group images included from previously published article “Enthesis trauma as a means for the development of translatable chronic rotator cuff degeneration in an ovine model” [Figure source: <http://dx.doi.org/10.21037/atm-21-354>; use permitted under the Creative Commons Attribution License the CC BY-NC-ND 4.0].

Histomorphology Results

Histomorphometry analysis of collagen organization revealed decreased organization in the CF samples at all timepoints (Figure 18), with relative decreases (as compared to uninjured group) of 22.9% ($P=.189$), 16.2% ($P=.343$), and 11.8% ($P=.506$) for the 6, 12, and 18-week groups, respectively. No significant differences were noted between the CF groups and the degenerated human samples. The CF samples at all timepoints demonstrated increased intramuscular adipose content as evidenced by increased percent adipose area, with relative increases in adipose area as compared to the uninjured ovine group of 56.4% ($P=.071$), 30.3% ($P=.315$), and 53.6% ($P=.077$) for the 6, 12, and 18-week groups, respectively.

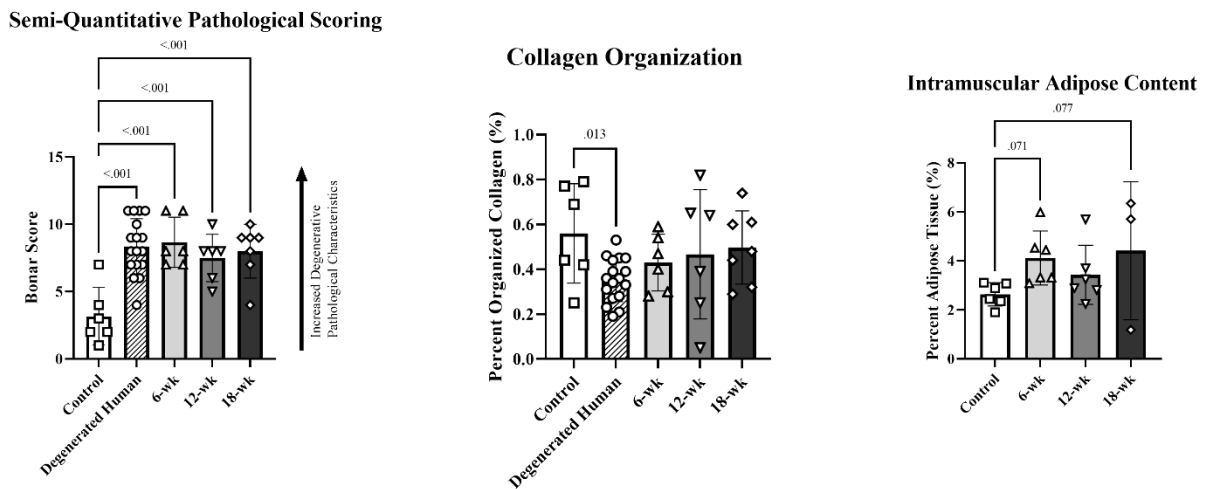


Figure 18. Pathological scoring and histomorphometry results. (Left) Overall Bonar degeneration score (Center) Percent organized collagen. (Right) Percent intramuscular adipose area. P-values are indicated for all pairwise comparisons which met the significance threshold ($P<0.05$); individual data points are marked with symbols according to their respective groups (i.e., square (Control), circle (Degenerated Human), triangle up (6-wk), triangle down (12-wk), diamond (18-wk)).

RNA sequencing

The number of samples that met quality control specifications and underwent RNA sequencing are as follows: 6-week n=4, 12-week n=0, and 18-week n=3. RNA-seq of tendon samples revealed gene expression patterns in line with tendon degeneration over the entire 18-week observation period. As evidenced by the principal component analysis plot, the gene expression patterns of the 18-week samples appear to be the most divergent from the control group (uninjured ovine) (Figure 19A). Specifically, the significantly up-regulated + down-regulated genes increased from 98 at 6 weeks post-surgery (Figure 19B) to 1,235 at 18 weeks (Figure 19C), yielding 185 across all CF samples (Figure 19D).

Gene Ontology of Biological Processes (GO BP) was evaluated to explore gene set enrichment as a means to provide a comparative baseline for future studies. Gene counts as determined via RNA-seq were tabulated and run in GSEA (version 4.1.0) using the GO_BP gene set (version 7.2). Time points were challenged individually against the uninjured group and as a pooled “injured” group (i.e., all CF samples vs. uninjured). Thirty pathways from each comparison with the highest normalized enrichment scores and false discovery rates less than 5% proceeded to graphical analysis (Figure 20). Gene sets were grouped by shared biological process ontology categories (Mouse Genome Informatics (MGI), RRID:SCR_006460).

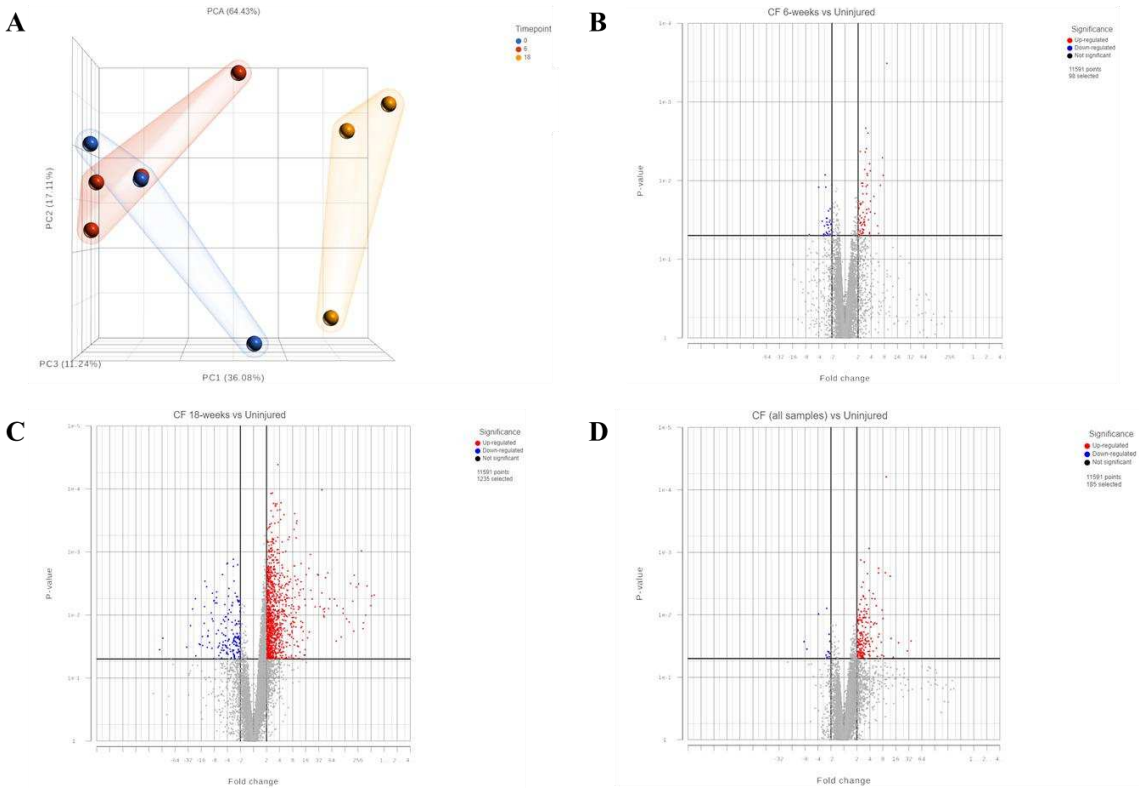


Figure 19. Gene expression changes in tendon following sharp transection. 5A) Principal component analysis (PCA) plot illuminating the temporal changes in gene expression in the Combed Fenestration (CF) model and uninjured. 5B) Volcano plot comparing 6-week gene expression count to uninjured. X axis shows fold change; y axis shows p value. Significant genes with p value <0.05 and fold change >2 or <-2 shown in bright red and green gradient with ratio scale on top right. At the six-week timepoint, there were 70 significantly up-regulated genes and 28 significantly down-regulated genes. 5C) Volcano plot comparing 18-week gene expression count to uninjured. 1,063 significantly up-regulated genes and 172 significantly down-regulated genes. 5D) Volcano plot comparing gene expression of all CF samples count to uninjured. 172 significantly up-regulated, 13 significantly down-regulated.

Correlation Analysis

An exploratory correlation analysis was performed to probe potential gene roles in other outcome parameters from the mechanical testing and pathologic scoring. To determine appropriate gene candidates, a list of genes was selected from the CF samples (both timepoints) vs uninjured control, based on an absolute value of fold change greater than 2, leading to a potential list of 300 genes. For n=10 sheep, gene expression (i.e., RPKM) was compared to biomechanical and histopathological properties (i.e., peak stress, percent relaxation, CSA, Bonar score). Comparisons exceeding the significance threshold ($p < 0.05$) are included in (Table 6). Specifically, there were significant correlation results (42 genes) found with collagen organization, percent relaxation, and Bonar scoring as shown in (Table 6). From this list, 19 had Pearson correlation coefficients exceeding 0.7, indicating a strong correlation with other outcomes parameters and illuminating potential cellular pathways of tendinopathy.

The biomechanical properties of the tendons were also compared to the histopathologic scoring results. The Bonar degeneration scores were found to be strongly and significantly correlated with the peak stress at both strain magnitudes of the tendons ($\lambda=1.06$: $\rho = -.65$, $P < .01$; $\lambda=1.08$: $\rho = -.69$, $P < .01$, Figure 21), percent relaxation ($\lambda=1.06$: $\rho = -.62$, $P < .01$; $\lambda=1.08$: $\rho = -.60$, $P < .01$), and CSA of the tendons ($\rho = .61$, $P < .01$). The peak stress was strongly and significantly correlated with the CSA of the tendons ($\lambda=1.06$: $\rho = -.54$, $P = .01$; $\lambda=1.08$: $\rho = -.69$, $P < .01$, Figure 21) and percent relaxation ($\lambda=1.06$: $\rho = -.63$, $P < .01$; $\lambda=1.08$: $\rho = -.61$, $P < .01$).

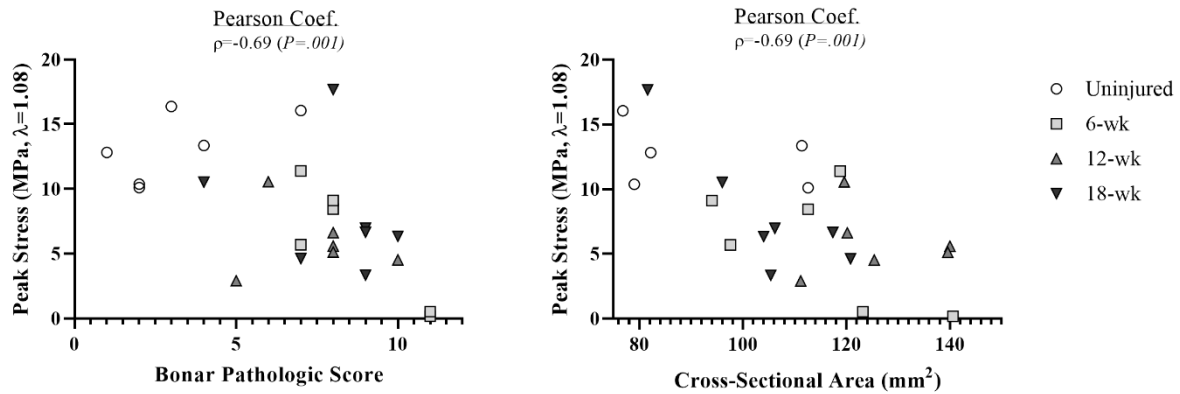


Figure 21. Representative scatterplots illustrating relationships between several outcome parameters. (Left) Peak stress was distinctly and significantly reduced in samples that demonstrated increased pathologic characteristics ($\rho = -.69$, $P = .001$). (Right) Peak stress was markedly and significantly decreased in samples with increased CSA ($\rho = -.69$, $P = .001$). Individual data points are marked with symbols according to their respective groups (i.e., circle (Control), square (6-wk), triangle up (12-wk), triangle down (18-wk)).

Table 6. Correlation analyses results.

	Gene ID	ρ	<i>P</i> -value
Col. Org. (%)	STOX1	0.774	0.01
	WNT9A	0.674	0.03
	ZNF212	-0.638	0.05
	CCDC106	-0.659	0.04
	RDH13	-0.665	0.04
	CAPN15	-0.669	0.03
	B3GNT8	-0.691	0.03
	THSD4	-0.697	0.03
	ZAP70	-0.737	0.02
	CD244	-0.740	0.01
	CMSS1	-0.771	0.01
	TMUB2	-0.794	0.01
	MYO7A	-0.803	0.01
	GRAMD4	-0.821	0.00
Peak Stress ($\lambda=1.08$)	THSD4	-0.649	0.04
CSA	BGLAP	0.743	0.01
	SLC1A3	0.741	0.01
	FABP4	-0.643	0.04
	TENT5B	-0.645	0.04
	ISLR	-0.647	0.04
	AKAP12	-0.659	0.04
	CBR3	-0.688	0.03
	FN3K	-0.689	0.03
	S100A1	-0.737	0.02
Bonar Score	PPARGC1B	0.874	0.00
	B3GNT8	0.843	0.00
	CCDC106	0.837	0.00
	THSD4	0.768	0.01
	MAP4K1	0.762	0.01
	NEU3	0.757	0.01
	TMUB2	0.703	0.02
	CD244	0.687	0.03
	TFR2	0.670	0.03
	TRAF3IP3	0.669	0.03
	NUP210	0.667	0.04
	C1orf216	0.659	0.04
	ZDHHC12	0.652	0.04
	WDYHV1	0.646	0.04
	TRPM2	0.638	0.05
	PAQR8	0.634	0.05
	PRR7	-0.746	0.01
	SLC6A17	-0.752	0.01

Conclusions

There are many insightful preclinical animal models of rotator cuff injury^(91,92,106,136); however, these models primarily rely on releasing either a portion of or the entire tendon from the humeral footprint followed by immediate or delayed reattachment. These models have fueled important discoveries in the tendon injury and repair field; unfortunately, they do not fully and/or accurately recapitulate the chronic degeneration of tendons that is observed without injury and/or trauma to the enthesis (i.e., aged population with a history of overuse resulting in chronically degenerated tendons prior to injury). Therefore, the purpose of this study was to fill this gap and generate and characterize a model of chronic rotator cuff degeneration that was not initially caused by enthesis disruption. As detailed in the results section, as early as 6-weeks persisting through the 18-week timepoint, this model generated samples exhibiting histopathological, collagen organization, and gene expression changes comparable to what has been documented in human tendinopathy.

Previous studies employing translational animal models to investigate RCT biomechanics have mostly performed destructive mechanical testing, reporting deleterious biomechanical changes with percent reductions in ultimate force to failure ranging from 58.1%⁽⁷⁰⁾ to 78.4%⁽⁶⁵⁾ depending on model type. Decreases in tendon biomechanical properties have also been noted in human tendon samples. Zellers et al. reported a 30.7% decrease in tendon dynamic shear modulus in Achilles tendons after injury / repair as compared to the uninjured side⁽¹³⁹⁾. At all timepoints, the CF model presented herein exhibited a marked decrease in peak stress ranging from 39 to 60% as compared to the uninjured group. The similarity in percent decrease of these mechanical property metrics seems to indicate that the CF model is inducing degenerative effects similar to what has

been documented to occur in humans secondary to injury. Stress relaxation testing has also been performed in an ovine enthesis damage model ⁽¹³⁶⁾, which reported deleterious changes at multiple timepoints and stretch levels, with percent decreases in peak stress ranging from 50% to 74% as compared to the uninjured group, corresponding closely with the changes in the CF model presented here. Similarly, the changes to the percent relaxation outcome parameter demonstrated by this CF model are remarkably similar to a recently characterized enthesis damage model⁽¹³⁶⁾, both exhibiting almost similar increases in percent relaxation secondary to injury. Considering the surgical insult was significantly different between these two models (i.e., direct enthesis damage versus direct tendon damage herein) the similarity in the decreased biomechanical properties seems to indicate that the biomechanical degenerative cascade is not damage type specific, and we hypothesize that any trauma (either acute such as a tear, or chronic such as overuse) will ultimately result in the same deleterious biomechanical changes. However, these data seem to indicate that the underlying mechanisms causing these changes (such as distributions in collagen alignment and/or gene expression) are different, possibly indicating that biomechanical testing alone is insufficient to understand the root cause of chronic tendon degeneration.

Increases in tendon CSA have also been reported previously. Derwin et al. reported marked increases in tendon CSA in a canine acute transection and repair model, ranging from 84% to 303% ⁽⁸³⁾. Likewise, similar increases have been reported in an ovine model without full tendon release, with increases ranging from 58% to 63% ⁽¹³⁶⁾. Additionally, increases in human tendon CSA following injury have been documented clinically. Zellers et al. reported a 525% increase in Achilles tendon CSA at 12-weeks post-repair from full-thickness tear ⁽¹³⁹⁾. Interestingly, this CF

model demonstrated only modest increase in CSA comparatively (17% to 42% depending on timepoint), these results demonstrate that full-thickness tears, as compared to tendon overuse, result in more pronounced geometric changes. This insight should have clinical utility in possibly determining the root cause of degeneration as the imaging of tendons and the resultant “thickening” observed, is a common parameter used to determine the level of degeneration in human patients ^(140,141).

The CF ovine tendons demonstrated pathologic changes consistent with human tendinopathy (Figure 17). Pathologic attributes noted across the CF tendon samples and timepoints are similar to those that have been described previously in human samples ^(111,126-128). Characteristic pathologic traits exhibited across all timepoints include disorganized collagen throughout the tendon body, increased vascular density, and marked expansion of tenoblast populations. The decrease in collagen organization that was qualitatively described by the pathologist was quantified through histomorphometry, illuminating a mean decrease in collagen organization of 16.9% across the CF groups at the three timepoints normalized to the uninjured group. Similar changes in collagen organization have been noted previously, with an ovine enthesis damage model reporting a mean decrease in collagen organization of 27.0% across multiple timepoints as well ⁽¹³⁶⁾. Furthermore, all of the pathologic changes exhibited by the CF samples were similar in magnitude and manifestation to what has been described previously in an ovine enthesis damage model ⁽¹³⁶⁾. Again, considering the differences of initial surgical insults between the two models, the similarity in manifestation of histopathological changes indicates that the degenerative cascade is not damage type specific. This observation is further supported by the existence of pathological

changes to the entirety of the tendon substance, even in regions that did not experience surgical insult.

This model and others ^(70,83,91,106) have demonstrated clearly that injury to one isolated portion of the tendon can cause changes to the entire bone-tendon-muscle construct. Additionally, this work has quantitatively demonstrated that the changes secondary to tendon injury are not isolated to the tendon. Histomorphometry analysis of the intramuscular adipose content within the infraspinatus muscle belly illuminated large relative increases in adipose content as early as 6-weeks (56.4% increase) and persisting through the 18-week timepoint (67.5% increase). Previous research has shown similar changes in muscle quality following injury, with one study having shown increases in pro-adipogenic gene expression and adipocyte quantity in an acute ovine injury model ⁽¹⁰²⁾. Similar reductions in associated muscle quality are a hallmark of human chronic degeneration, with assessment of fatty atrophy via magnetic resonance imaging being a primary method of diagnosis of rotator cuff injury, degeneration, and decreased surgical outcomes ^(62,142).

The samples in this study were semi-quantitatively graded following the Bonar pathologic grading scheme, which assigns numeric values to pathologic features associated with chronic tendon degeneration ⁽⁴⁰⁾. The mean Bonar scores for the CF tendon groups at all timepoints were within 1 point of the degenerated human control group ($\pm 10.2\%$). There was a strong and statistically significant correlation between the cellular activity/pathologic characteristics (encompassed in the Bonar scoring scheme) and the biomechanical performance of the tendons. Specifically, the Bonar

scores of the CF tendons had strong correlations with the peak stress, percent relaxation, and CSA of the tendons (Figure 7). Knowing collagen is the primary load-carrying constituent of tendons and also a key component graded in the Bonar scheme, these results are not surprising. However, these data highlight the importance of the microstructural composition and organization to the performance of the tendon.

Gene expression patterns across the 6- and 18-week timepoints in this model embodied many of the changes documented in literature regarding injured human rotator cuff tendons. Previous work by Jelinsky et al. [dataset] ⁽⁴¹⁾ measured global gene expression patterns in diseased human tendons obtained intraoperatively. Their data contains findings from many tendons, including the supraspinatus and subscapularis. Upon isolating the results from the lesioned supraspinatus tendons and normalizing to the unlesioned subscapularis tendons using the GEO2R tool, (Gene Expression Omnibus (GEO), RRID:SCR_005012), it was apparent the CF tendons exhibited similar overall gene expression patterns. Specifically, the CF samples had a 51.7% and 53.2% match in gene expression pattern across the entire transcriptome for the 6- and 18-week timepoints, respectively. Furthermore, the 6-week CF samples matched the collagen expression of the lesioned human tendon samples across 11 out of the 17 collagen genes, while the 18-week CF samples only matched expression with 4 of the same collagen genes. These results highlight the temporal changes in gene expression patterns secondary to tendon injury and provide reasoning to believe this model is an appropriate platform with which to investigate chronic rotator cuff degeneration. Additionally, these data provide the necessary information to illuminate potential target pathway(s) for therapy designs.

Ongoing work includes investigation of human cadaver tissue with the same analysis methodologies implemented herein, with the goal of enabling direct comparison between the two species. It is our hope that by investigating the pathologic and gene expression changes in a representative cohort of human samples with inferior mechanical performance, the underlying cellular pathways responsible for chronic degeneration may be illuminated, providing valuable insight for scientists working on therapeutics to arrest chronic degeneration.

While previous large animal translational models of chronic rotator cuff degeneration have been successfully implemented, this model separates itself as it does not rely on enthesis disruption yet is still capable of achieving similar degenerative pathology as what has been documented in humans. For this reason, it is our belief that this model will provide a valuable research platform to test biological therapies aimed at arresting/reversing the degeneration cascade prior to injury. Additionally, due to similarity in tendon size to the human rotator cuff tendons, this model is particularly well suited as a platform to assess scaffolds intended to improve repair outcomes for full tears of chronically degenerated tendons. Through comprehensive testing, we have demonstrated similar pathology, similar decreases in collagen organization, increased intramuscular adipose content, and similar gene expression patterns as what has been documented in humans. For these reasons, we believe that combed fenestration of the ovine infraspinatus tendon results in a translatable model of chronic rotator cuff degeneration.

Chapter 5- Bisphosphonate Impacts Tendon Mechanical Degradation in An Ovine Model of Osteoporosis

Introduction

It is startling that rotator cuff repair failures are 1.6 - 7.25 times as likely for osteoporotic (OP) patients as compared to those with healthy bone mineral density⁽⁵²⁻⁵⁴⁾. Due to the nature of OP, most research has focused on understanding the pathophysiology of bone loss and therapies to reverse those processes, with less research examining the changes to soft tissues associated with this condition. However, there is clear clinical evidence demonstrating inferior rotator cuff repair outcomes in patients with decreased bone mineral density (BMD) in the humeral head as compared to those with healthy BMD^(52,53,143-145). These studies have shown a decrease in both tendon insertion strength and repair outcomes in patients with low BMD, specifically in the humeral head. However, none of these small animal or clinical studies have specifically probed soft tissue mechanical properties in a non-destructive manner, enabling comparison of tissue mechanics and OP pathologic characteristics^(146,147).

Unfortunately for the 10 million people within the United States who are suffering from OP⁽⁵⁵⁾, the underlying mechanism(s) resulting in increased surgical failures to repairs in the shoulder has not yet been elucidated, resulting in a critical need to better understand the factors that impact rotator cuff repair surgical prognoses in patients with OP. Specifically, there is a lack of understanding of the changes to soft tissue biomechanical properties secondary to osteoporosis. With the current lack of understanding of the interplay between skeletal and connective tissue,

studies that enable direct comparison between osseous tissue condition and connective tissue pathology and/or microstructure are needed.

Several therapies have been implemented to reverse bone loss for patients with OP, such as bisphosphonates (BP) ⁽⁵⁶⁾. Bisphosphonate treatments have been widely implemented clinically, with great success, with large, randomized, placebo-controlled trials showing significant reductions (as large as 50%) in vertebral body fractures for example⁽¹⁴⁸⁾. While clinical improvements such as these should be celebrated, it is necessary and prudent to also fully understand the effects such therapies have on adjacent soft tissue tissues. Recent work has documented *in vitro* changes to proliferation and gene expression of human epithelial fibroblasts secondary to bisphosphonate exposure; however, studies investigating the changes to other cell types such as tendon fibroblasts or non-existent. Additionally, work investigating the *in vivo* impact of this therapy on connective tissue function is needed.

Therefore, the goal of this study was to benchmark biomechanical and histopathological changes within the rotator cuff (i.e., infraspinatus – humeral head construct) that occur secondary to an induced osteoporotic state in an ovine large animal model as a means of assessing whether soft tissue is altered prior to injury. Our hypothesis was that soft tissue biomechanical properties are altered in the osteoporotic condition, potentially contributing to the increased surgical failures. Secondly, due to the prevalence of BP treatments clinically, the impact of BP treatments on

those same soft tissue biomechanical properties was assessed under the hypothesis that altered cellular populations in the enthesis region would impact the mechanical properties of the tendons.

Materials and Methods

All surgeries were performed with approval from Institutional Animal Care and Use Committee (IACUC, Colorado State University #18-7872A).

Ovine OP Model Development

Osteoporosis was induced in ten skeletally mature (≥ 3.5 years of age) *ovis aries* ewes resulting in n=20 humerus infraspinatus tendon constructs (HTCs) which were allocated to two groups (n=10 HTCs in each group). Similar to previous studies^(149,150), a combination of dietary deficiency (low calcium, low vitamin D), ovariectomy (OVX), and steroid administration (intramuscular 500mg methyl-prednisolone acetate every three weeks starting at 2 weeks and ending at 16 weeks post-OVX) were used to induce osteoporosis (Figure 22). Sheep were monitored daily throughout the study period for any signs of adverse events or complications and to evaluate pain, lameness/ambulatory function, and incisional site healing. Sheep were fed and provided with tap water *ad libitum*. Sheep were housed in pasture with access to a three-sided shelter for the duration of the study.

Osteoporosis was validated with DXA (T-score ≥ 3.5) at 16 weeks post OVX, at which point n=4 weekly intravenous injections were administered according to treatment group, with the bisphosphonate (BP) group receiving 0.031mg/kg and the sham treatment group (PBS) receiving the same volume injection of 0.9% phosphate buffered saline. Animals were humanely euthanized 28 weeks post-OVX (intravenous overdose of pentobarbitone sodium 88 mg/kg). The HTC's were immediately (<1 hr.) harvested following euthanasia. Uninjured HTC's (n=6) were harvested from animals in unrelated studies; the cross-sectional areas, Bonar scores, and intramuscular adipose content values from these samples have been previously published⁽¹³⁶⁾ and are being redisplayed here with permission from the copyright holder.

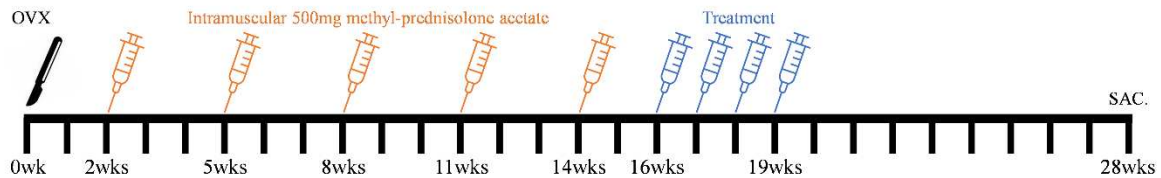


Figure 22. Experimental design/treatment timeline. Ovariectomy occurred in all OP sheep at zero weeks. Intramuscular steroid injections were administered every three weeks starting at 2 weeks and ending at 16 weeks post-OVX. Beginning 16 weeks post-OVX, the BP and PBS group sheep were given weekly injections of their respective treatments. Sheep were euthanized at 28 weeks post-OVX.

Tendon Mechanical Analysis

As previously described⁽¹³⁶⁾, HTC's were denuded of soft tissues with great care to not damage the tendon. Cross-sectional area (CSA) measurements were taken of each tendon prior to mechanical testing using a custom area micrometer. Following CSA measurement, the humeri were mounted in a polyvinyl chloride sleeve using a strong two-part hard casting resin (SmoothCast 321, Smooth-

On, Macungie, PA). The sleeve was then clamped to a servo-hydraulic load frame (Model 858, MTS Corp. Eden Prairie, MN), allowing anatomically accurate loading of the tendon^(3,71). Prior to testing, tendons remained unloaded for a duration of one hour to allow for viscoelastic equilibrium^(68,117-121). Tendons were gripped using a custom cryo-grip maintained at -10°C ⁽¹³⁶⁾. Subsequently, tendons were subject to a static preload of 5N for two minutes, at which point a reference gage length was measured. Non-destructive cyclic testing at 10% stretch were randomly performed at two frequencies, 1 Hz and 0.1 Hz. Tendons were allowed to recover for a period of 1,000 seconds between cycles⁽¹²⁰⁾. At all times during dissection and testing, tendon hydration was maintained with physiological saline spray at ten-minute intervals. Force-displacement data was collected at 100 Hz and these raw data were fit to an established strain energy function (see Viscoelastic Modeling section).

Bone μCT Analysis

Upon completion of the nondestructive biomechanical testing, samples were bisected via diamond bandsaw through the enthesis to improve fixation⁽⁷¹⁾ and subsequently placed in 10% neutral buffered formalin (≥ 7 days). Specimens were micro computed tomography (μCT) scanned using the following parameters: isotropic resolution, $37\ \mu\text{m}$; voltage, 70 kVp; current, 114 μA ; and integration time, 500 ms (Scanco μCT 80, Scanco USA Inc. Wayne, PA). The analysis region for each specimen was set as a 6mm diameter cylinder directly under the HTC enthesis, excluding the fibrocartilaginous transition zone (Figure 23A). The long axis of the cylindrical region of interest was maintained parallel to the tendon insertion. The following quantitative parameters were measured (SCANCO Evaluation V1.1.15.0, SCANCO Medical): bone volume fraction (BV/TV),

trabecular number (Tb.N), trabecular thickness (Tb.Th), trabecular spacing (Tb.Sp), specific bone surface (BS/BV), connectivity density (Conn.D), structure model index (SMI), and degree of anisotropy (DA).

Histomorphological Analysis

Following fixation and μ CT scanning, samples were decalcified using an 8% trifluoroacetic acid solution^(136,138). Samples were subsequently processed using standard formalin fixed paraffin embedded techniques to display the transition from mid-body tendon to fibrocartilaginous insertion to humeral bone. Three 5 μ m thick slides were created from each sample, with one slide stained with hematoxylin and eosin (H&E), one slide stained with Picro-sirius red, and one stained with RGB Trichrome⁽¹⁵¹⁾.

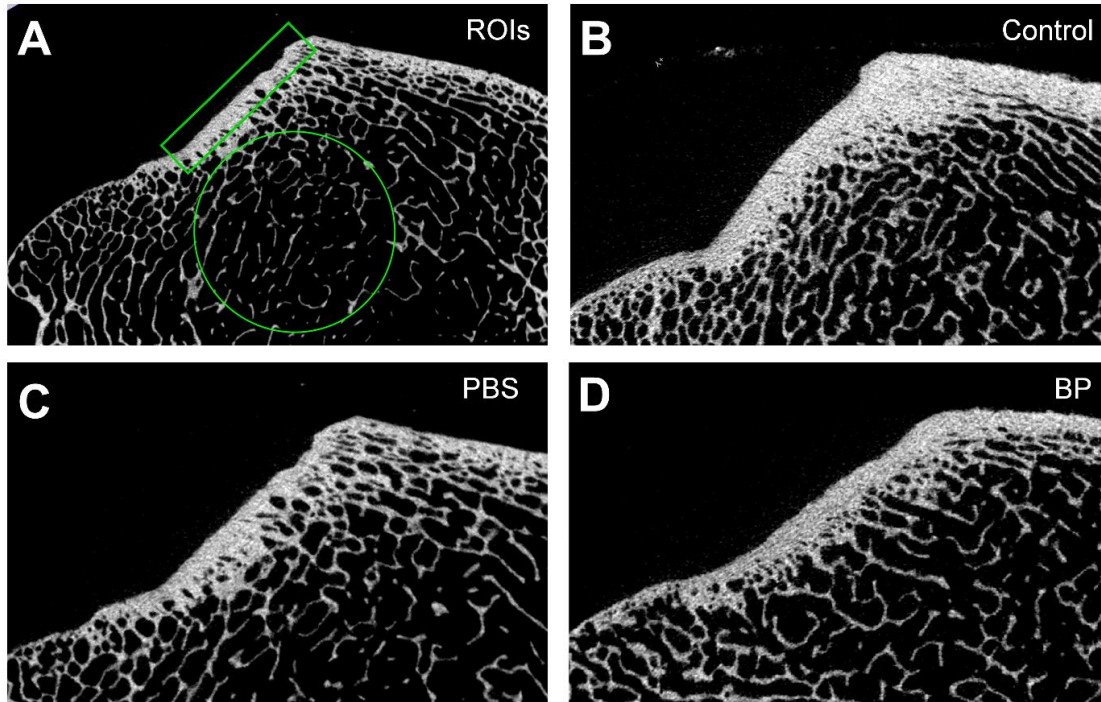


Figure 23. Representative microCT images. (A) Circle illustrates microCT analysis region. Square indicates tendon enthesis (insertion). (B) Representative image of a sample from the Control group. (C) Representative image of a sample from the PBS group. (D) Representative image of a sample from the BP group. The samples chosen for each group exhibited the median bone volume fraction value for their respective group.

Collagen organization was assessed through utilization of picro-sirius red stained slides⁽¹³⁶⁾. Briefly, slides containing approximately 40 mm of the proximal infraspinatus tendon and enthesis/bone were prepared and imaged using polarized brightfield microscopy at 20x magnification (Olympus BX61VS, Center Valley, PA). All samples were imaged in one session with 40ms exposure to ensure no variation in imaging capture process or polarization lens configuration. A machine learning algorithm (Image-Pro Premier v9.2, Rockville, MD) was programmed to calculate percent area of the organized / disorganized collagen seen within the

analysis region within the tendon. Region of analysis included the most proximal 25mm of tendon but did not include the fibrocartilaginous enthesis zone.

Fatty atrophy of the associated rotator cuff muscles is correlated with decreased rotator cuff repair surgical outcomes⁽¹⁵²⁾. Therefore, intramuscular adipose content was assessed in the samples to determine potential differences between groups and whether the degree of fatty infiltration was correlated with tendon mechanics. Biopsies (10mm x 10mm x 3mm) were collected from the center of the infraspinatus muscle belly and processed using standard paraffin-embedded histology techniques which were stained with H&E. Total tissue area and adipose tissue area were quantified (Image-Pro Plus, RRID:SCR_007369). To eliminate the effect of differing sample sizes and histological artifact, the measured adipose tissue area was normalized to the total tissue area to generate percent adipose tissue area. To eliminate area selection bias, the percent adipose tissue area was calculated at three randomly chosen uniformly sized analysis regions within each sample, which were subsequently averaged. The veterinary pathologist in residency viewed the segmentation images to ensure accuracy and consistency of region selection across all samples.

Histopathological analysis

As outlined previously⁽¹³⁶⁾, H&E slides were graded by a blinded veterinary pathologist in residency using the semiquantitative Bonar tendinopathy scale, which is designed to quantify pathologic characteristics of tendinopathy^(40,153). Samples were assessed for: (1) tenocyte reactivity, (2) angiogenesis, (3) tendon bundle organization and polarization, and (4) deposition of

ground substance. Each of these four characteristics were graded on a 4-point scale ranging from 0 (normal/healthy) to 3 (markedly “degenerated” / pathologic)⁽⁴⁰⁾. These scores were then summed to give an overall score between 0 (pathologically normal) and 12 (pathologically degenerated) for each tendon section. Upon completion of the semi-quantitative grading, the pathologist was unblinded to treatment and made gross observations regarding structural and/or tissue type differences noted between groups that were not captured by the Bonar scoring system.

Tendon insertional structure and characteristics were assessed through semi-quantitative scoring and descriptive pathology. The ovine infraspinatus tendon and its humeral enthesis have discrete morphologic characteristics when stained with RGB-trichrome and viewed using bright field microscopy⁽¹⁵¹⁾. The lateral tendon body is comprised of larger, tightly organized tendon bundles of parallel fibers (light blue), the boundaries of which are delineated by thin sheets of variably oriented, looser fibers (red) (Figure 26). There is a variably abrupt transition from this lateral organization to the medial tendon body where tendon bundles are smaller and are separated by increasing amounts of proteoglycan rich, loose connective tissue (dark blue). Within these areas fibroblasts often have a chondroid morphology, with moderate amounts of cytoplasm and occasional lacunae. In some sections the lateral extreme of the peri-entheseal tendon transitions to hyalin cartilage (purple). These areas are anatomically adjacent to the hyalin cartilage of the articular joint of the humeral head. As the tissues of the tendon and tendon to bone interface are shaped by mechanobiological factors⁽¹⁵⁴⁾, this transition from the lateral to medial morphology appears adapted to translating the tensile forces of the lateral body to the medial, compressive forces over the joint. This transition zone often extends to the enthesis proper. To assess differences

in the insertional structure, the degree of interdigitation of the bone-fibrocartilage interface was scored on a 1-5 scale by a veterinary pathologist. Semi-quantitative scoring of the enthesial interdigitation was performed on the tendon insertion spanning 1mm from the external surface to the mid enthesis. Interdigitation of the bone and MFC that is regular in width and spans less than half of the total width of the MFC is given a score of 1. For each of the following features an additional point is awarded: interdigitation spans greater than half the width of the MFC zone; interdigitations vary in width; there is more than one island of bone isolated by MFC in a 200X microscopic field; projections of MFC abut medullary spaces.

Viscoelastic Modeling

It has previously been demonstrated that quasilinear viscoelasticity (QLV) can successfully be implemented to describe the non-linearity seen in soft tissue elastic and viscous responses to arbitrary strain inputs⁽²⁸⁻³⁰⁾. As outlined by Fung⁽³¹⁾, tissue response to uniaxial loading can be approximated in terms of engineering strain by:

$$\sigma[\varepsilon(t), t] = \int_0^t G(t - \tau) \frac{d\sigma^e(\varepsilon)}{d\varepsilon} \frac{d\varepsilon(\tau)}{d\tau} d\tau$$

Equation 5

where $G(t)$ represents the reduced relaxation modulus which captures the viscous behavior, and $\sigma^e(\varepsilon)$ represents the non-linear elastic (i.e., instantaneous hyperelastic) behavior. In this work, $G(t)$ was modeled through implementation of a Prony series defined as:

$$G(t) = G_{\infty} + \sum_{i=1}^4 G_i e^{-t/\tau_i}.$$

Equation 6

In this formulation, the relaxation modulus terms (G_i) were constrained to be positive with their summation equal to one⁽²⁸⁾. Time constants were assigned to decadal increments of 0.1, 1, 10, and 100 seconds. To model the hyperelastic behavior of the tendons, a 1-term Ogden constitutive equation was implemented:

$$\sigma^e(\varepsilon) = \frac{2\mu}{\alpha} [(\varepsilon + 1)^{\alpha-1} - (\varepsilon + 1)^{-\alpha/2-1}],$$

Equation 7

where μ and α are experimentally derived material constants used to represent the stretch-dependent material stress⁽²⁷⁾. When written in terms of stretch (λ), Equation 7 takes the following form:

$$\sigma = \frac{2\mu}{\alpha} [\lambda^{(\alpha-1)} - \lambda^{-(0.5\alpha+1)}].$$

Equation 8

By differentiating Equation 8 with respect to λ , the formulation of Young's Modulus as a function of stretch is provided:

$$\frac{d\sigma}{d\lambda} = \frac{2\mu}{\alpha} \left[(\alpha - 1)\lambda^{(\alpha-2)} + \left(\frac{\alpha}{2+1} \right) \lambda^{-(0.5\alpha+2)} \right].$$

Equation 9

This resulted in a total of seven fitted terms: μ , α , G_1 , G_2 , G_3 , G_4 , and G_∞ . Data fitting of the biomechanical data was performed using Matlab's (R2020a, Mathworks, Natick, MA) *fmincon* function to determine the set of fitted coefficients while minimizing the sum of the root-mean-squared errors (RMSE) across each frequency individually⁽¹⁵⁵⁾. The variables derived from each frequency were then averaged to provide for one set of variables for each specimen. The Ogden variables were then used in conjunction with Equation 9 to generate a plot of Young's modulus vs stretch ($1.00 \leq \lambda \leq 1.10$). Each of the experimental groups were plotted and a nonlinear fit was assigned to the means of each group. The best-fit values and Young's modulus values at each stretch value are included in the Supplemental Material section.

Statistical analysis

All comparisons between groups were made using a one-way ANOVA followed by Tukey's post-hoc test (GraphPad Prism v9.0.0, GraphPad Software, San Diego, CA). Data sets that did not pass the equal variance (Bartlett's test) or normality assumptions (Anderson-Darling test) of the one-way ANOVA, a Kruskal-Wallis test was performed. The left and right limb from each animal were treated as independent observations for all statistical analyses. Prior to plotting individual nonlinear fits to each group for Young's modulus vs stretch, an Extra Sum-of-Squares F Test was performed to determine if one curve could fit all data. The significance threshold was set to $\alpha =$

0.05 for all statistical tests. Two tendons in the osteoporotic group were damaged during dissection; thus, a decision was made to exclude those samples from the study. Sample numbers in each grouping were: n=6 uninjured shoulders (Control), n=8 osteoporotic plus saline injection shoulders (PBS), and n=10 osteoporotic plus bisphosphonate injection shoulders (BP). Sample sizes were verified as adequate following a post-*hoc* power test based on tendon mechanical properties (hyperelastic μ , power=0.799). Correlation analyses between all outcome parameters were performed to help ascertain whether tendon mechanics or microstructure were changed according to degree of bone loss; results of Spearman correlation coefficients and associated P-values were reported. Correlation strength was characterized as follows: slight (0 to .2), fair (.21 to .4), moderate (.41 to .6), strong (.61 to .8), and very strong (.81 to 1.0)⁽¹⁵⁶⁾.

Results

All animals survived to the study end date; no intra- or post-operative complications were noted.

Micro-CT

Marked decreases in trabecular bone quantity and structure were noted in both the PBS and BP groups. A 57.6% reduction in bone volume fraction was noted in the PBS group ($p < 0.001$) as compared to the Control group, while the BP group exhibited a 49.9% reduction ($p < 0.001$, Figure 24A) in the same metric. The PBS and BP groups demonstrated decreased trabecular number; with percent decreases as compared to the Control group of 47.9% ($p = 0.001$) and 39.8% ($p = 0.013$,

Figure 24B) for the PBS and BP groups, respectively. The OP groups exhibited decreased trabecular thickness; with percent decreases as compared to the Control group of 20.3% ($p < 0.001$) and 16.7% ($p = 0.002$, Figure 24C) for the PBS and BP groups, respectively. The PBS and BP groups demonstrated increased trabecular spacing; with percent increases as compared to the Control group of 142.5% ($p = 0.001$) and 80.5% ($p = 0.013$, Figure 24D) for the PBS and BP groups, respectively.

The OP groups exhibited increased specific bone surface; with percent increases as compared to the Control group of 26.4% ($p = 0.001$) and 20.6% ($p = 0.007$, Figure 24E) for the PBS and BP groups, respectively. The PBS and BP groups demonstrated decreased connectivity density; with percent decreases as compared to the Control group of 71.1% ($p < 0.001$) and 56.5% ($p < 0.001$, Figure 24F) for the PBS and BP groups, respectively. Analysis of the structure model index of the trabeculae revealed a shift towards a cylindrical rod shape as compared to the control group, with percent increases as compared to the Control group of 46.2% ($p < 0.001$) and 38.6% ($p < 0.001$, Figure 24G) for the PBS and BP groups, respectively. No significant differences in degree of anisotropy were noted between groups (Figure 24H). Representative images of samples from each group are displayed in Figure 23B,C,D.

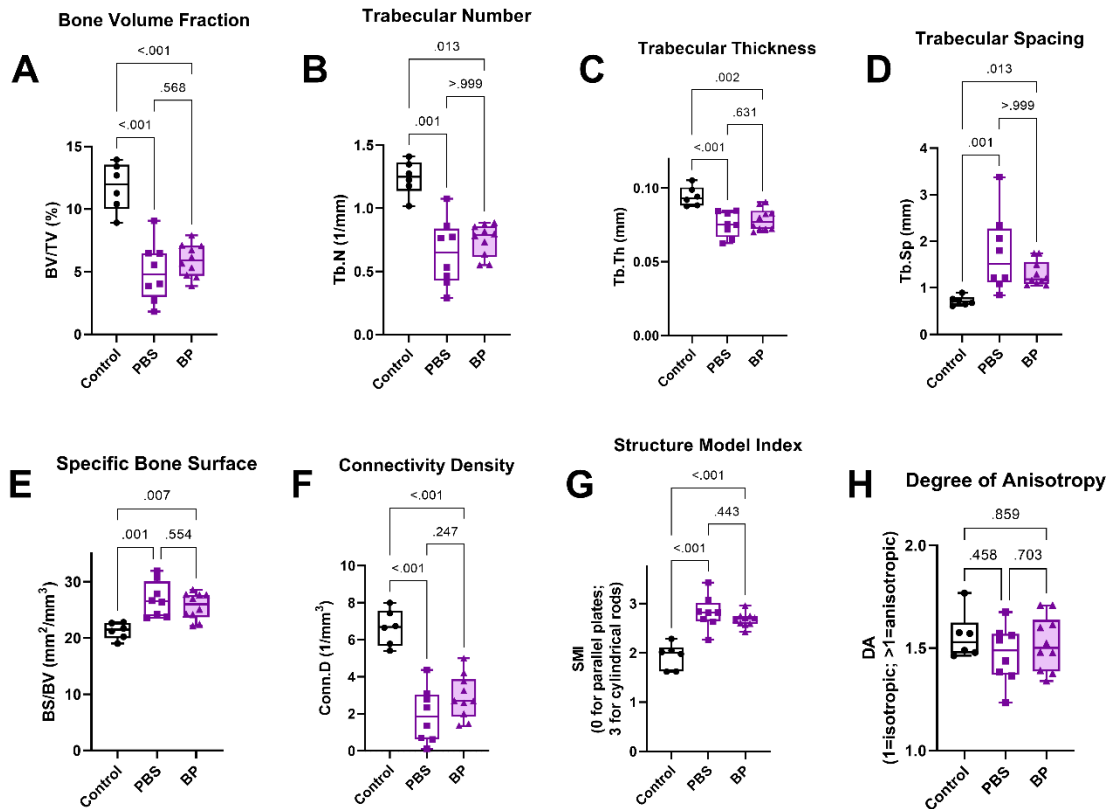


Figure 24. MicroCT outcome parameters. (A) Bone volume fraction was reduced in both the PBS ($p < 0.001$) and BP ($p < 0.001$) groups as compared to the Control group. (B) Trabecular number was decreased in both the PBS ($p = 0.001$) and BP ($p = 0.013$) groups. (C) Trabecular thickness was decreased in both the PBS ($p < 0.001$) and BP ($p = 0.002$) groups. (D) Trabecular spacing was increased in both the PBS ($p = 0.001$) and BP ($p = 0.013$) groups. (E) The specific bone surface was increased in the PBS ($p = 0.001$) and BP ($p = 0.007$) groups. (F) The connectivity density was decreased in both the PBS ($p < 0.001$) and BP ($p < 0.001$) groups. (G) The structure model index was increased in the PBS ($p < 0.001$) and BP ($p < 0.001$) groups. (H) The degree of anisotropy was similar for all groups. Statistical test: one-way ANOVA with Tukey's post hoc test (A,C,E,F,G,H) and Kruskal-Wallis test (B,D). Box plot indicates median and interquartile range; whiskers indicate maximum and minimum values. Individual datum points are overlaid.

Histomorphological assessment of collagen fiber alignment

Quantitative measurements of collagen organization were made through implementation of Picro-Sirius red staining followed by analysis of birefringence patterns with polarized light microscopy. To determine potential differences between treatment groups, areas of organized collagen were normalized to total analysis area. These measurements revealed no significant differences between groups, with collagen organization ratios of 61.6%, 61.7%, and 56.8% for the PBS, BP, and Control groups, respectively (Figure 25A).

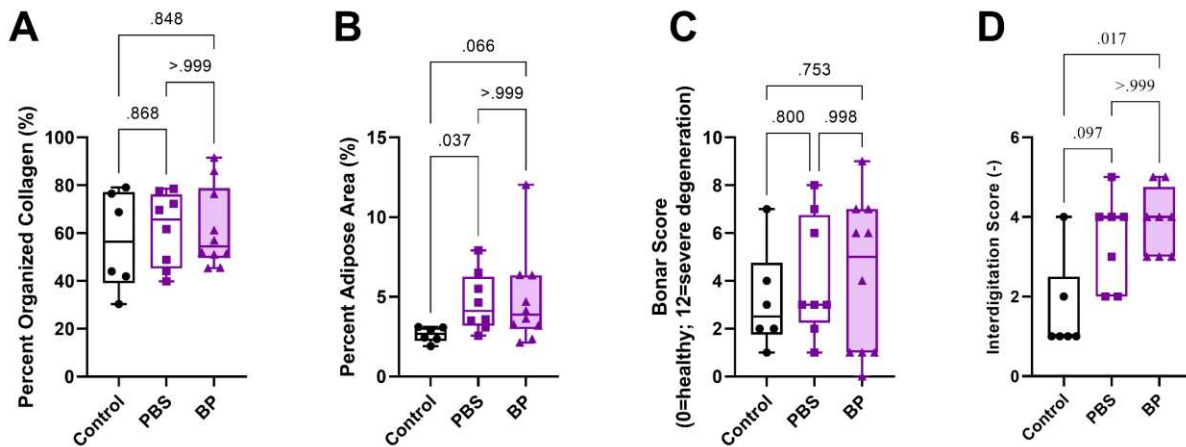


Figure 25. Tendon pathological scoring and histomorphometry analyses results. (A) No differences were noted in tendon collagen organization between treatment groups. (B) Increased intramuscular adipose content was measured in the PBS ($p=0.037$) and BP ($p=0.066$) groups as compared to the Control group. (C) No significant differences were noted in tendon degenerative pathological scoring results between treatment groups. (D) Increased semi-quantitative interdigitation scores were noted in the PBS ($p=0.097$) and BP ($p=0.017$) groups. Statistical test: one-way ANOVA with Tukey's post hoc test (A,B) and Kruskal-Wallis test (C,D). Box plot indicates median and interquartile range; whiskers indicate maximum and minimum values. Individual datum points are overlaid.

Histopathology Results

Semi-quantitative Bonar scoring for pathological characteristics of tendon mid-body degeneration did not reveal significant differences between groups (Figure 25C). The PBS and BP groups exhibited mean scores of 4.1 and 4.2, respectively; indicating all groups showed minimal pathological signs of tendon degeneration. As compared to the Control group (Figure 26A), both OP tendon groups displayed increased presence of tenocytes (Figure 26B,C, *), ground substance (Figure 26B,C, †), and collagen disorganization (Figure 26B,C) within the tendon body. Within the OP groups, the BP group exhibited increased pathologic tendencies in those categories. Interestingly, the BP treatment group demonstrated reduced vascularity as compared to the Control group, whereas the PBS group displayed increased vascularity in the tendon mid-body.

While not within the scope of Bonar histologic scoring, the cellular distribution of the enthesis was observed to be notably different between the BP and the PBS groups (Figure 26B,C). In the PBS group, the non-mineralized fibrocartilage is markedly paucicellular (Figure 26B, ‡); while in the BP group, there is a moderate to marked increase in mesenchymal cells in the fibrocartilage (Figure 26C, §). The increased mesenchymal cell population is primarily composed of chondrocytes, with a large proportion having prominent lacunae. As compared to the Control samples (Figure 26D, arrow), a notable decrease in tidemark symmetry and presence was noted in the PBS group samples (Figure 26E, arrow). This decrease was less pronounced and sometimes non-existent in the BP samples (Figure 26F, arrow). Deep to the enthesis, the humeral trabecular network of the healthy shoulders is mildly more robust than either OP group as evidenced by increased trabecular density and/or thickness.

The fibrocartilagenous transition of the humeral enthesis of the infraspinatus tendon can be broken into four distinct zones by light microscopy when stained with the RGB-trichrome stains⁽¹⁵¹⁾. These zones have discrete boundaries in health when stained by these methods; bone (intense turquoise); mineralized fibrocartilage (MFC, light turquoise); non-mineralized fibrocartilage (nMFC, red); and tendon (blue) (Figure 26). These discrete boundaries are thought to represent a physiochemical threshold for the stains in what is a truly gradient biomaterial transition between these mechanically disparate materials (tendon and bone). This staining artifact, of discrete boundaries between enthesal zones appears in health as a smooth, regular tinctorial demarcation between the MFC and nMFC zones; however, sometimes this line of demarcation is lost and there is apparent interweaving of these zone with variable tinctorial gradations that can extend from the tendon to the bone. This was most often seen in sections demonstrating increased interdigitation of the bone to MFC junction. The interdigitation between these zones was most extreme and consistent in both the PBS (Figure 26H) and BP (Figure 26I) groups as compared to the Control (Figure 26G). Specifically, the semi-quantitative scoring revealed increased interdigitation levels in the PBS ($p=0.097$) and BP ($p=0.017$, Figure 25D) groups.

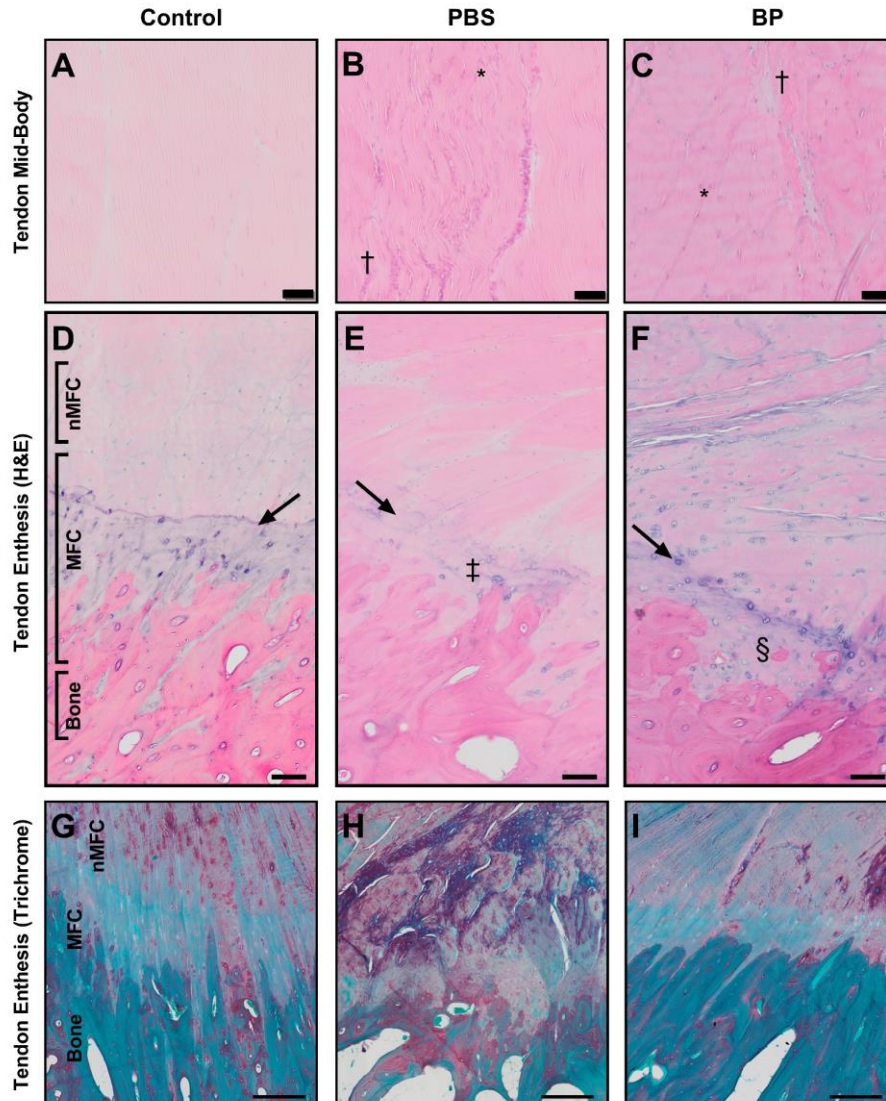


Figure 26. Representative histology micrographs of the Control, PBS, and BP groups. (A,B,C) H&E-stained sections of tendon mid-body specimens. Decreased collagen organization noted in the PBS (B) and BP (C) samples throughout. Increased tenocytes (*) and increased ground substance (†) were noted in the PBS (B) and BP (C) samples. (D,E,F) H&E-stained sections of tendon enthesis specimens. As compared to the Control samples (D, arrow), the PBS (E) and BP (F) samples exhibited decreased tidemark (arrow) symmetry and prominence. The PBS samples exhibited a notable decrease in cellularity within the fibrocartilage (‡). The BP samples demonstrated increased mesenchymal cell population within the fibrocartilage (§). (G,H,I) Trichrome stained sections of tendon enthesis specimens. As compared to Control samples (G), the PBS (H) and BP (I) samples exhibited increased interdigitation of the of the bone to MFC junction. Sections are 5µm thick, formalin fixed, trifluoroacetic acid demineralized, and paraffin embedded. Scale bar: 50µm (A,B,C), 100µm (D,E,F), and 200µm (G,H,I).

Viscoelastic Modeling

The PBS group exhibited markedly decreased biomechanical properties as compared to the Control group, exemplified by a 56.7% ($p=0.083$, Figure 27A) decrease in Ogden μ term and a 64.9% ($p=0.026$, Figure 27B) increase in non-linearity (α). Interestingly, no significant differences were noted in hyperelastic μ term or non-linearity (α) terms between the BP and Control groups, with mean μ values of 60.6 MPa ($p>0.999$, Figure 27A) and 62.0 MPa and mean α values of 16.4 ($p=0.463$, Figure 27B) and 13.1 for the BP and Control groups, respectively. All QLV fitting was carried out successfully with mean root mean square error (RMSE) values of 0.33 MPa, 0.48 MPa, and 0.46 MPa (Figure 27C) for the PBS, BP, and Control groups, respectively. As a means to quantify the RMSE values to stress values, RMSE was normalized to cyclic peak stress, which resulted in mean total error for all samples to be 3.2%, 2.9%, and 2.5% (Figure 27D) for the PBS, BP, and Control groups, respectively. No significant differences were noted in tendon CSA between treatment groups (Figure 27E). Young's modulus values for each group were plotted against stretch (Figure 27F). An Extra Sum-of-Squares F Test rejected the null hypothesis and verified that one curve could not adequately fit all groups ($p<0.0001$). The PBS group exhibited decreased Young's modulus values at all stretch levels below 1.10 ($\lambda=1.00$, $p=0.083$; $\lambda=1.01$, $p=0.092$; $\lambda=1.02$, $p=0.111$; $\lambda=1.03$, $p=0.111$; $\lambda=1.04$, $p=0.103$; $\lambda=1.05$, $p=0.118$; $\lambda=1.06$, $p=0.145$; $\lambda=1.07$, $p=0.191$; $\lambda=1.08$, $p=0.248$; $\lambda=1.09$, $p=0.372$; $\lambda=1.10$, $p=0.629$; Figure 28). The BP group and the Control group exhibited similar Young's modulus values at all stretch levels ($p>0.999$ for all λ , Figure 28). At all stretch levels, the BP group exhibited increased Young's modulus values as compared to the PBS group ($\lambda=1.00$, $p=0.073$; $\lambda=1.01$, $p=0.068$; $\lambda=1.02$, $p=0.075$; $\lambda=1.03$,

$p=0.075$; $\lambda=1.04$, $p=0.063$; $\lambda=1.05$, $p=0.044$; $\lambda=1.06$, $p=0.038$; $\lambda=1.07$, $p=0.038$; $\lambda=1.08$, $p=0.039$;
 $\lambda=1.09$, $p=0.044$; $\lambda=1.10$, $p=0.043$; Figure 28).

Differences were noted in the QLV reduced relaxation terms between the treatment groups. Specifically, the BP group exhibited increased mean G_1 term values as compared to the PBS ($p=0.058$) and Control ($p=0.229$, Figure 29A) groups. The BP group exhibited decreased G_2 term values as compared to the PBS ($p=0.075$) and Control ($p=0.526$, Figure 29B) groups. All groups exhibited similar G_3 and G_4 term values (Figure 29C,D). The PBS group exhibited decreased G_∞ term values as compared to the Control group ($p=0.136$) and the BP group ($p=0.306$, Figure 29E). Mean reduced relaxation modulus function plots for each group best illustrate the relaxation behavior differences between the different groups (Figure 29F).

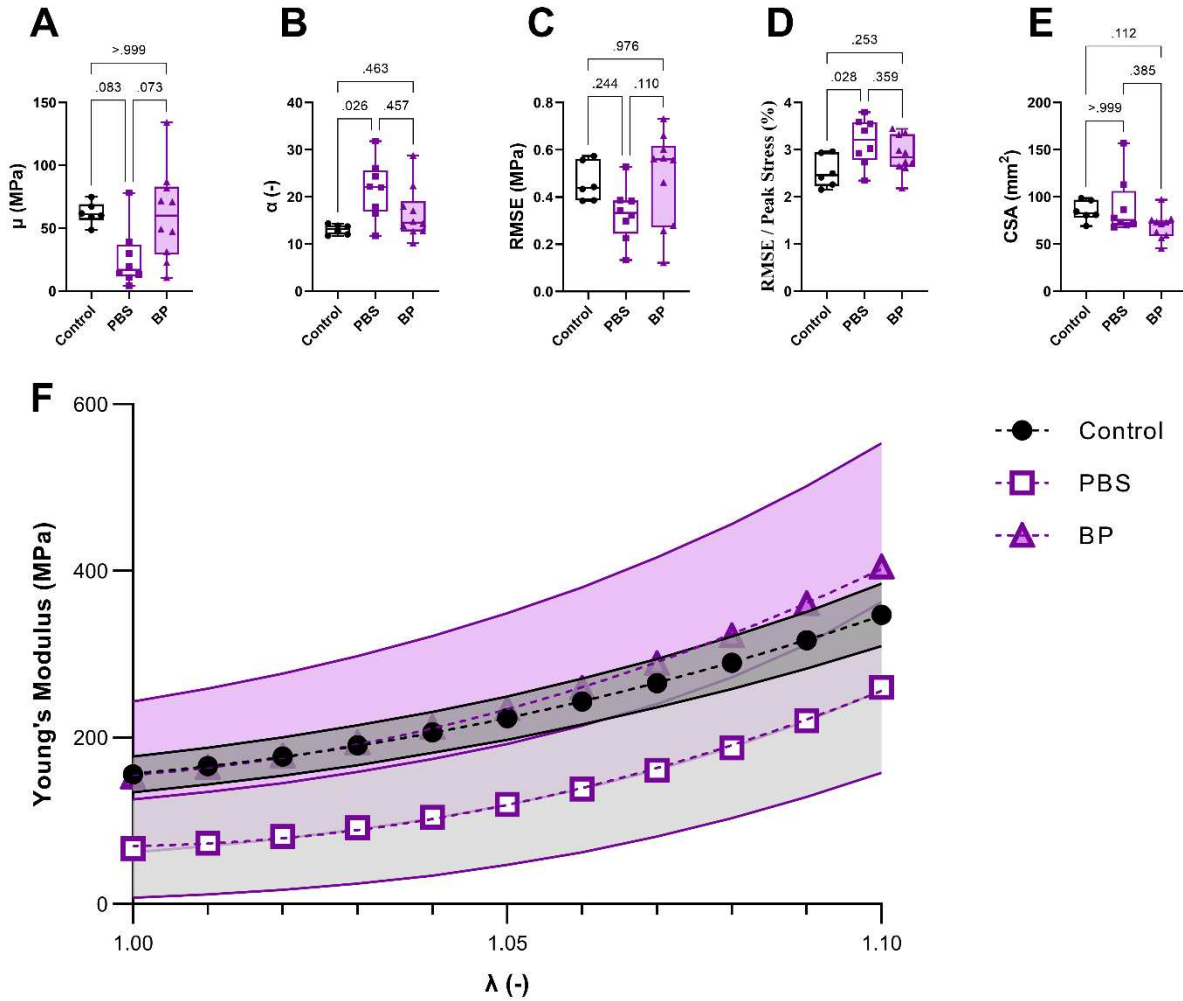


Figure 27. Hyperelastic strain energy function fitting results. (A) A decrease in the Ogden μ term was noted in the PBS group as compared to the Control group ($p=0.083$). The BP group exhibited increased μ term values as compared to the PBS group ($p=0.073$) which were similar to those exhibited by the Control group ($p>0.999$). (B) An increase in the Ogden non-linearity term (α) was noted in the PBS group as compared to the Control group ($p=0.026$), while the BP group exhibited values closer to the Control group ($p=0.463$). (C) RMSE values were below 0.5 MPa for all groups. (D) Normalized fitting errors across all groups were below 3.2%. (E) No significant differences were noted in tendon CSA between treatment groups. (F) Young's modulus vs Stretch plot. Symbols indicate group means, shaded regions illustrate standard deviation of the group samples, and dotted lines indicate best-fit nonlinear regressions. Statistical test: one-way ANOVA with Tukey's post hoc test (C,D) and Kruskal-Wallis test (A,B,E). Box plot indicates median and interquartile range; whiskers indicate maximum and minimum values. Individual datum points are overlaid. An Extra Sum-of-Squares F Test was performed to reject the null-hypothesis that one curve could adequately fit all data ($p<0.0001$; F).

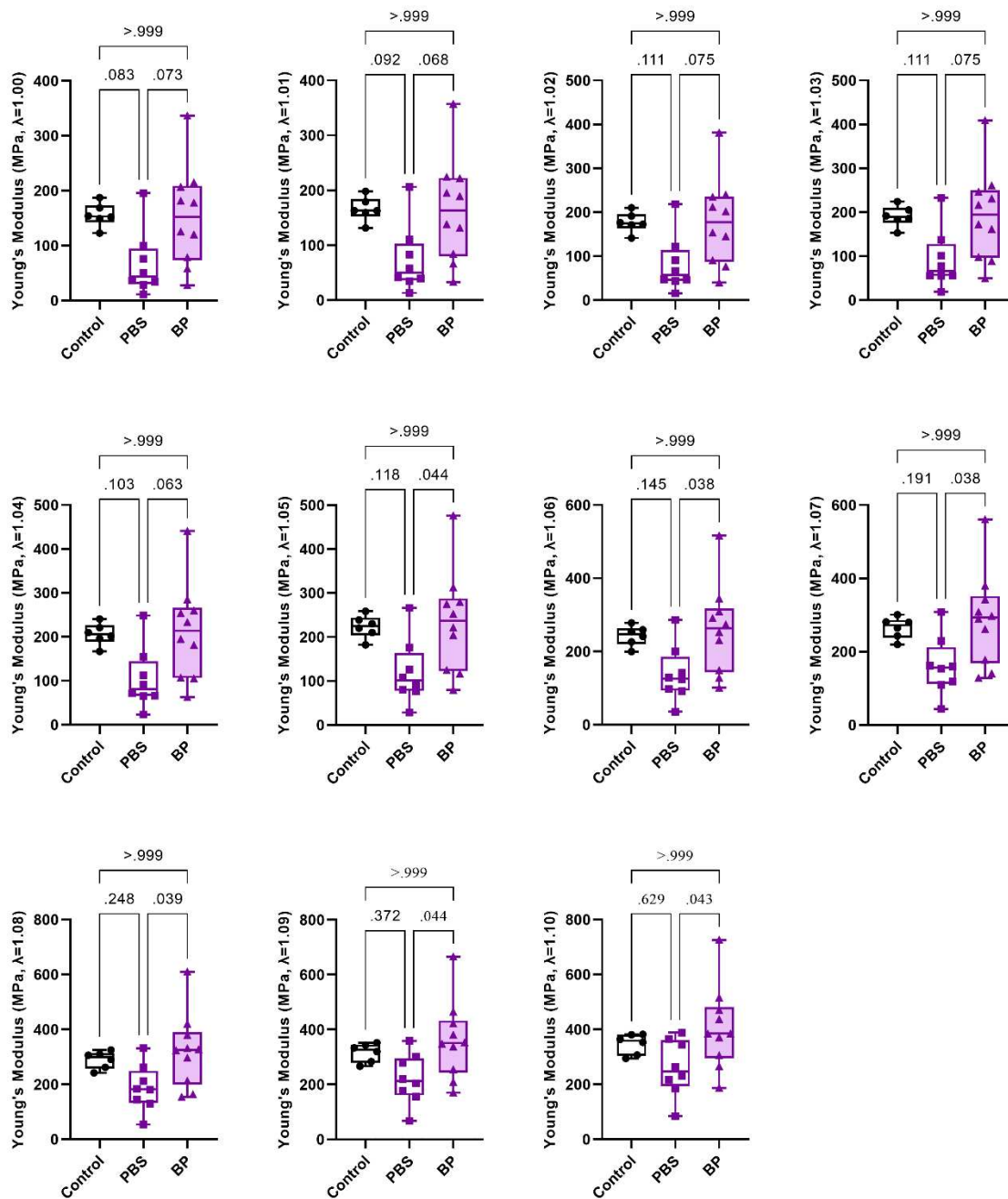


Figure 28. Young's modulus values for all groups at discrete stretch levels ($1.00 \leq \lambda \leq 1.10$). Statistical test: Kruskal-Wallis test (all). Box plot indicates median and interquartile range; whiskers indicate maximum and minimum values. Individual datum points are overlaid.

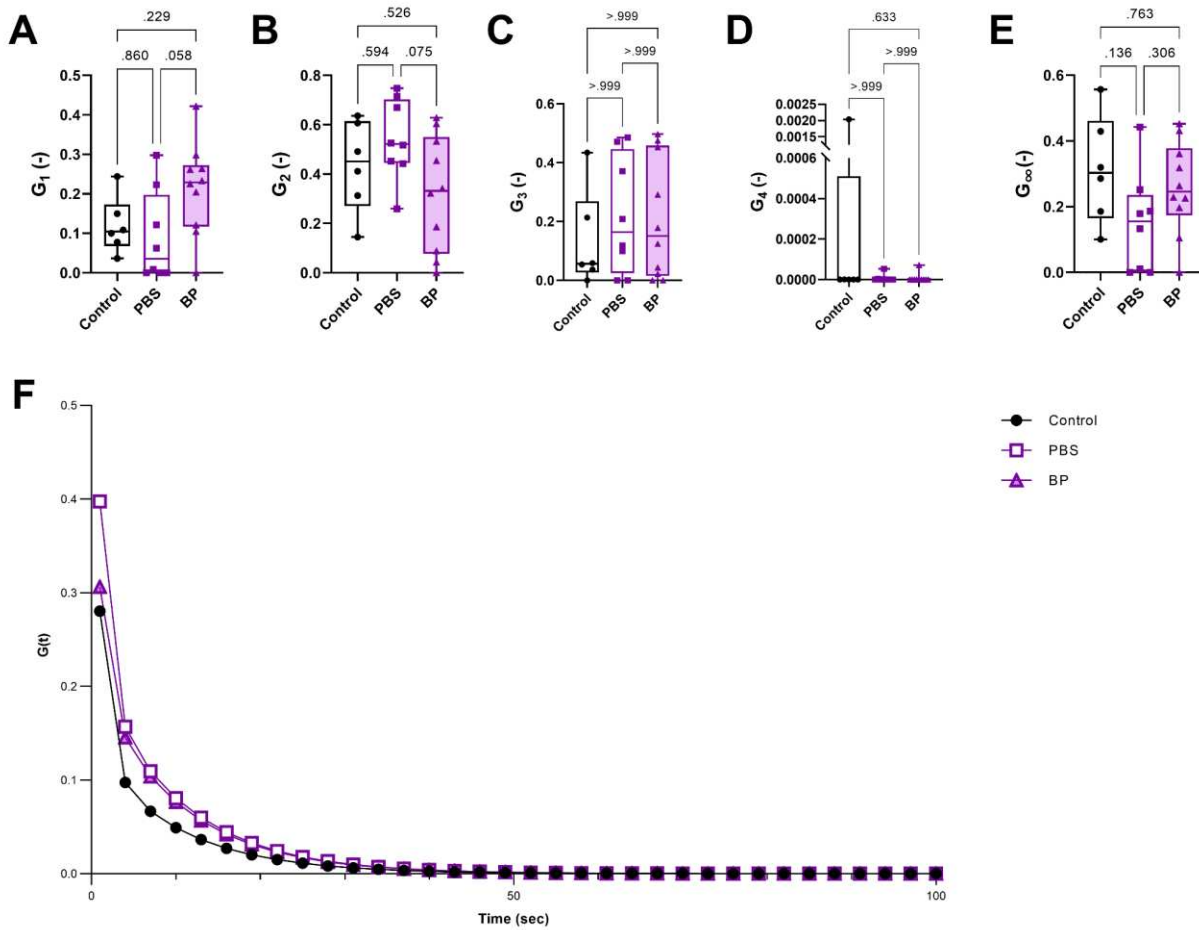


Figure 29. Viscoelastic fitting results. (A) The BP group exhibited increased G_1 term values as compared to the PBS group ($p=0.058$) and the Control group ($p=0.229$). (B) The BP group demonstrated decreased G_2 term values as compared to the PBS group ($p=0.075$) and the Control group ($p=0.526$). (C) The BP group displayed similar G_3 term values as the PBS group ($p>0.999$) and the Control group ($p>0.999$). (D) The BP group exhibited similar G_4 term values as the PBS group ($p>0.999$) and the Control group ($p=0.633$). (E) The PBS group demonstrated decreased G_∞ term values as compared to the Control group ($p=0.136$) and the BP group ($p=0.306$). (F) Mean reduced relaxation modulus function for each group is plotted against time. Symbols indicate group means and solid lines connect adjacent points. Points graphed 1 every 3 seconds. Differences in the short-term relaxation behavior is evident between the Control and OP groups. Statistical test: one-way ANOVA with Tukey's post hoc test (A,B,E) and Kruskal-Wallis test (C,D). Box plot indicates median and interquartile range; whiskers indicate maximum and minimum values. Individual datum points are overlaid.

Correlation Analysis

Statistically significant correlations were observed between the tendon biomechanical properties and bone microstructure. Moderate correlations were noted between the hyperelastic μ term and the bone volume fraction ($r = 0.470$, $p=0.020$), trabecular number ($r = 0.455$, $p=0.026$), trabecular spacing ($r = -0.460$, $p=0.024$), connectivity density ($r = 0.524$, $p=0.009$), and structure model index ($r = -0.468$, $p=0.021$, Table 7). Fair correlations were noted between the hyperelastic μ term and the trabecular thickness ($r = 0.354$, $p=0.090$), specific bone surface ($r = -0.354$, $p=0.090$), and degree of anisotropy ($r = 0.383$, $p=0.065$, Table 7). Moderate correlations were noted between the non-linearity term (α) and the bone volume fraction ($r = -0.517$, $p=0.010$), trabecular number ($r = -0.456$, $p=0.025$), trabecular thickness ($r = -0.517$, $p=0.010$), trabecular spacing ($r = 0.465$, $p=0.022$), specific bone surface ($r = 0.517$, $p=0.010$), connectivity density ($r = -0.528$, $p=0.008$), and structure model index ($r = 0.569$, $p=0.004$, Table 7). Fair correlations were noted between the non-linearity (α) and the degree of anisotropy ($r = -0.371$, $p = 0.074$, Table 7). Correlation plots are included in below (Figure 30).

Table 7. Spearman correlation values for Ogden hyperelastic coefficients with other outcome parameters.

	$\mu(\text{MPa})$		$\alpha (-)$		Bonar Score	
	r	p	r	p	r	p
BV/TV (-)	0.470	0.020	-0.517	0.010	-0.184	0.389
Tb.N (1/mm)	0.455	0.026	-0.456	0.025	-0.148	0.491
Tb.Th (mm)	0.354	0.090	-0.517	0.010	-0.375	0.071
Tb.Sp (mm)	-0.460	0.024	0.465	0.022	0.168	0.433
BS/BV (mm²/mm³)	-0.354	0.090	0.517	0.010	0.375	0.071
Conn.D (1/mm³)	0.524	0.009	-0.528	0.008	-0.083	0.701
SMI (-)	-0.468	0.021	0.569	0.004	0.070	0.744
DA (-)	0.383	0.065	-0.371	0.074	0.318	0.130
CSA (mm²)	-0.437	0.033	0.191	0.371	-0.133	0.536
Bonar Score (-)	0.087	0.687	-0.080	0.712	-	-
Percent Organized Collagen (%)	0.037	0.865	0.059	0.784	0.157	0.463
Percent Adipose Area (%)	-0.250	0.240	0.423	0.040	0.202	0.345

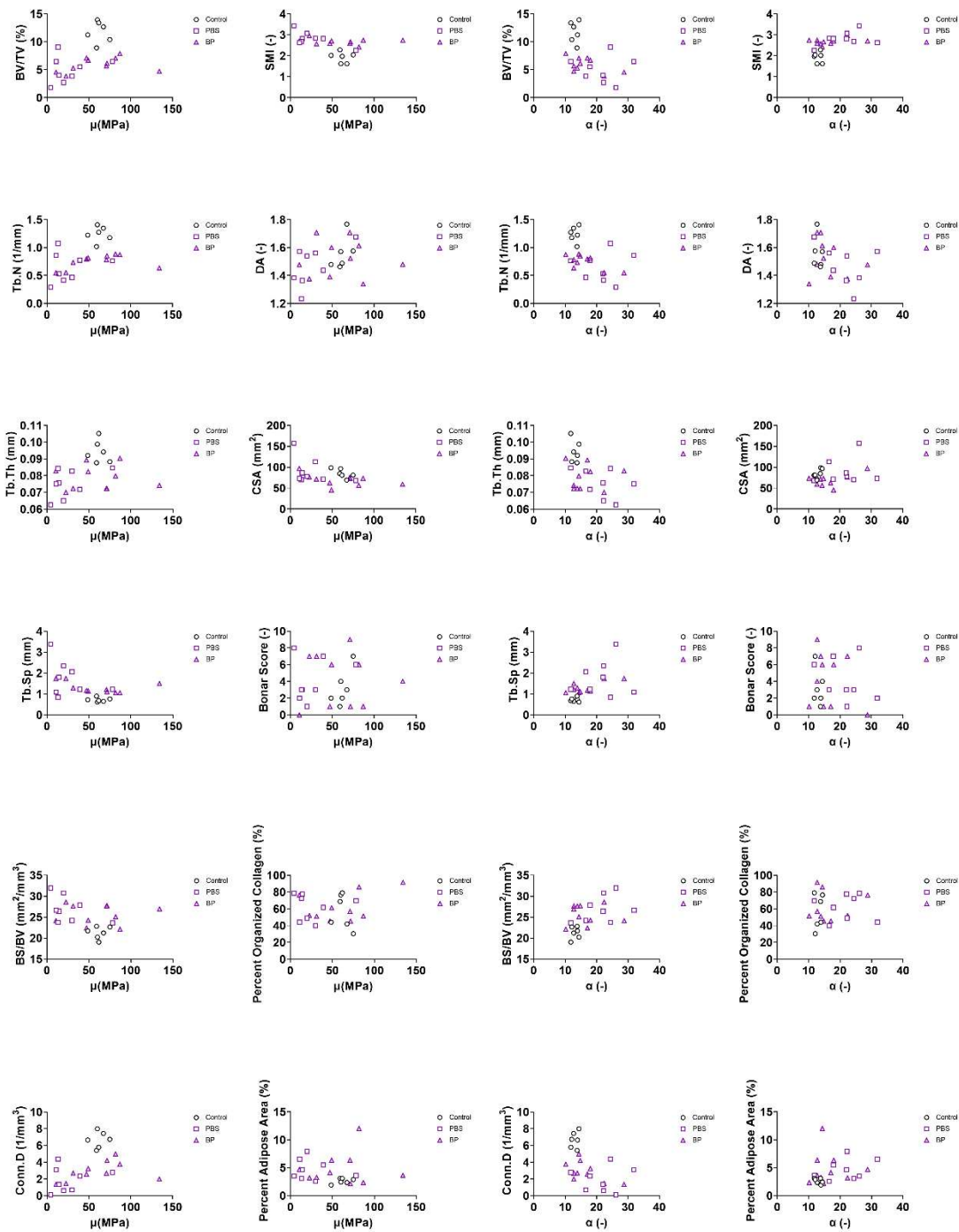


Figure 30. Correlation plots for Ogden hyperelastic terms and other outcome parameters. Spearman correlation values and p-values are listed in Table 1.

Discussion

The primary goal of this study was to assess the changes to the biomechanical and histopathological properties to tendon tissue that occur secondary to an induced osteoporotic state in a large animal model. A secondary objective was to evaluate whether bisphosphonate may impact any changes to tendon tissue in those same osteoporotic samples. These goals were pursued as a means to help elucidate the underlying mechanisms resulting in the increased rotator cuff repair failures in patients with OP. To this end, an ovine model was utilized to explore the changes to the IFT and relate them to the bone microstructure underlying the IFT insertion. These data presented in this work confirm our hypothesis and highlight some of the changes to soft tissue mechanics and pathology that occurred in the large animal OP model.

The comprehensive biomechanical testing and the subsequent hyperelastic and viscoelastic characterization detailed here illustrate the alterations to the biomechanical properties of the tendons. The PBS group (i.e., sham OP group) exhibited decreased Young's moduli, whereas the BP group exhibited similar moduli to the Control group. Additionally, the hyperelastic parameters used to calculate the Young's moduli were moderately and significantly correlated with the bone volume fraction, as well as most of the other trabecular structure outcome parameters. It is well known that collagen is the primary load-carrying component of tendons; thus, the aforementioned changes in tendon biomechanical behavior indicates that the collagen and/or extracellular matrix network in the PBS tendons was most likely altered. Interestingly, little to no changes were noted in quantitative or semi-quantitative assessment of collagen organization within the samples studied

here. Similarly, semi-quantitative analysis of the pathological characteristics typically seen in degenerative tendons revealed little to no differences between groups.

The changes to the Young's moduli values revealed physiologically important differences in tissue function/mechanics. While not reaching the level of statistical significance, the Young's modulus exhibited by the PBS group was markedly reduced as compared to the Control group across the entire experimentally tested range. While the non-destructive biomechanical testing employed in this study does not provide insight on failure loads, it is clear that a reduction in tendon moduli without change in CSA would result in a decreased ability to absorb energy under equivalent displacement/stretch applications, which would hamper the ability of the tendon to withstand traumatic loading, most likely leading to increased failure rates. As such, the differences in tendon moduli noted between groups potentially explains one component of the clinical presence of increased tears and decreased surgical outcomes in patients with OP. Additionally, the significant difference between tendon moduli in the BP group as compared to the PBS group suggests BPs have potential to positively impact soft tissue functional mechanics.

Inspection of the ovine tendon insertions revealed decreases in tidemark prominence and symmetry in the PBS group, whereas this change was less pronounced in the BP group. Additionally, cellularity in the fibrocartilaginous insertion was notably decreased in the PBS group, whereas the BP group exhibited increased mesenchymal cell populations, as compared to the Control group. Furthermore, differences in the insertional microstructure were noted between

the OP samples and the Control group. Specifically, the PBS and BP groups exhibited increased interdigitation of the bone to MFC junction, illustrating the impact of bone remodeling/loss on the tendon insertional structure. This, in combination with the loss of tinctorial distinction between the MFC and nMFC zones could represent either direct effect or a cascade of adaptive changes to the biomaterial interface of these mechanically disparate materials. Loss or disruption of gradient transition is thought to contribute to repetition of tendon tears and continued degeneration of the tendon⁽¹⁵⁴⁾. As such, the changes to tendon insertional structure described here may potentially be contributing to the increased prevalence of rotator cuff tears in patients with lower BMD⁽¹⁴⁵⁾.

Alterations to enthesis structure have previously been documented in osteoporotic tendon insertions by Cadet et al⁽¹⁴⁷⁾ in a rat model of OP. These changes were described as poorer fibrocartilage organization and an amorphous transition of the tendon insertion. Chen et al. reported a thinning to the tendon-bone interface and a loss of tidemark visibility in an OP model using lapine samples⁽¹⁴⁶⁾. Additionally, they described decreased cellular deposition in the enthesis area of their OVX samples. While these studies agree with our findings, this work is the first to illustrate the increased interdigitation of the bone to MFC junction, specifically.

The increased necessity for revision surgeries in OP patients is well documented in clinical studies^(52-54,143-145). Researchers have also demonstrated decreased failure stresses in OP small animal models previously. Chen et al. reported a 21.9% decrease in failure stress in a lapin model of OP⁽¹⁴⁶⁾. Cadet et al. also revealed a 4% decrease in tendon failure stress in a rat model of OP, with improvements in a group treated with BP⁽¹⁴⁷⁾. These studies have essentially confirmed what has been noted clinically, in that patients with OP have increased rates of tendon failures.

The justification for this work was further bolstered by the increased rate of RCR failures in OP patients. Bone loss at tendon and ligament insertions has been noted following disruption of the connective tissue and the resulting loss in loading to the local bone⁽¹⁵⁷⁾. Several researchers have hypothesized that this loss of bone is a contributing factor to the increased RCR failure rates. As such, several preclinical studies have documented improved failure loads of transected and repaired tendons as a result of various bisphosphonates and OP therapeutics (i.e., zoledronate, alendronate, SERMs, and sclerostin antibodies)⁽¹⁵⁷⁻¹⁶¹⁾. While these studies have demonstrated improved bone quality and tendon failure strength following RCR in treated samples, the destructive testing implemented in the previous studies has precluded the ability to determine whether mechanical changes are isolated to the bone-tendon interface, or whether the entire tendon is affected as well. Our work has highlighted the large impact on soft tissue biomechanical properties secondary to OP and treatment with anti-resorption therapies.

Our data has shown that BP treatments may have a restorative effect on the soft tissue biomechanical properties of tendons. It is also known that the use of bisphosphonate treatments can improve bone quality of bone within the humerus⁽¹⁴⁷⁾; however, it has been shown that improvements in bone quality do not impact the prevalence of rotator cuff repair failures in humans clinically⁽⁵²⁾. Taken together, it is clear that restoring the tendon biomechanical properties or the bone quantity are not sufficient to reduce the surgical failure of rotator cuff repair surgeries. We believe our findings showing the alterations to enthesis structure in both the PBS and BP treatment

groups may be the underlying mechanism for decreases prognosis for rotator cuff repair in patients with OP.

Previous research has revealed that BP interacts with fibroblast physiology. Specifically, BP treatments are designed to decrease the production of RANK-L and increase the production of IL-6⁽¹⁶²⁾, which are both produced by fibroblasts⁽¹⁶³⁾. While this produces a microenvironment that favors the inhibition of bone resorption, it has been shown to increase the proliferative capacity of fibroblasts⁽¹⁶⁴⁾. Furthermore, it has also been shown that Zolendronate (a potent and long-acting bisphosphonate in clinical use) can increase the elastin expression of fibroblasts⁽¹⁶⁴⁾. While elastin content was not measured in our study, we hypothesize that the inadvertent increases in elastin expression by the resident fibroblasts within the tendons may be a potential factor explaining the improved biomechanical properties of the BP tendons measured in this study.

This study has several limitations. Firstly, it was performed utilizing an animal model of osteoporosis which likely does not recapitulate all of the changes observed during the natural progress / onset of OP. However, we believe these data are relevant and provide insight into the mechanisms underlying the increased rotator cuff repair failures witnessed in OP patients. Secondly, the model used to induce OP in the sheep utilized several corticosteroid injections in conjunction with a vitamin D deficient diet, which have potential to impact tendon physiology. With respect to corticosteroid injections, studies have shown that steroid use can temporarily affect soft tissues such as tendon⁽¹⁶⁵⁾, with data revealing increases in tendon modulus following steroid

use⁽¹⁶⁶⁾. In contrast, these data indicate a decrease in tendon stiffness, which when taken together with the 19-week period between steroid injection and mechanical testing, lend credence to the belief that the steroid injections did not have a large impact on tendon mechanics. With respect to the impact of the vitamin D deficient diet, previous studies have revealed vitamin D impacts tendon healing through downregulation of MMP9⁽¹⁶⁷⁾. The primary finding of these studies was by means of increased production of MMP9 through the NF- κ B pathway, decreased healing outcomes and decreased collagen organization were realized following tendon injury⁽¹⁶⁸⁾. While these studies have exposed deleterious effects to tendon healing as a result of vitamin D deficiency, no impact on healthy tendons has been described. Additionally, expression of MMP-9 in uninjured tendons is relatively low as compared to the injured state⁽⁴⁶⁾, theoretically minimizing the impact of vitamin D deficiency on tendon physiology. As such, results presented herein should be interpreted in conjunction with the knowledge of the existence of these confounding factors. Finally, it is known that hormone levels can impact soft tissue mechanics^(169,170). Unfortunately, hormone levels were not monitored in this study, therefore data on such was unavailable and should be considered in future work.

Conclusions

These data confirm our hypothesis that the biomechanical properties and insertional structure of the infraspinatus tendon are altered in an ovine model of osteoporosis. It is our belief that the changes to the insertional structure play a role in the increased surgical failures noted in patients with OP. Therefore, there is a critical need for future work aimed at improving and restoring the native gradient within the fibrocartilaginous insertion as a means to improve surgical outcomes.

Interestingly, the samples treated with bisphosphonate injections exhibited biomechanical properties akin to the Control samples. While we were unable to measure the physiological reasons for this, it is our hypothesis that BP is inadvertently impacting the resident fibroblasts of the tendons, potentially resulting in increased elastin expression. Future work investigating the impact of BP on tendon fibroblasts is therefore warranted.

Chapter 6- Form and Function: Biomechanical, Pathological, and Gene Expression Changes Secondary to Aging In The Human Rotator Cuff

Introduction

Previous studies have shown a high prevalence of rotator cuff tendon tears in the general population, with tear rates increasing markedly with age ^(15,171). Considering these rotator cuff repair (RCR) failure rates have been documented to be as high as 90% depending on risk factors ⁽¹⁷⁾, there is a clear need to develop new therapeutics and treatment devices that can drive improved healing outcomes. Recent research has been aimed at utilizing scaffolds to either drive improved time zero repair strength or to deliver biologically active agents ⁽⁶⁹⁾; however, many products have not generated the anticipated clinical success ⁽¹⁷²⁻¹⁷⁴⁾.

Recent work has illustrated the importance of proper mechanobiological cues to resident cell populations to maintain healthy tissue homeostasis, collagen turnover, and gene expression ⁽¹⁷⁵⁻¹⁷⁹⁾; this concept has been further exemplified through utilization of overuse tendinopathy models that have shown breakdowns in tendon collagen structure and inferior mechanical properties secondary to overuse regiments in rats ^(180,181). With this in mind, it is apparent that tailored scaffold mechanical properties have the potential to positively impact native tenocyte function and behavior. Unfortunately, current biomechanical property targets for human rotator cuff tendons suitable for design of such a scaffold have not yet been reported.

Furthermore, it has been documented that each tendon has unique biomechanical properties as a result of anatomical arrangement and function ⁽¹⁸²⁻¹⁸⁴⁾. Clinical studies have revealed the vast majority of tears occur to the supraspinatus tendons ^(171,185), yet the underlying reason is not understood. Additionally, the negative impact of chronic degeneration on RCR success rates has been well documented ⁽¹⁸⁶⁾, yet the exact cause for chronic degeneration pathology and at what point those changes manifest has not yet been fully elucidated. Furthermore, an additional contraindication for RCR is age ⁽¹⁸⁷⁾, which has been shown to impact tendon biomechanical properties, yet the underlying mechanism is not clear. While some researchers have documented age-related changes to tendon biomechanical properties in animal models, changes to all four rotator cuff tendons in humans secondary to aging have not yet been documented. Likewise, it is unclear to what extent biomechanical changes to these tendons occur with differing levels of degenerative pathology and gene expression.

With this in mind, the goal of this study was to characterize the biomechanical and histopathological properties with the accompanying gene expression of fresh human rotator cuff tendons. Additionally, the biomechanical properties of these tendons were to be modeled using a one-term Ogden quasilinear viscoelastic constitutive theory as a means of providing the necessary material properties to better understand the mechanobiological environment of healthy and degenerated rotator cuff tendons. It was hypothesized that aged human tendons would exhibit increased degenerative pathological characteristics and decreased biomechanical properties.

Materials and Methods

All samples included within this manuscript were de-identified cadaveric tissues. As such, the Colorado State University Institutional Review Board (IRB) deemed approval was unnecessary.

Tendon Dissection Procedure

Paired shoulders were obtained within 16-hours postmortem delivered on wet ice. Samples were immediately dissected with great care to ensure tendon integrity. Three histological muscle biopsies were harvested from each rotator cuff muscle group (i.e., supraspinatus, infraspinatus, subscapularis, and teres minor) prior to exposure of the tendons. Biopsies were taken from the central muscle belly. Upon visualization and isolation of each rotator cuff tendon, a small (i.e., 2mm wide x 4mm long) tendon biopsy was taken with a sterile blade and flash frozen in liquid nitrogen for the purpose of RNA sequencing. Following exposure of each tendon/muscle group and skeletonization of the humerus, the muscle tissue was carefully removed from each tendon.

Tendon Biomechanical Testing Procedures

Similar to previous studies^(136,188), a strong two-part hard casting resin (SmoothCast 321, Smooth-On, Macungie, PA) was used to mount the humeri in a polyvinyl chloride sleeve. This sleeve was installed in a custom fixture to ensure tendon testing occurred in anatomically appropriate directions on the servo-hydraulic load frame (Model 858, MTS Corp. Eden Prairie, MN). The tendons were gripped using a custom cryo-grip maintained between -10°C and -15°C to minimize

freeze artifact while ensuring adequate gripping strength ⁽¹³⁶⁾. High-speed video was captured for all testing to ensure tendons did not slip within the grips. Tendons remained unloaded for a period of at least one hour prior to biomechanical testing to provide for viscoelastic equilibrium ^(68,117-121). Prior to initiation of biomechanical testing, a static preload of 5N was applied to each tendon for a duration of two minutes, at which point a reference gage length was measured and recorded for purposes of strain application. Tendons were then subjected to two stress relaxation tests at 6% and 8% global stretch. Subsequently, two cyclic tests at decadal frequencies (i.e., 1 Hz and 0.1 Hz) at 10% global stretch were applied randomly. A 1,000 second rest period was enforced between tests to minimize the viscoelastic history of previous test cycles ⁽¹²⁰⁾. Force and displacement data were sampled at 100 Hz for all testing. Tendon hydration was preserved with physiological saline spray at all times during dissection and testing. The stress relaxation tests at both stretch magnitudes were subsequently analyzed to generate the following outcome parameters: peak force, peak stress, and percent relaxation. Following biomechanical testing, each tendon was transected from the humerus at the insertion. Photogrammetry techniques were utilized to measure the cross-sectional area (CSA) of each tendon for the purposes of transforming force to stress ^(121,155).

Viscoelastic Modeling

Similar to previous studies ⁽²⁸⁻³⁰⁾, a quasilinear viscoelastic (QLV) strain energy function was implemented as a means to generate biomechanical material property constants capable of predicting tissue response to arbitrary strain inputs *in silico*. As proposed by Fung ⁽³¹⁾, soft tissue response (i.e., induced stress) to uniaxial loading can be modeled by:

$$\sigma[\varepsilon(t), t] = \int_0^t G(t - \tau) \frac{d\sigma^e(\varepsilon)}{d\varepsilon} \frac{d\varepsilon(\tau)}{d\tau} d\tau,$$

Equation 10

where $\varepsilon(t)$ denotes the engineering strain applied to the tissue, $G(t)$ denotes the reduced relaxation modulus (capturing the viscous component of tissue response), and $\sigma^e(\varepsilon)$ denotes the non-linear elastic behavior (capturing the instantaneous hyperelastic component of tissue response). Similar to previous studies ^(28,121), a Prony series was implemented to model the reduced relaxation modulus as follows:

$$G(t) = G_\infty + \sum_{i=1}^4 G_i e^{-t/\tau_i}.$$

Equation 11

To ensure unique solutions, the Prony series terms were subjected to the following constraints: all $G_i \geq 0$, $\sum_{i=1}^4 G_i = 1$, and $\tau_i = [0.1 \text{ sec}, 1 \text{ sec}, 10 \text{ sec}, 100 \text{ sec}]$ ⁽²⁸⁾. A 1-term Ogden strain energy function was implemented as a means of capturing the hyperelastic behavior of the tendons:

$$\sigma^e(\varepsilon) = \frac{2\mu}{\alpha} [(\varepsilon + 1)^{\alpha-1} - (\varepsilon + 1)^{-(\alpha/2)-1}].$$

Equation 12

In this formulation, μ and α are experimentally derived material constants that provide for the strain-dependent material stress ⁽²⁷⁾. By writing Eqn. 3 in terms of stretch then subsequently differentiating with respect to stretch (λ), the formulation of Young's Modulus as a function of stretch is obtained:

$$\frac{d\sigma}{d\lambda} = \frac{2\mu}{\alpha} \left[(\alpha - 1)\lambda^{(\alpha-2)} + \left(\frac{\alpha}{2 + 1} \right) \lambda^{-(0.5\alpha+2)} \right].$$

Equation 13

Implementation of this modeling approach as defined in Eqns. 1 – 3 resulted in a total of seven fitted terms: μ , α , G_1 , G_2 , G_3 , G_4 , and G_∞ . Cyclic biomechanical testing data for each sample were independently fit through implementation of Matlab's (R2020a, Mathworks, Natick, MA) *fmincon* function with the optimization goal of reducing root-mean-squared errors (RMSE) ⁽¹⁵⁵⁾. The fitted terms derived from both cyclic tests (i.e., 1 Hz, 0.1 Hz) were then averaged to generate one set of seven fitted terms for each specimen/tendon. To validate the model fitting results and ascertain their predictive capabilities, these parameters were utilized to predict the stress-relaxation responses. Specifically, the mean fitting parameters from each respective tendon/age group were utilized to predict the mean experimental stress-relaxation response of that same group. Predicted peak stress was compared to experimental peak stress and RMSE values were reported as outcome parameters for the predictive testing.

As a means of further visualizing the age-related changes to tendon biomechanical properties, Eqn. 4 was utilized to calculate the stretch-dependent Young's modulus values at discrete intervals (i.e., 1%) over the experimental stretch range (i.e., $1.00 \leq \lambda \leq 1.10$) for each tendon/age group.

Histomorphological Analysis

Following biomechanical testing, tendons were placed in 10% neutral buffered formalin for 24 hours then were processed using standard formalin fixed paraffin embedding procedures. Two 5 μm thick slides were produced from each specimen, with one slide stained with hematoxylin and eosin (H&E) and one slide stained with Picro-sirius red. Muscle biopsies were processed similarly; however, only one slide for each specimen was produced and stained with H&E.

Polarized light microscopy was utilized to image the picro-sirius red stained slides and assess collagen organization ⁽¹³⁶⁾. Briefly, tendon sections were imaged at 100x magnification using a polarized light scanning microscope with a manual exposure of 40ms (Olympus BX61VS, Center Valley, PA). A machine learning algorithm (Image-Pro Premier v9.2, RRID:SCR_007369) was utilized to quantify the percent area of the organized / disorganized collagen within the tendon section.

Presence of intramuscular adipose content has long been correlated with decreased RCR outcomes and increased degenerative tendon pathology ⁽¹⁵²⁾. As such, the intramuscular adipose content

within the rotator cuff muscle groups was quantified using histomorphometry techniques as previously outlined ⁽¹⁸⁸⁾, with the intention of documenting changes to tendon biomechanical properties at different stages of associated muscle fatty atrophy. Adipose area and total tissue area were quantified (Image-Pro Premier v9.2, RRID:SCR_007369). To normalize for differing section areas, percent intramuscular adipose area was calculated. The reported percent intramuscular adipose content value reported for each sample was the mean of three randomly located equally sized analysis regions within each specimen.

Histopathological analysis

The semi-quantitative Bonar scoring system has previously been implemented as a means of assessing the degenerative pathology of tendon samples ⁽⁴⁰⁾. Tendon slides stained with H&E were graded by a blinded veterinary pathologist in residency according to the previously defined Bonar tendinopathy scale ⁽¹⁸⁹⁾. Specifically, the tendon specimens were evaluated on a semi-quantitative scale from 0 (normal/healthy) to 3 (markedly degenerated) across four categories: (1) tenocyte reactivity, (2) angiogenesis, (3) tendon bundle organization and polarization, and (4) deposition of ground substance ⁽⁴⁰⁾. The summation of the four category scores was used to provide an overall score for each tendon ranging from 0 (pathologically normal) to 12 (pathologically degenerated). Following completion of semi-quantitative scoring, the pathologist was unblinded to specimen information (i.e., number and age) and made observational comments regarding structural and tissue component features to provide additional pathological descriptions and comparisons across tendon and age groups.

Gene Expression Analysis

Gene expression was probed in all tendon samples that met minimum RNA sequencing (RNAseq) standards (i.e., $\geq 0.4\mu\text{g}$, $\geq 20\text{ng}/\mu\text{L}$, $\text{RIN} \geq 6.8$) as a means of exploring changes secondary to aging and degeneration. RNA extractions were carried out using previously defined procedures (124,136,188). Tendon biopsies purposed for RNAseq analyses were powdered then lysed (TRizol™ Invitrogen, Carlsbad, CA, USA) to precipitate RNA. Chloroform was utilized to isolate RNA which was further purified using commercially available kits (RNeasy, Qiagen, Hilden, Germany). Changes secondary to aging and degree of pathological degeneration (as evidenced by Bonar scoring) were explored.

Statistical analysis

Cadavers were divided into two groups: younger (less than 36 years old) and aged (greater than 55 years old). Statistical comparisons within tendon groups between age groups were made using a Welch's t-test (GraphPad Prism v9.2.0, GraphPad Software, San Diego, CA). An Extra Sum-of-Squares F Test was performed on all Young's modulus vs stretch plots to determine if one curve could adequately fit all data. A significance threshold (α) of 0.05 was used for all statistical comparisons. Sample numbers for each grouping are outlined in **Table 1**. Sample sizes were verified as adequate as demonstrated by a post-*hoc* power test based on biomechanical properties of the tendons (infraspinus hyperelastic μ , power = 0.913). Correlations between all outcome parameters were assessed to illuminate patterns between pathological features, gene expression,

and biomechanical properties; Pearson correlation coefficients and associated P-values were reported. Correlation strength was characterized as follows: slight (0 to .2), fair (.21 to .4), moderate (.41 to .6), strong (.61 to .8), and very strong (.81 to 1.0) ⁽¹⁵⁶⁾.

Table 8. Sample sizes.

Tendon	Age Group	Mechanics	Histology	RNAseq
Supraspinatus	Younger	4	4	1
	Aged	3	7	5
Infraspinatus	Younger	4	4	0
	Aged	6	8	2
Subscapularis	Younger	4	4	1
	Aged	5	7	3
Teres Minor	Younger	3	4	0
	Aged	5	8	0

Results

Tendon Biomechanical Testing

The rotator cuff tendons exhibited differentially altered biomechanical properties with age. All aged tendons exhibited decreased peak stress at both stretch magnitudes (i.e., 6% and 8%), and increased percent relaxation. Specifically, the aged supraspinatus tendons exhibited a 67.3% (p=0.078, Suppl. Mat. Fig1A) and 65.6% (p=0.106, Suppl. Mat. Fig 1B) decrease in peak stress as compared to the younger tendons at the 6% and 8% stretch levels, respectively. Similarly, the aged

infraspinatus tendons demonstrated a 48.8% (p=0.007, Suppl. Mat. Fig1A) and 52.6% (p=0.001, Suppl. Mat. Fig 1B) decrease in peak stress as compared to the younger tendons at the 6% and 8% stretch levels, respectively. The aged subscapularis exhibited a 47.8% (p=0.002, Suppl. Mat. Fig1A) and 44.6% (p=0.012, Suppl. Mat. Fig 1B) decrease in peak stress as compared to the younger tendons at the 6% and 8% stretch levels, respectively. The aged teres minor tendons demonstrated a 29.7% (p=0.223, Suppl. Mat. Fig1A) and 25.6% (p=0.289, Suppl. Mat. Fig 1B) decrease in peak stress as compared to the younger tendons at the 6% and 8% stretch levels, respectively.

Differences in the percent relaxation outcome metric were not as pronounced for the supraspinatus and teres minor tendons as compared to the infraspinatus and subscapularis tendons. The aged supraspinatus tendons exhibited a 4.0% (p=0.821, Suppl. Mat. Fig 1C) and 14.5% (p=0.635, Suppl. Mat. Fig 1D) relative increase in percent relaxation as compared to the younger tendons at the 6% and 8% stretch levels, respectively. Similarly, the aged infraspinatus tendons demonstrated a 32.9% (p=0.005, Suppl. Mat. Fig 1C) and 22.4% (p=0.072, Suppl. Mat. Fig 1D) relative increase in percent relaxation as compared to the younger tendons at the 6% and 8% stretch levels, respectively. The aged subscapularis exhibited a 22.1% (p=0.056, Suppl. Mat. Fig 1C) and 23.5% (p=0.049, Suppl. Mat. Fig 1D) relative increase in percent relaxation as compared to the younger tendons at the 6% and 8% stretch levels, respectively. The aged and younger teres minor tendons exhibited similar percent relaxation values at both stretch magnitudes. The aged and younger tendons did not exhibit physiologically relevant differences in cross-sectional area (all p>0.249).

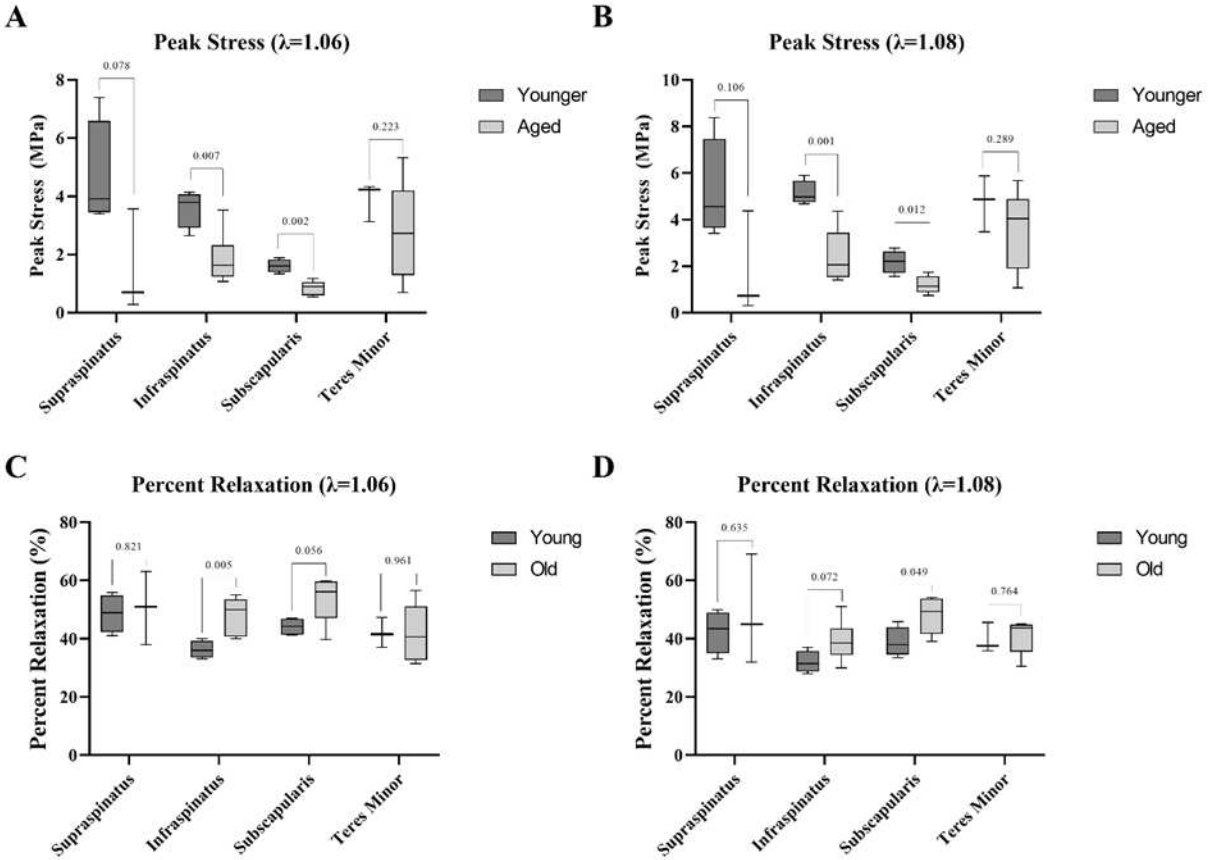


Figure 31. Stress-relaxation testing results. A) Peak stress ($\lambda=1.06$). The aged infraspinatus and subscapularis samples exhibited significantly decreased peak stress as compared to their respective younger age group samples. B) Peak stress ($\lambda=1.08$). The aged infraspinatus and subscapularis samples exhibited significantly decreased peak stress as compared to their respective younger age group samples. C) Percent relaxation ($\lambda=1.06$). The aged infraspinatus samples exhibited significantly increased percent relaxation as compared to the younger infraspinatus samples. D) Percent relaxation ($\lambda=1.08$). The aged subscapularis samples demonstrated significantly increased percent relaxation as compared to the younger subscapularis samples. Statistical test: Welch's t-test. Box plot indicates median and interquartile range; whiskers indicate maximum and minimum values.

Viscoelastic Modeling

Viscoelastic modeling was completed successfully for all samples, with RMSE of 0.090 ± 0.057 MPa (mean \pm std. dev.). The aged supraspinatus, infraspinatus, and subscapularis tendons

exhibited marked decreases in the Ogden μ term, whereas the teres minor did not exhibit a change. Specifically, viscoelastic modeling revealed a 69.6% ($p=0.076$), 60.3% ($p=0.037$), and 54.4% ($p=0.031$, Suppl. Mat. Fig 1A) decrease in the Ogden μ term in the aged tendons as compared to the younger tendons for the supraspinatus, infraspinatus, and subscapularis tendons, respectively. These tendons also exhibited increases in the Ogden α term, with increases of 17.7% ($p=0.400$), 17.0% ($p=0.060$), and 22.8% ($p=0.026$, Suppl. Mat. Fig 1B) in the aged tendons as compared to the younger tendons for the supraspinatus, infraspinatus, and subscapularis tendons, respectively. Using Eqn. 4, the Young's modulus was calculated across the experimentally tested stretch range (i.e., 1.00 – 1.10). Each of the experimental groups (i.e., younger and aged groups for all four tendons) were plotted and a nonlinear fit was assigned to the means of each group (Fig 1). The Extra Sum-of-Squares F Tests revealed significant differences in curve shapes in all four tendons between the aged and younger groups ($p<0.0001$). As evidenced by these plots, the aged and younger tendon moduli values increasingly diverged with increased stretch magnitude in all four tendons. This divergence was probed by comparing moduli values between the younger and aged groups of all four tendons at two percent discrete stretch magnitudes (i.e., 1.00, 1.02, 1.04... 1.10) using Welch's t-tests to ascertain significant differences (Suppl. Mat. Fig 3). The aged supraspinatus tendons exhibited significantly reduced Young's modulus for all $\lambda \geq 1.04$ ($\lambda = 1.04$, $p=0.045$; $\lambda = 1.06$, $p=0.033$; $\lambda = 1.08$, $p=0.025$; $\lambda = 1.10$, $p=0.022$). The aged infraspinatus tendons exhibited significantly reduced Young's modulus across all experimentally tested stretch magnitudes ($\lambda = 1.00$, $p=0.036$; $\lambda = 1.02$, $p=0.031$; $\lambda = 1.04$, $p=0.026$; $\lambda = 1.06$, $p=0.020$; $\lambda = 1.08$, $p=0.014$; $\lambda = 1.10$, $p=0.010$). The aged subscapularis tendons demonstrated significantly reduced Young's modulus for $1.00 \leq \lambda \leq 1.04$ ($\lambda = 1.00$, $p=0.030$; $\lambda = 1.02$, $p=0.032$; $\lambda = 1.04$, $p=0.040$). There were no significant differences between the younger and aged teres minor tendons at any

stretch magnitude. The best-fit values are included in Suppl. Mat. Table 1. Grossly, few significant changes to the Prony series terms representing the reduced relaxation modulus of the aged tendons were noted (Suppl. Mat. Fig 4A-E). The changes to the reduced relaxation moduli in the aged group as compared to the younger group for each tendon were not consistent (Fig 2A-D).

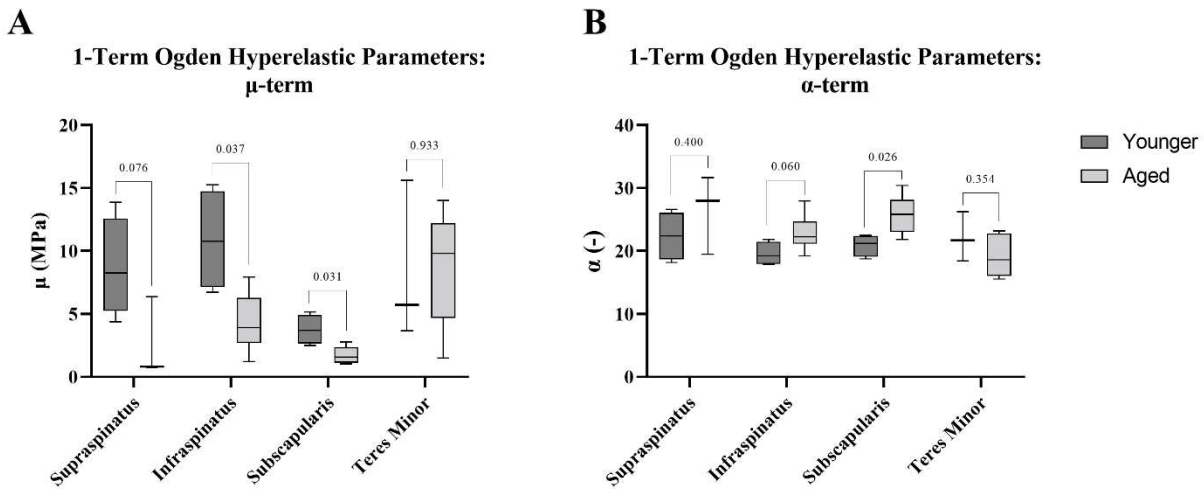


Figure 32. One-term Ogden hyperelastic modeling parameters. A) Ogden μ -term. The aged infraspinatus and subscapularis samples exhibited significantly decreased μ -term values as compared to their respective younger samples. B) Ogden α -term. The aged subscapularis samples exhibited significantly increase α -term values as compared to the younger subscapularis samples. Statistical test: Welch's t-test. Box plot indicates median and interquartile range; whiskers indicate maximum and minimum values.

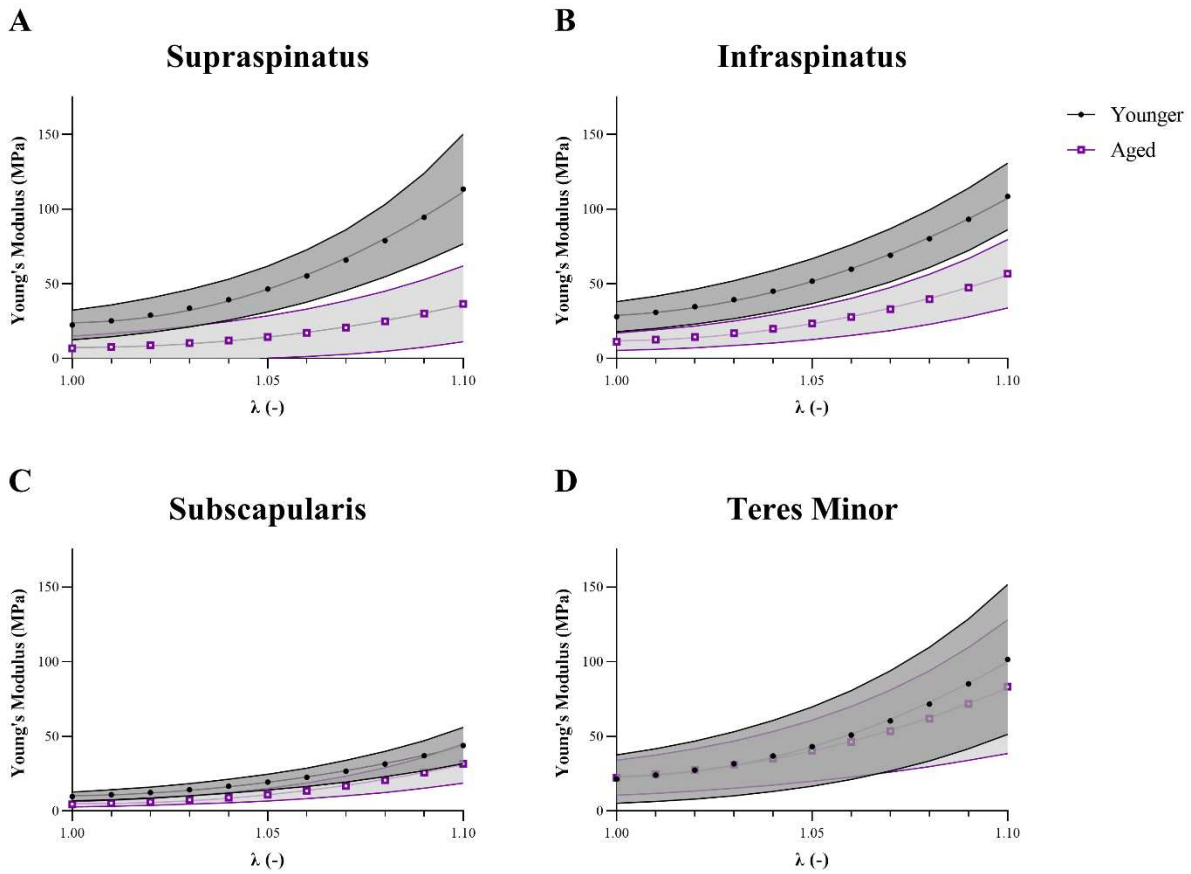


Figure 33. Young's modulus vs Stretch plots. A) Aged and Younger Supraspinatus fits. B) Aged and Younger Infraspinatus fits. C) Aged and Younger Subscapularis fits. D) Aged and Younger Teres Minor fits. Extra Sum-of-Squares F Tests were performed between aged and younger groups for each tendon to confirm separate fits should be performed for each age group (all $p < 0.0001$). Shaded regions illustrate ± 1 standard deviation from respective group means.

Table 9. Best-fit values for Young's modulus vs. stretch curves for all age groups and tendons.

Tendon	Age Group	Tenocytes	Ground Substance	Collagen	Vascularity
Supraspinatus	Younger	0.77 ± 0.60	0.46 ± 0.66	1.00 ± 0.58	1.08 ± 0.95
	Aged	1.64 ± 1.04	0.96 ± 1.14	1.60 ± 1.04	1.68 ± 1.18
Infraspinatus	Younger	0.85 ± 0.55	0.31 ± 0.48	1.15 ± 0.55	1.08 ± 0.95
	Aged	1.62 ± 0.98	0.86 ± 1.09	1.59 ± 1.02	1.69 ± 1.20
Subscapularis	Younger	0.77 ± 0.60	0.31 ± 0.48	1.08 ± 0.64	1.08 ± 0.95
	Aged	1.60 ± 1.00	0.88 ± 1.13	1.56 ± 1.00	1.60 ± 1.15
Teres Minor	Younger	0.69 ± 0.48	0.46 ± 0.66	1.00 ± 0.58	0.92 ± 0.76
	Aged	1.63 ± 1.01	0.93 ± 1.11	1.70 ± 0.95	1.89 ± 1.15

Data are presented as means \pm std. dev.

As a means to quantify the robustness of biomechanical modeling efforts, the mean Ogden QLV parameters from each group generated from cyclic testing were used independently to predict the mean stress relaxation testing experimental results ($\lambda=1.08$) from their respective group. The experimental means were plotted with the accompanying predicted stress value for each tendon / age group (Fig 3A-H). To quantify the goodness of fit, RMSE values for the predictions were calculated. Additionally, normalized RMSE (N.RMSE) were calculated as RMSE/Peak Stress to provide a percent error in prediction of stress relaxation ramp phase (Table 10). Predicted values fell within one standard deviation of the experimental mean with RMSE of 0.22 ± 0.08 MPa and N.RMSE of $7.78 \pm 3.20\%$ (mean \pm std. dev.).

Table 10. Viscoelastic modeling prediction errors.

Tendon	Age Group	RMSE (0-1sec, MPa)	N.RMSE (0-1sec, %)
Supraspinatus	Younger	0.31	6.43
	Aged	0.24	13.78
Infraspinatus	Younger	0.22	4.58
	Aged	0.12	5.02
Subscapularis	Younger	0.13	6.24
	Aged	0.12	10.60
Teres Minor	Younger	0.27	6.11
	Aged	0.32	9.49

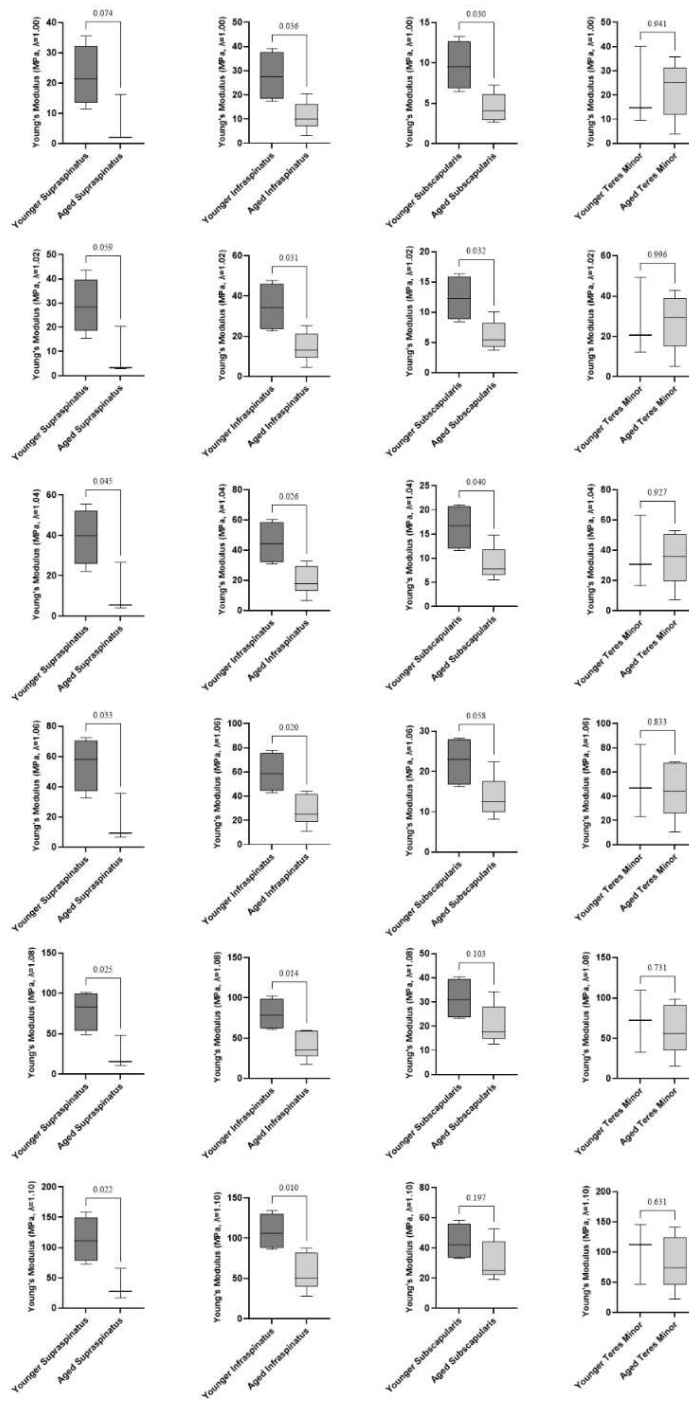


Figure 34. Young's modulus values for all groups at discrete stretch levels ($1.00 \leq \lambda \leq 1.10$). Statistical test: Welch's t-test. Box plot indicates median and interquartile range; whiskers indicate maximum and minimum values.

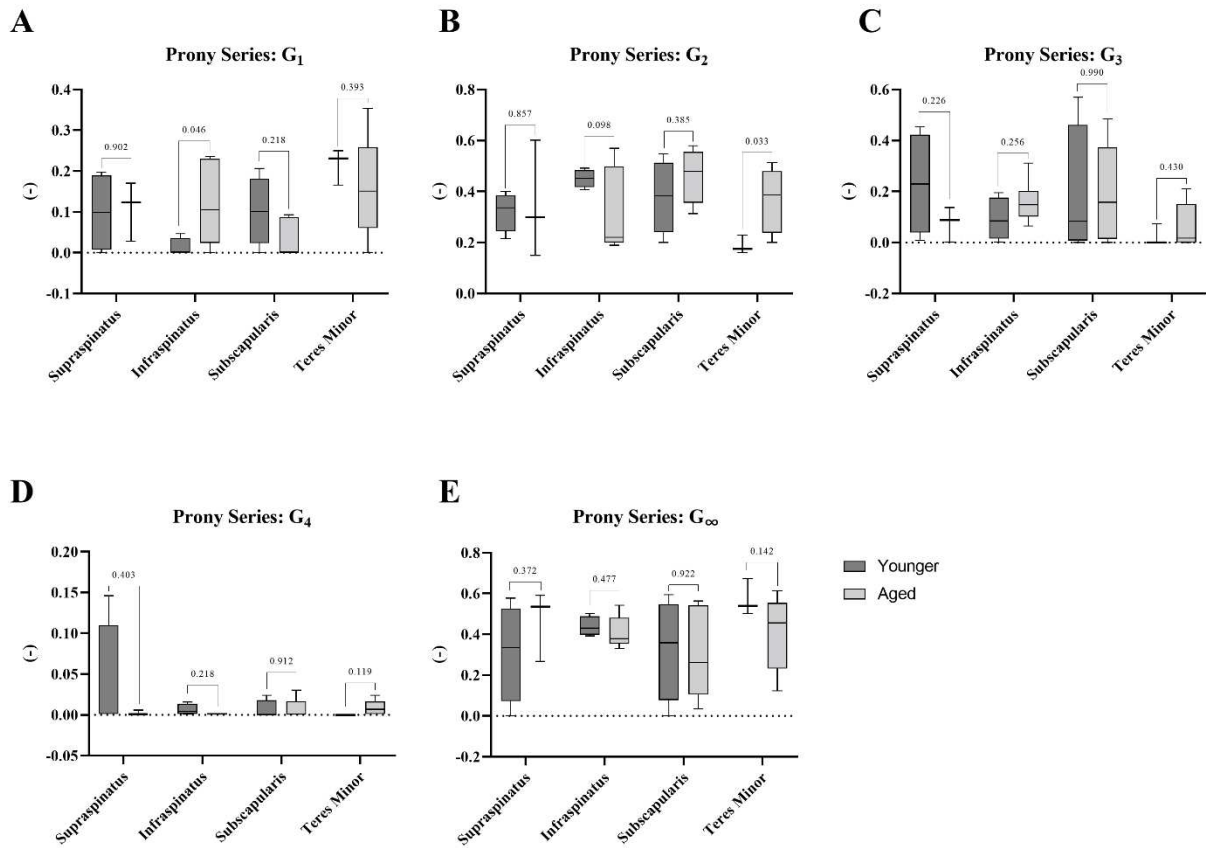


Figure 35. Prony series values representing the reduced relaxation moduli for all four tendons in the aged and younger groups. A) G_1 Prony term. The aged infraspinatus samples exhibited significantly increased G_1 values as compared to the younger infraspinatus samples. B) G_2 Prony term. The aged teres minor samples exhibited significantly increased G_2 values as compared to the younger teres minor samples. C) G_3 Prony term. No significant differences were noted between age groups in any tendons. D) G_4 Prony term. No significant differences were noted between age groups in any tendons. E) G_∞ Prony term. No significant differences were noted between age groups in any tendons. Statistical test: Welch's t-test. Box plot indicates median and interquartile range; whiskers indicate maximum and minimum values.

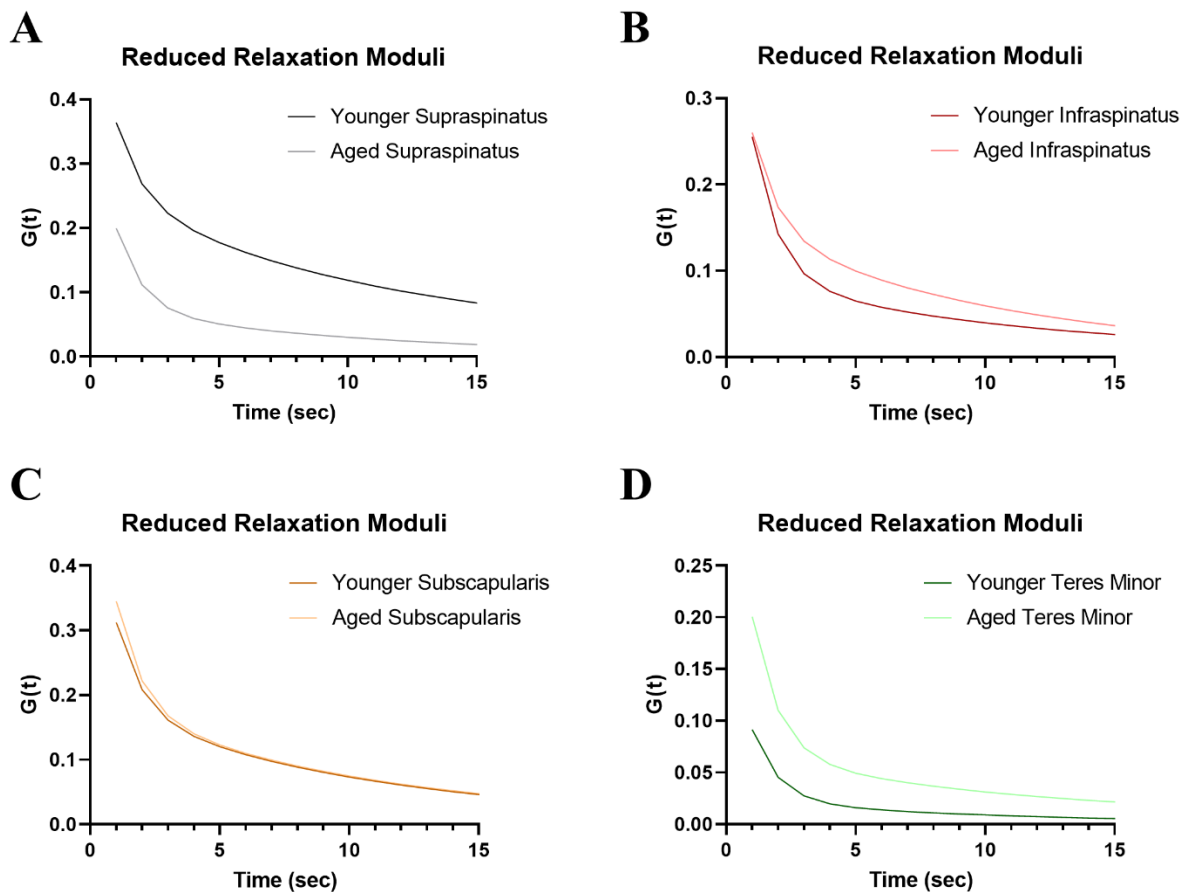


Figure 36. Reduced relaxation modulus vs. time plots. A) Aged and Younger Supraspinatus fits. B) Aged and Younger Infraspinatus fits. C) Aged and Younger Subscapularis fits. D) Aged and Younger Teres Minor fits.

Histomorphological assessment of collagen fiber alignment and intramuscular adipose content

Collagen organization was quantified within each tendon across both age groups through utilization of Picro Sirius red staining. No significant differences were noted in percent organized collagen between the aged and younger groups in any of the four tendons (Fig 4A). Intramuscular adipose

content as measured through histomorphometry techniques was markedly increased in the aged infraspinatus (828.2%, $p=0.043$) and teres minor (1,376.4%, $p=0.033$) muscle samples. No differences were noted in the intramuscular adipose content between the aged and younger groups in the supraspinatus ($p=0.688$) and subscapularis ($p=0.637$) groups (Fig 4B).

Histopathology Results

Typical degenerative pathological characteristics were semi-quantitatively assessed through Bonar scoring which revealed increased degenerative pathology in the aged tendons as compared to the younger tendons in the infraspinatus, subscapularis, and teres minor tendons. Specifically, the Bonar scores were increased by 180.6% ($p<0.001$), 237.1% ($p=0.067$), and 88.1% ($p=0.136$) in the aged infraspinatus, subscapularis, and teres minor tendons, respectively (Fig 4C). No differences were noted between the younger and aged supraspinatus tendon scores, with both groups exhibiting moderate characteristics of chronic degeneration (Fig 4C). As outlined previously, the overall Bonar score is generated by summing the scores of four different pathological categories (i.e., tenocytes, ground substance, collagen, and vascularity). The scores for all ages groups and tendons in each of these four categories are provided in Table 4. Individual category scores were increased in all four categories for all four tendons in the aged tendons as compared to the younger tendons. Increased tenocyte reactivity was noted in all aged tendons as compared to the younger tendons, with relative score increases of 113.0%, 90.6%, 107.8%, and 136.2% for the supraspinatus, infraspinatus, subscapularis, and teres minor tendons, respectively. Heightened deposition of ground substance was noted in all aged tendons as compared to the younger tendons, with relative score increases of 108.7%, 177.4%, 183.9%, and 102.2% for the

supraspinatus, infraspinatus, subscapularis, and teres minor tendons, respectively. Tendon bundle organization and polarization was decreased in all aged tendons, with relative score increases of 60.0%, 38.3%, 44.4%, and 70.0% for the supraspinatus, infraspinatus, subscapularis, and teres minor tendons, respectively. Increased vascularity was observed in all aged tendons, with relative score increases of 55.6%, 56.5%, 48.1%, and 105.4% for the supraspinatus, infraspinatus, subscapularis, and teres minor tendons, respectively.

Table 11. Categorical Bonar degeneration scoring results

Tendon	Age Group	Tenocytes	Ground Substance	Collagen	Vascularity
Supraspinatus	Younger	0.77 ± 0.60	0.46 ± 0.66	1.00 ± 0.58	1.08 ± 0.95
	Aged	1.64 ± 1.04	0.96 ± 1.14	1.60 ± 1.04	1.68 ± 1.18
Infraspinatus	Younger	0.85 ± 0.55	0.31 ± 0.48	1.15 ± 0.55	1.08 ± 0.95
	Aged	1.62 ± 0.98	0.86 ± 1.09	1.59 ± 1.02	1.69 ± 1.20
Subscapularis	Younger	0.77 ± 0.60	0.31 ± 0.48	1.08 ± 0.64	1.08 ± 0.95
	Aged	1.60 ± 1.00	0.88 ± 1.13	1.56 ± 1.00	1.60 ± 1.15
Teres Minor	Younger	0.69 ± 0.48	0.46 ± 0.66	1.00 ± 0.58	0.92 ± 0.76
	Aged	1.63 ± 1.01	0.93 ± 1.11	1.70 ± 0.95	1.89 ± 1.15

Data are presented as means ± std. dev.

Histologic sections of each tendon stained with H&E and examined under bright field microscopy appeared as parallel bundles of consistently staining collagen fibers interspersed with paucicellular elongate nuclei with little to absent cytoplasm, consistent with tenocytes. Between large bundles

were rare, small caliber, thin-walled blood vessels supported by loose connective tissue. Degeneration was characterized by a loss of fiber orientation and distinction, with hyalinization of the bundles and/or loss of bundle distinction with replacement by disorganized collagen. This was best observed using polarized light where fiber disarray was demonstrated by a loss of regular, patterned transillumination in relation to fiber orientation. Tenocyte nuclei were more rounded and closer spaced with regional progression toward prominent cytoplasmic expansion. Inter-bundle vasculature was often more prominent, though still thin walled, with low to moderate numbers of mononuclear cells infiltrating the peri-vascular loose connective tissue. Rarely vessels were present within collagen bundles in areas of replacement by disorganized collagen. Vessels were most prominent in healthy and diseased tendon sections at the myotendinous junction. Here there was extensive interdigitation of the tendon fiber bundles with skeletal muscle. Interspersed throughout the skeletal muscle were variably sized aggregates of adipocytes which were frequently associated with blood vessels. Additionally, biopsies of each muscle were examined. In these sections there was occasional extension of adipose into myofiber bundles, consistent with fatty degeneration.

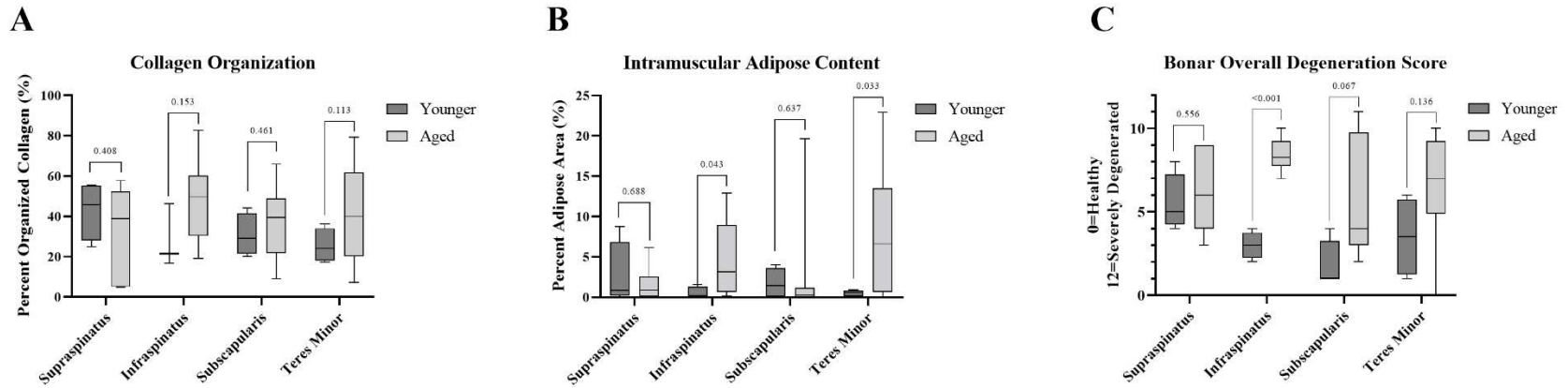


Figure 37. Histomorphometry and histopathology results. A) Percent organized collagen across aged and younger groups in all four tendons. No significant differences were noted between age groups in any tendons. B) Intramuscular adipose content. The aged infraspinatus and teres minor muscle biopsies exhibited significantly increased intramuscular adipose content as compared to their respective younger groups. C) Bonar degeneration scores. The aged infraspinatus samples demonstrated significantly increased pathological degenerative characteristics as compared to the younger infraspinatus samples. Statistical test: Welch's t-test. Box plot indicates median and interquartile range; whiskers indicate maximum and minimum values.

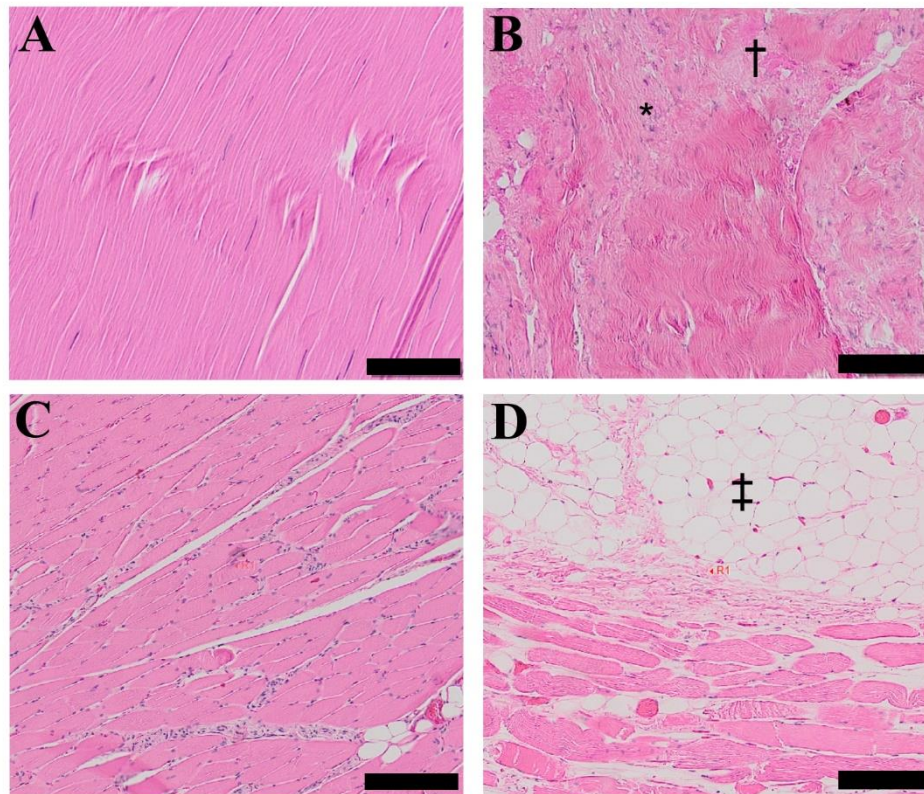


Figure 38. Representative histology micrographs of healthy (A,C) and degenerated (B,D) tendon and muscle sections. Increased tenocytes (*) and increased ground substance (†) typical of degenerated samples. Increased intramuscular adipose content (‡). Scale bars are 100µm.

Gene Expression Analysis

Due to the limited sample size, tendons were pooled into “degenerated” (Bonar score ≥ 6 ; n=6) vs “healthy” (Bonar score ≤ 5 ; n=6) and younger (less than 36 years of age; n=2) vs aged (greater than 55 years of age; n=10) categories for subsequent analyses. Principal component analysis (PCA) revealed gradated separation of sample expression in line with pathological degeneration (Fig 6A). The aged tendons exhibited significantly altered gene expression profiles, with 250 genes significantly upregulated genes (≥ 2 fold, $p \leq 0.05$) and 475 significantly downregulated genes (\leq

-2 fold) in the aged group as compared to the younger group (Fig 6B). The degenerated (Bonar score ≥ 6) tendons also exhibited significantly altered gene expression profiles, with 287 significantly upregulated genes (≥ 2 fold, $p \leq 0.05$) and 158 significantly downregulated genes (≤ -2 fold) in the degenerated group as compared to the healthy group (Fig 6C).

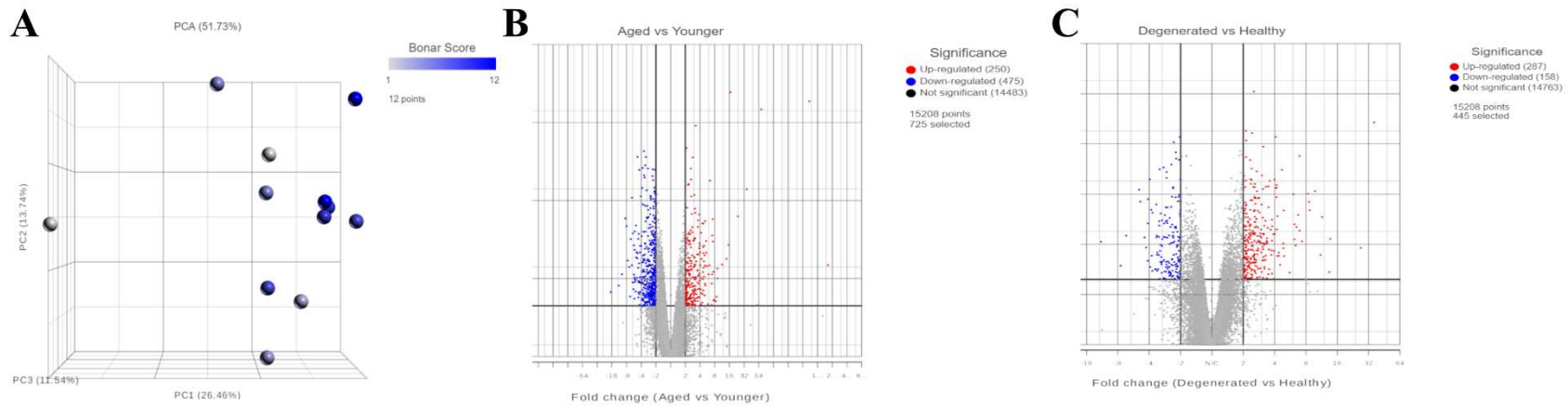


Figure 39. Gene expression changes across all four human rotator tendons secondary to aging and degeneration. A) Principal component analysis (PCA) plot illuminating the differential expression secondary to degeneration. Points colored according to Bonar score. B) Volcano plot comparing the aged and younger samples illustrating the 725 significantly regulated genes with fold change greater than ± 2 . C) Volcano plot comparing the healthy and degenerated samples illustrating the 445 significantly regulated genes with fold change greater than ± 2 .

Correlation Analysis

A correlation analysis was performed as a means of ascertaining the form-function relationships between the gene expression and the biomechanical/histopathological properties of the rotator cuff tendons. For the purposes of this analysis, all tendons were pooled. Only genes with a fold change ≥ 2 resulting from the degenerated vs healthy comparison were considered in this analysis. Reads per kilobase of transcript (RPKM) were compared to the biomechanical and histopathological outcomes parameters (i.e., Ogden μ , Peak Force/Stress, Young's Modulus, Collagen Organization, and Bonar degeneration). Only comparisons which exceeded the significance threshold ($\alpha=0.05$) are reported (Table 12). From this list, 32 genes were listed as having very strong correlations and 22 were listed as having strong correlations.

Table 12. Correlation analysis results

Outcome Parameter	Gene ID	r	p-value
Young's Modulus ($\lambda=1.10$)	RP11-119F19.2	-0.782	0.013
	PET100	-0.766	0.016
	TLCD2	-0.757	0.018
	FOS	-0.739	0.023
	DDIT4	-0.727	0.026
	ANKRD37	-0.684	0.042
	ROMO1	-0.684	0.042
	PFKFB3	-0.682	0.043
	ZNF433	-0.680	0.044

Outcome Parameter	Gene ID	r	p-value
	RPS29	-0.679	0.044
	SPOCK2	-0.674	0.046
Ogden μ -term	TLCD2	-0.753	0.019
	PET100	-0.729	0.026
	RP11-119F19.2	-0.721	0.028
	FOS	-0.693	0.039
	GSTT2B	-0.680	0.044
Peak Stress ($\lambda=1.08$)	TLCD2	-0.750	0.020
	RP11-119F19.2	-0.726	0.027
	PET100	-0.723	0.028
	FOS	-0.673	0.047
	GSTT2B	-0.670	0.049
Percent Organized Collagen	SPTB	0.631	0.028
Bonar Score*	KLF2	0.905	0.000
	TRPM4	0.877	0.000
	ARHGEF39	0.874	0.000
	SLCO4A1	0.856	0.000
	FRAS1	0.852	0.000
	C17orf97	0.850	0.000
	C2CD4C	0.848	0.000
	ZNF415	0.844	0.001
	HES4	0.841	0.001
	CYP7B1	0.829	0.001
	IGFBP4	0.829	0.001

Outcome Parameter	Gene ID	r	p-value
	COL18A1	0.826	0.001
	LINC01106	0.820	0.001
	PLEKHA4	0.819	0.001
	PCSK1	0.815	0.001
	ROMO1	0.814	0.001
	ABI3	0.813	0.001
	STC1	0.812	0.001
	IFITM2	0.812	0.001
	NRXN2	0.812	0.001
	LSM6	0.809	0.001
	DUSP5	0.809	0.001
	ABLIM2	0.807	0.002
	SOX17	0.805	0.002
	RYR2	0.805	0.002
	ESAM	0.804	0.002
	PRKAR1B	0.803	0.002
	ZNF442	0.802	0.002
	ECSCR	0.802	0.002
	LYPD5	0.801	0.002
	FAM107A	0.801	0.002
	C8orf4	0.801	0.002

*Only genes with $r \geq 0.80$ were listed for Bonar Score category.

Discussion

The objective of this investigation was to assess the biomechanical changes to the human rotator cuff secondary to aging using non-destructive testing techniques, so as to enable subsequent histopathological and gene expression analyses. As outlined previously, it is well known that RCR surgeries have unacceptable success rates, necessitating alternative treatment options (i.e., repair augmentation scaffolds). Recent work has shown that by tailoring scaffold mechanics to *in vivo* tissue properties, optimized mechanobiological cues can be provided to resident cell populations that may improve healing outcomes. This work was intended to provide the necessary design targets such that biomimetically optimized scaffolds can be devised. To this end, comprehensive biomechanical testing and modeling was successfully implemented for all four human rotator cuff tendons across multiple age groups. These data presented herein confirm our hypothesis that aged human tendons exhibit decreased biomechanical properties and increased degenerative pathological characteristics.

The exhaustive biomechanical testing and subsequent modeling illustrated the degradation secondary to aging in human tendons. Interestingly, the change to tendon mechanical properties did not manifest similarly in all four rotator cuff tendons. Specifically, these data demonstrate changes were most magnified in the supraspinatus tendons, as evidenced by the difference in Young's modulus vs stretch curves between the younger and aged groups, especially at higher stretch levels. Understanding that there were no significant differences in CSA between the age groups, this decrease in Young's modulus results in reduced tendon stiffness. While these data do not provide information on failure mechanisms (i.e., failure stretch, stress, or method of failure),

it is evident that the aged tendons would absorb less energy for the same stretch/displacement, potentially illuminating an underlying structural mechanism for the increase in tendon tear prevalence in aged tendons ⁽¹⁸⁷⁾. Furthermore, the relatively large departure in aged supraspinatus tendon mechanical properties as compared to the other three tendons agrees with previous clinical studies that have shown the highest tear prevalence in supraspinatus tendons ⁽¹⁷¹⁾. With respect to the original purpose of this research, these data illustrate the large differences in biomechanical properties between the four tendons of the human rotator cuff and across the age range tested. While additional studies will be necessary to confirm, these data suggest that scaffold mechanics should be tailored to the patient age, degeneration level, and tendon to be repaired.

Previous work has investigated changes to rotator cuff biomechanics secondary to aging. Newton et al. recently investigated purely biomechanical changes to rat rotator cuff tendons secondary to aging. That study revealed increased stiffness, decreased stress relaxation, and decreased fatigue secant and tangent moduli in geriatric animals across all four rotator cuff tendons; however, the supraspinatus tendon was not preferentially affected ⁽¹⁸²⁾. These results are interesting considering the data presented herein illustrate a decrease in stiffness and an increase in percent relaxation with age, with the supraspinatus being preferentially affected. Other studies have investigated supraspinatus tendon moduli and found similar values of moduli to what is reported herein (2.6 – 14.4 MPa) and also a moderate/strong correlation with degeneration ($r = -0.60$, $p=0.013$) ^(190,191).

Pathological scoring of all tendons revealed a moderate and significant correlation with age across all four tendons ($r = 0.508$, $p < 0.001$). Interestingly, this correlation was fair and not significant when analyzing the supraspinatus tendons alone. This was most likely a result of the younger cadaver specimens exhibiting increased pathological signs of degeneration in the supraspinatus tendons as compared to the other three tendons. While this work does report using a limited sample size, the difference in degenerative pathology of the four tendons in the younger age group provides interesting information regarding the timeline of pathological manifestation of degeneration in all four tendons.

Gene expression patterns in the pathologically degenerated sample group was aligned with what has been previously reported for tendinopathy. Changes to MMP3 (-1.75 fold decrease, $p=0.06$), Egr1 (3.65 fold increase, $p=0.09$), TNMD (1.72 fold increase, $p=0.35$) and MKX (-2.07 fold decrease, $p=0.02$) seen herein align with previous studies investigating gene expression in tendinopathy/injury samples^(130,192-195). While the small sample size included herein is limiting in terms of gene expression exploration, the changes exhibited in these samples provide another means of positive confirmation beyond pathology that degenerative samples were indeed procured and tested.

Future work should include the utilization of these data to design scaffolds with appropriate mechanical properties to better facilitate patient healing and improve RCR repair success rates. As mentioned previously, the sample size is the main limitation of this study. However, it is the belief

of the authors that the sample size is adequate for the goal of this study, as justified by the power analysis outlined in Section 2.7. Additionally, the utilization of non-destructive biomechanical testing with subsequent same-sample histological and gene expression analyses provides novel information on the aging and degeneration process of human tendons.

Conclusions

The purpose of this study was to characterize the changes to biomechanical properties to the human rotator cuff secondary to aging. Computational modeling techniques were implemented successfully to characterize all four tendons at different ages and pathological states as a means of generating design criteria for future instructive scaffold design. These data presented herein confirm the hypothesis that tendon biomechanical properties are degenerated in aged patients and suggest scaffold mechanical properties should be tailored to patient age and target tendon to optimize healing outcomes.

Chapter 7- Implementation of Healthy Human Supraspinatus Tendon Hyperelastic Properties Into a Finite Element Analysis Package

The work described in this chapter has not been submitted for publication in any journal(s). The data and concepts presented herein are intended to act as preliminary data for future studies.

Introduction

The inadequacy of rotator cuff repair surgeries, particularly in the elderly population with chronically degenerated tendons, is the underlying justification for the research included in this document. In an effort to improve these surgical outcomes, surgical augmentation devices have been designed and implemented as a means of improving initial repair strength or to deliver biologically active ingredients. The impact of appropriate mechanobiological signaling to native cellular populations on collagen homeostasis within fibrous tissue (i.e., intervertebral disc ^(196,197) and tendon ⁽¹⁷⁵⁻¹⁷⁹⁾) is well known; however, current scaffolds have not leveraged the concept of targeted scaffold mechanical properties as a means of delivering optimized mechanobiological signaling.

As outlined in Chapter 6, one of the goals of the human cadaver study was to adequately characterize the biomechanical properties of the human tendons as a means of generating design criteria for such a scaffold. Specifically, rigorous biomechanical testing was employed in conjunction with viscoelastic modeling techniques as a means of deriving material properties for

healthy tendons. These material properties were chosen and derived such that implementation into a finite element (FE) analysis software package (i.e., ABAQUS) could be pursued. Such a material combined with geometric model of the relevant tissues could better inform future tailored scaffold designs. To these ends, the one-term Ogden hyperelastic material properties for the younger supraspinatus group generated in Chapter 6 were implemented into a finite element software analysis package with subsequent comparison to experimental testing as a means of validation.

Materials and Methods

Due to the prevalence of supraspinatus tears clinically and the knowledge that collagen homeostasis is best exemplified in younger patients ⁽¹⁸²⁾, the younger supraspinatus tendon properties were chosen as the target properties for this analysis. A commercial finite element analysis software (ABAQUS, Dassault Systemes SIMULIA, Johnston, RI) was utilized for analyses described herein. A solid rectangular geometry was generated with dimensions designed to match the mean cross-sectional area of the younger supraspinatus group (CSA=47.7 mm²) with a length of 100mm as a means of reducing loading and boundary condition artifacts during analyses. As outlined in Chapter 6, the properties implemented were derived from multi-frequency cyclic testing performed at a stretch magnitude of $\lambda=1.10$, yielding Ogden parameters $\mu= 8.260$ and $\alpha=23.480$. These parameters were implemented into an isotropic Ogden strain energy potential function with $D1 = 0.003$. The fibers were meshed with quadratic tetrahedral elements (C3D10) yielding 2,033 elements total. All nodes on one end of the rectangular bar were subjected to an encastre condition (i.e., all displacements and rotations were nil). As a means of providing validation to these material properties as implemented into the FE software, the rectangular bar

was subjected to the mean experimental load exhibited at $\lambda=1.08$ by all younger supraspinatus tendons ($F=219.93$ N). As a means of matching experimental loading conditions, this load was applied to a reference point which was kinematically coupled to all nodes on the free end of the rectangular bar (i.e., opposing the end subjected to encastre conditions). FE predicted longitudinal stress and strain within the rectangular bar under these loading conditions were compared to experimentally measured values as a means of validating the material properties. FE outcome measurements were taken from the center of the rectangular bar in accordance with Saint-Venant's principle as a means of minimizing edge/loading effects.

Results

Mesh convergence was considered adequate using the 2,033-element mesh configuration, yielding 0.001% change in longitudinal strain as compared to the results of the 517-element mesh. The deformation of the rectangular bar under the applied loading conditions is shown below (Figure 41). Computationally predicted longitudinal strain in the mid-section of the rectangular bar was within 8.38% percent of experimentally measured strain ($\epsilon_{\text{computational}} = 8.67\%$, $\epsilon_{\text{experimental}} = 8.00\%$). Additionally, computationally predicted longitudinal stress was within 8.80% of experimentally measured stress ($\sigma_{\text{computational}} = 5.01$ MPa, $\sigma_{\text{experimental}} = 4.61$ MPa, Figure 42).

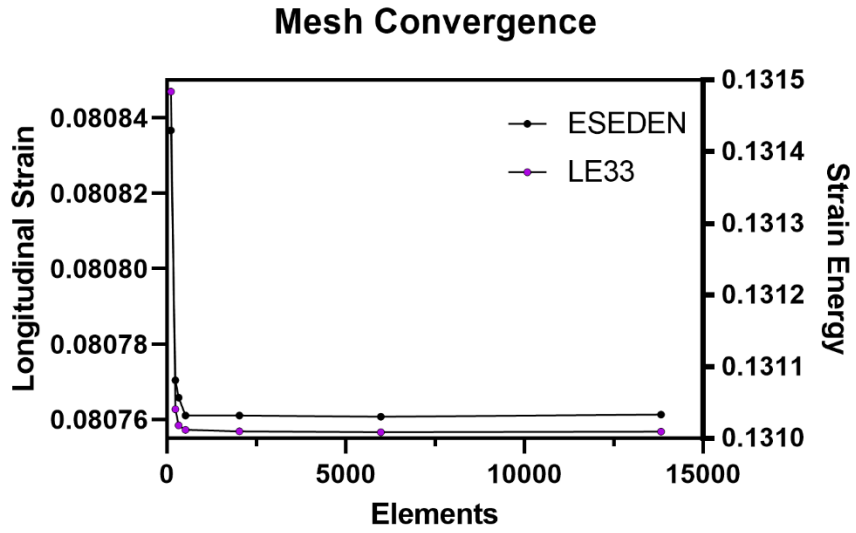


Figure 40. Mesh convergence results using longitudinal strain and strain energy.

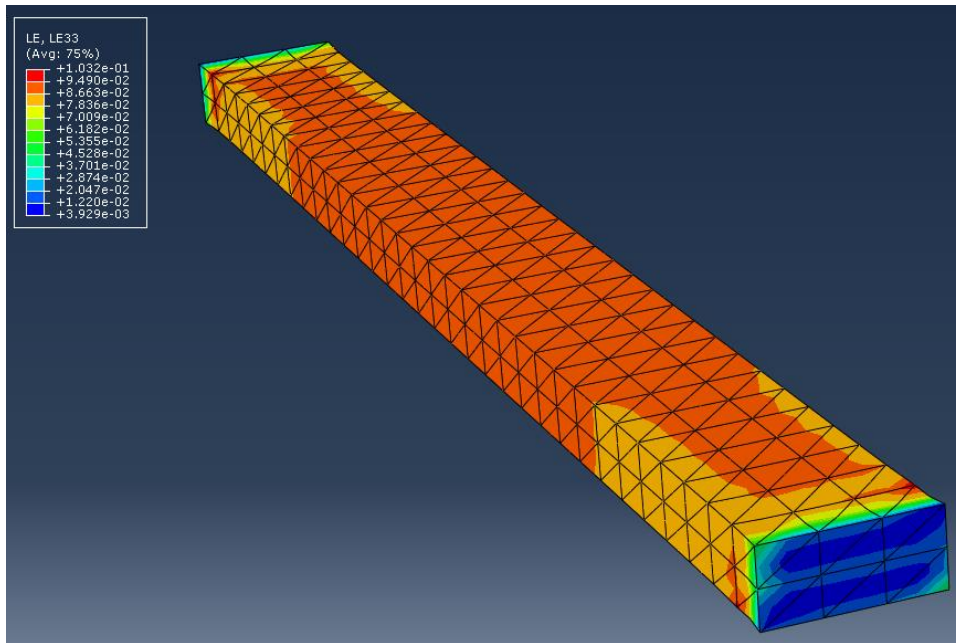


Figure 41. Longitudinal strain in rectangular bar.

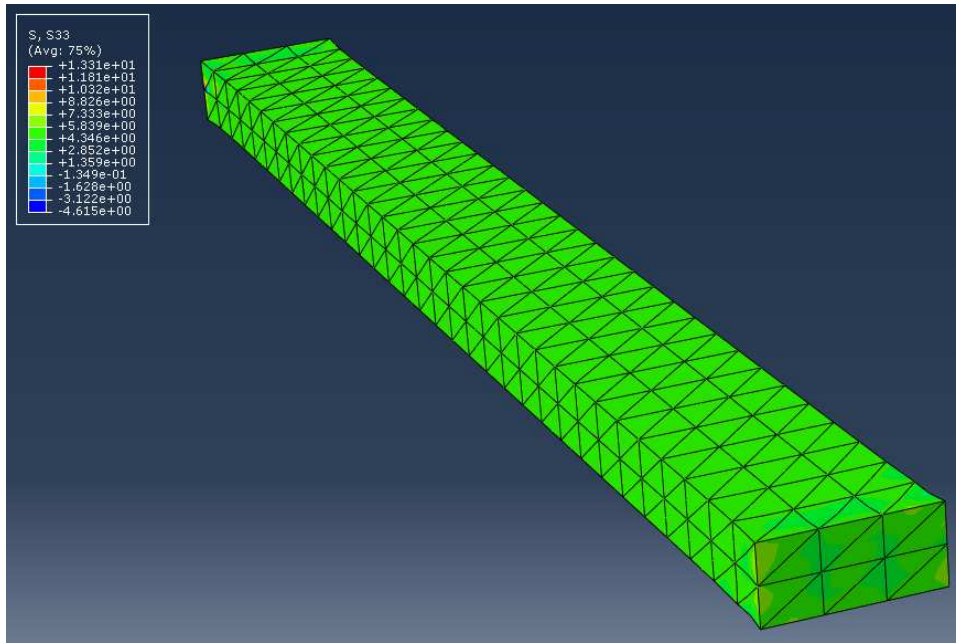


Figure 42. Longitudinal stress of rectangular bar.

Discussion

The goal of this analysis was to implement the one-term Ogden hyperelastic material properties generated in Chapter 6 into a FE package to enable future design of a scaffold that leverages mechanobiological signaling as a means of driving improved healing outcomes in a rotator cuff repair situation. As outlined previously, computationally predicted stress and strain values matched experimentally measured values with 8.80% and 8.38%, respectively. Future work will entail utilizing these material properties in conjunction with anatomically accurate geometries as a means of determining the local micromechanical environment within the tendon enthesis region. These analyses have the potential to inform future scaffold designs to enable utilization of mechanobiological signaling as a means of driving improved healing outcomes.

Chapter 8- Conclusion

Summary of Work

This work details the investigation of multiple animal models of chronic rotator cuff degeneration through simulated injury, changes to tendons secondary to an animal model of osteoporosis, and characterization of human rotator cuff tendon properties across a spectrum of ages and degeneration levels. To these ends, exhaustive characterization utilizing biomechanical testing, histopathological analyses, histomorphometry analyses, microCT analyses, and gene expression analyses was employed.

Chapter 2 detailed the investigation of a partial transection model of chronic rotator cuff degeneration, generated through release of one half of the width of the tendon from its insertion. These samples were analyzed utilizing histopathology techniques which revealed characteristics aligned with chronic degeneration in the unimpaired half of the tendon; however, the transected half of the tendon exhibited marked to severe histological characteristics indicative of an acute reparative process, as well as significant, irreparable retraction of the tendon from its insertion. The shortcomings of this model provided the insight and justification for Chapters 3 and 4.

Chapter 3 described the findings of the sharp transection model of chronic rotator cuff degeneration. It was hypothesized that by releasing one half of the thickness of the tendon, histological changes aligned with chronic rotator cuff degeneration would be induced, while also

eliminating or severely reducing tendon retraction, enabling subsequent repair surgery simulations. As evidenced by the comparative biomechanical, histological, and gene expression data, this model resulted in tendons with characteristics aligned with chronic degeneration similar to what has been documented in humans clinically.

Chapter 4 detailed the findings of the combed fenestration model of chronic rotator cuff degeneration. This model was induced through surgical microtrauma of the tendon midbody utilizing 16 cuts in the fiber direction. It was hypothesized that this surgical trauma would result in histological changes aligned with chronic rotator cuff degeneration while maintaining the integrity of the insertion, enabling investigations of therapies designed at reversing degeneration/tendinopathy prior to tendon injury. As demonstrated by the comparative biomechanical, histological, and gene expression data, this model resulted in tendons with characteristics aligned with chronic degeneration similar to what has been documented in humans clinically. Additionally, similar biomechanical changes were noted in this combed fenestration model as what was noted for the sharp transection model. This finding is particularly interesting in light of the similarity in pathologies stemming from inherently different surgical trauma, which may in part explain the difficulty of determining the underlying cause(s) of chronic rotator cuff degeneration in humans.

As outlined in Chapter 5, rotator cuff repair procedures exhibit elevated failure rates in patients with osteoporosis. To date, the underlying mechanism for these increased failures has not been

elucidated. Chapter 5 described the findings of a study conducted to ascertain whether soft tissue mechanics are altered in a large animal model of osteoporosis, and whether a current standard of care for osteoporosis impacts those soft tissues. Data presented within this chapter confirmed that biomechanical properties and insertional structure of tendons are diminished in an ovine model of osteoporosis. Additionally, the cohort of tendons harvested from animals treated with systemic bisphosphonates exhibited improved biomechanical properties as compared to the those without treatment.

Chapter 6 reported the results of biomechanical, histological, and gene expression analyses on human rotator cuff tendon tissues across a spectrum of ages and degeneration levels. As outlined in that chapter, tendons increased in degenerative characteristics with age, albeit at differing trajectories and magnitudes across the four tendons of the rotator cuff. The supraspinatus tendons tested exhibited the greatest magnitude of degenerative traits, and some of those traits were exhibited even in the younger specimens that were tested, insinuating degenerative changes manifest at an early age in that tendon. Additionally, all four tendons exhibited differing biomechanical properties, suggesting “instructive” repair scaffolds may need to be tailored to specific tendons / tear situations (i.e., supraspinatus only vs combined supraspinatus and infraspinatus tear).

Chapter 7 outlined preliminary data illustrating the capability for the one-term Ogden hyperelastic parameters generated in Chapter 6 to be used as input material properties in a finite element model such that future “instructive” scaffold design can be pursued in future work.

Human Cadaver Data Validates Sheep Models of Chronic Rotator Cuff Degeneration

The work detailed in Chapters 2, 3, and 4 was pursued as a means of generating clinically translatable large animal model(s) of chronic rotator cuff degeneration. As outlined in each of those aims, histological and gene expression data from previous studies or intra-operative biopsies were utilized as a means of model validation. However, adequate data regarding changes to tendon biomechanics following degeneration has never been reported. As such, a portion of the justification for Specific Aim 5 was to leverage the biomechanical testing data derived from human cadavers samples across a spectrum of degeneration levels as a means of validating our ovine models. Each Specific Aim presented herein has outlined the results of each study independently; therefore, the goal of this section is to provide a brief side-by-side comparison as a means of model validation. Specifically, the main findings of the biomechanical and histological analyses from each independent study will be compared to the human cadaver data presented in Chapter 6.

Biomechanical Comparisons

As outlined in Chapters 3 and 4, deleterious changes to biomechanical properties of the ovine infraspinatus tendons were noted at all timepoints in both the CF and ST models, as compared to the Control (healthy) tendons. Marked reductions in peak stress and increases of percent relaxation

were noted at all timepoints in the CF and ST models. For brevity, only comparisons using the $\lambda = 1.08$ data will be presented here ($\lambda = 1.06$ results provide similar results, thus inclusion was deemed redundant).

The peak stress metric was reduced similarly in degenerated human tendons and in both ovine models. With respect to the ST model, percent reductions in peak stress as compared to the Control group were 65.9%, 74.2%, and 61.4% for the 6, 12, and 18-week timepoints, respectively (Figure 43). The CF model exhibited similar changes, with percent reductions in peak stress of 55.3%, 55.3%, and 39.4% for the 6, 12, and 18-week timepoints, respectively (Figure 43). In comparison, percent reductions in peak stress exhibited by the aged cadaver tendons as compared to the younger tendons were 65.6%, 52.6%, 44.6%, and 25.6% for the supraspinatus, infraspinatus, subscapularis, and teres minor tendons, respectively (Figure 43). As outlined previously, the clinically documented prevalence of tears is greatest in the supraspinatus tendons, which also exhibited the greatest magnitude of degenerative changes as outlined in Chapter 6.

Increased percent relaxation during stress-relaxation testing was exhibited by degenerated human tendons and in both ovine models. With respect to the ST model, percent increase in percent relaxation as compared to the Control group were 51.7%, 52.5%, and 73.1% for the 6, 12, and 18-week timepoints, respectively (Figure 44). The CF model exhibited similar changes, with percent increase in percent relaxation of 44.5%, 10.5%, and 75.6% for the 6, 12, and 18-week timepoints, respectively (Figure 44). In comparison, percent increase in percent relaxation exhibited by the

aged cadaver tendons as compared to the younger tendons were 14.5%, 22.4%, 23.5%, and 3.3% for the supraspinatus, infraspinatus, subscapularis, and teres minor tendons, respectively (Figure 44). While differences in the magnitude of changes between ovine models and human cadavers are evident, all aged/degenerated groups exhibited increased percent relaxation values.

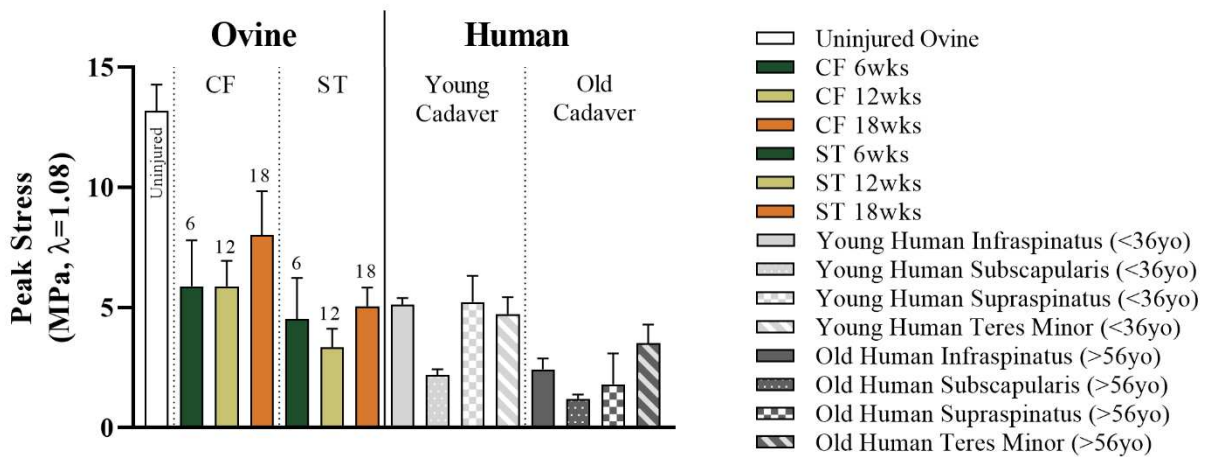


Figure 43. Peak stress for all timepoints of ST and CF models as well as younger and aged cadaver groups.

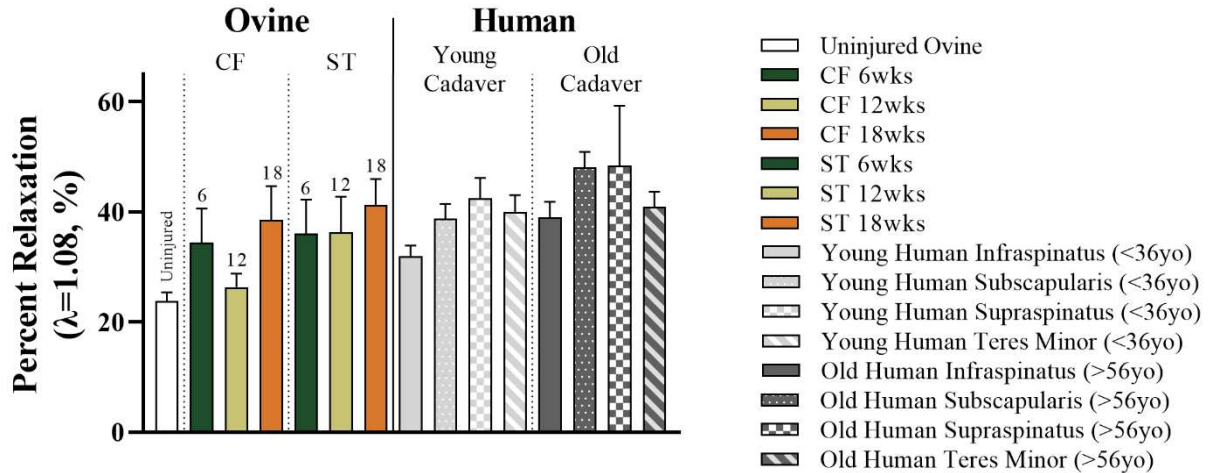


Figure 44. Peak stress for all timepoints of ST and CF models as well as younger and aged cadaver groups.

Histological Comparisons

Histological characterization of chronically degenerated human rotator cuff tendons has been well documented^(91,126,153,198). As outlined in Chapter 6, changes noted within the aged human cadaver samples were similar in manifestation to those described in chronically degenerated human tendon samples. Specifically, degeneration was typified by decreased collagen fiber organization, expanded tenocyte populations exhibiting loss of phenotypical spindle-shaped morphology, increased vascularization, and increased presence of ground substance. In this work, the histological manifestations of chronic degeneration have been semi-quantitatively assessed through Bonar scoring. As outlined in Chapters 3 and 4, the sharp transection and combed fenestration models exhibited Bonar scores remarkably aligned with those seen in the intraoperative biopsies of chronically degenerated rotator cuff tendons (obtained from patients undergoing primary reverse total shoulder arthroplasty) (Figure 45). The aged cadaver tendons

exhibited markedly increased Bonar scores as compared to the younger specimens, while not fully reaching the magnitude demonstrated by the intraoperative biopsies (Figure 45). When taken together with the biomechanical testing results presented in Chapter 6, these findings suggest physiologically relevant biomechanical degradation occurs even in tendons that do not exhibit advanced histologic signs of degeneration.

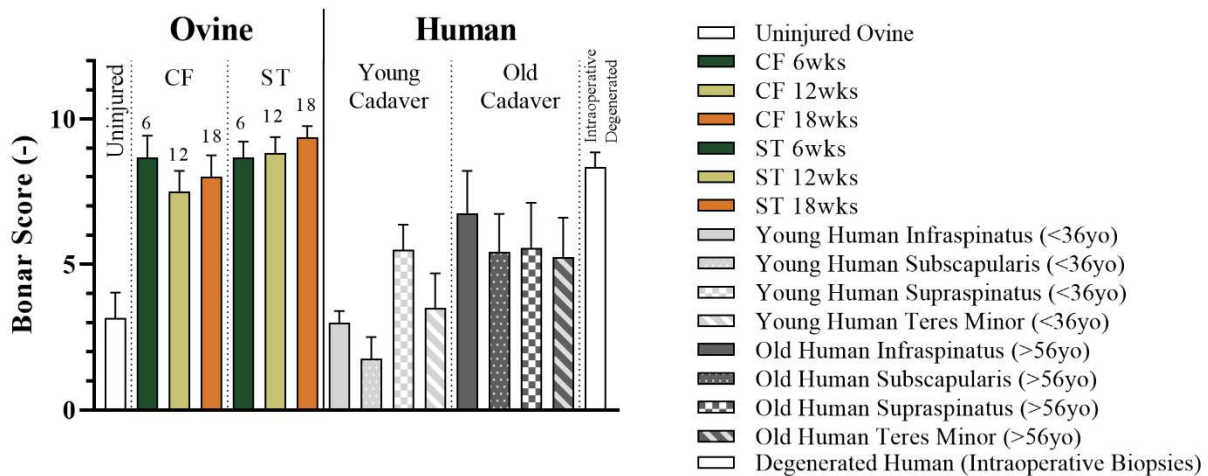


Figure 45. Bonar score results for all timepoints of ST and CF models as well as younger and aged cadaver groups.

Future Work

The results reported within this dissertation work illustrate the temporal nature of the manifestation of degenerative tendon pathology in human tendons. The animal models described herein exhibit similar changes to those seen in humans and will lend themselves as useful platforms with which to investigate future therapeutics. Additionally, the investigation of changes to tendon mechanics secondary to osteoporosis provides useful insight into potential causes leading to the increased

surgical repair failures experienced by osteoporotic patients. Future work should utilize the computational models of each tendon to generate tailored repair scaffolds capable of recapitulating the mechanical environment of a healthy rotator cuff. As evidenced by the differential properties between all four tendons, such a scaffold should have directional gradients of mechanical properties to best match the human rotator cuff. Additionally, future work should also continue investigation of the impact of bisphosphonates on tendon mechanical properties, such that a mechanistic explanation can be generated.

References

1. Lorbach O, Baums MH, Kostuj T, Pauly S, Scheibel M, Carr A, et al. Advances in biology and mechanics of rotator cuff repair. *Knee Surgery, Sports Traumatology, Arthroscopy*. 2015;23:530-41.
2. Apreleva M, Özbaydar M, Fitzgibbons PG, Warner JJP. Rotator cuff tears: The effect of the reconstruction method on three-dimensional repair site area. *Arthroscopy: The Journal of Arthroscopic & Related Surgery*. 2002;18:519-26.
3. Santoni BG, McGilvray KC, Lyons AS, Bansal M, Turner AS, Macgillivray JD, et al. Biomechanical analysis of an ovine rotator cuff repair via porous patch augmentation in a chronic rupture model. *Am J Sports Med*. Apr 2010;38(4):679-86. Epub 2010/04/02.
4. Colvin AC, Egorova N, Harrison AK, Moskowitz A, Flatow EL. National trends in rotator cuff repair. *The Journal of bone and joint surgery American volume*. 2012;94:227-33.
5. Mather RC, Koenig L, Acevedo D, Dall TM, Gallo P, Romeo A, et al. The Societal and Economic Value of Rotator Cuff Repair. *J Bone Joint Surg Am*. 952013. p. 1993-2000.
6. Chakravarty K, Webley M. Shoulder joint movement and its relationship to disability in the elderly. *The Journal of rheumatology*. Aug 1993;20(8):1359-61. Epub 1993/08/01.
7. Savin D, Meadows M, Verma N. Rotator Cuff Healing: Improving Biology. *Operative Techniques in Sports Medicine*. 2017;25:34-40.
8. Oh LS, Wolf BR, Hall MP, Levy BA, Marx RG. Indications for rotator cuff repair: a systematic review. *Clin Orthop Relat Res*. Feb 2007;455:52-63. Epub 2006/12/21.
9. Reilly P, Macleod I, Macfarlane R, Windley J, Emery RJ. Dead men and radiologists don't lie: a review of cadaveric and radiological studies of rotator cuff tear prevalence. *Ann R Coll Surg Engl*. Mar 2006;88(2):116-21. Epub 2006/03/23.
10. Thigpen CA, Shaffer MA, Gaunt BW, Leggin BG, Williams GR, Wilcox RB. The American Society of Shoulder and Elbow Therapists' consensus statement on rehabilitation following arthroscopic rotator cuff repair. *Journal of Shoulder and Elbow Surgery*. 2016;25(4):521-35.
11. Fukuda H. The management of partial-thickness tears of the rotator cuff. *J Bone Joint Surg Br*. Jan 2003;85(1):3-11. Epub 2003/02/15.
12. Matthews TJ, Hand GC, Rees JL, Athanasou NA, Carr AJ. Pathology of the torn rotator cuff tendon. Reduction in potential for repair as tear size increases. *J Bone Joint Surg Br*. Apr 2006;88(4):489-95. Epub 2006/03/29.
13. McIntyre LF, Bishai SK, Brown PB, Bushnell BD, Trenhaile SW. Patient-Reported Outcomes After Use of a Bioabsorbable Collagen Implant to Treat Partial and Full-Thickness Rotator Cuff Tears. *Arthroscopy: The Journal of Arthroscopic & Related Surgery*. 2019;35(8):2262-71.
14. Galatz LM, Ball CM, Teefey SA, Middleton WD, Yamaguchi K. The outcome and repair integrity of completely arthroscopically repaired large and massive rotator cuff tears. *J Bone Joint Surg Am*. Feb 2004;86-a(2):219-24. Epub 2004/02/13.
15. Cole BJ, McCarty LP, Kang RW, Alford W, Lewis PB, Hayden JK. Arthroscopic rotator cuff repair: Prospective functional outcome and repair integrity at minimum 2-year follow-up. *Journal of Shoulder and Elbow Surgery*. 2007;16(5):579-85.

16. Harryman DT, 2nd, Mack LA, Wang KY, Jackins SE, Richardson ML, Matsen FA, 3rd. Repairs of the rotator cuff. Correlation of functional results with integrity of the cuff. *J Bone Joint Surg Am.* Aug 1991;73(7):982-9. Epub 1991/08/01.
17. Meyer M, Klouche S, Rousselin B, Boru B, Bauer T, Hardy P. Does arthroscopic rotator cuff repair actually heal? Anatomic evaluation with magnetic resonance arthrography at minimum 2 years follow-up. *J Shoulder Elbow Surg.* Apr 2012;21(4):531-6. Epub 2011/05/24.
18. Maruvada S M-IA, Varacallo M. Anatomy, Rotator Cuff. *StatPearls.* Epub 2020 Oct 27.
19. Simon S. Orthopaedic basic science. American Academy of Orthopaedic Surgeons. 1994 1994.
20. Mora MV. Stem cell therapy in the management of shoulder rotator cuff disorders. *World Journal of Stem Cells.* 2015;7(4):691.
21. Vogel KG, Peters JA. Isolation of Proteoglycans from Tendon. Humana Press. p. 009-17.
22. Schwartz AG, Long F, Thomopoulos S. Enthesis fibrocartilage cells originate from a population of Hedgehog-responsive cells modulated by the loading environment. *Development.* 2015;142(1):196-206.
23. Tanzer ML. Cross-Linking of Collagen. *Science.* 1973;180(4086):561-6.
24. Yang G, Crawford RC, Wang JHC. Proliferation and collagen production of human patellar tendon fibroblasts in response to cyclic uniaxial stretching in serum-free conditions. *Journal of Biomechanics.* 2004;37(10):1543-50.
25. Nichols AEC, Best KT, Loiselle AE. The cellular basis of fibrotic tendon healing: challenges and opportunities. *Translational Research.* 2019.
26. Schwartz AG, Pasteris JD, Genin GM, Daulton TL, Thomopoulos S. Mineral Distributions at the Developing Tendon Enthesis. *PloS one.* 2012;7(11):e48630.
27. Ogden RW. Large deformation isotropic elasticity – on the correlation of theory and experiment for incompressible rubberlike solids. *Proceedings of the Royal Society of London A Mathematical and Physical Sciences.* 1972;326(1567):565-84.
28. Ramo NL, Troyer KL, Puttlitz CM. Comparing Predictive Accuracy and Computational Costs for Viscoelastic Modeling of Spinal Cord Tissues. *Journal of Biomechanical Engineering.* 2019;141(5):051009.
29. Lucas SR, Bass CR, Salzar RS, Oyen ML, Planchak C, Ziemba A, et al. Viscoelastic properties of the cervical spinal ligaments under fast strain-rate deformations. *Acta Biomaterialia.* 2008;4(1):117-25.
30. Huang C-Y, Wang VM, Flatow EL, Mow VC. Temperature-dependent viscoelastic properties of the human supraspinatus tendon. *Journal of Biomechanics.* 2009;42(4):546-9.
31. Fung YC. *Biomechanics: mechanical properties of living tissues.* New York: Springer-Verlag. 1993;2:568.
32. McGilvray KC, Sarkar R, Nguyen K, Puttlitz CM. A biomechanical analysis of venous tissue in its normal and post-phlebotic conditions. *J Biomech.* Nov 16 2010;43(15):2941-7. Epub 2010/09/25.
33. Fehringner EV, Sun J, VanOeveren LS, Keller BK, Matsen FA. Full-thickness rotator cuff tear prevalence and correlation with function and co-morbidities in patients sixty-five years and older. *Journal of shoulder and elbow surgery.* 2008;17:881-5.

34. Hashimoto T, Nobuhara K, Hamada T. Pathologic evidence of degeneration as a primary cause of rotator cuff tear. *Clin Orthop Relat Res*. Oct 2003(415):111-20. Epub 2003/11/13.
35. Rudzki JR, Adler RS, Warren RF, Kadrmaz WR, Verma N, Pearle AD, et al. Contrast-enhanced ultrasound characterization of the vascularity of the rotator cuff tendon: age- and activity-related changes in the intact asymptomatic rotator cuff. *J Shoulder Elbow Surg*. Jan-Feb 2008;17(1 Suppl):96S-100S. Epub 2007/12/11.
36. Longo UG, Ronga M, Maffulli N. Achilles tendinopathy. *Sports Med Arthrosc Rev*. Jun 2009;17(2):112-26. Epub 2009/05/15.
37. Longo UG, Franceschi F, Ruzzini L, Rabitti C, Morini S, Maffulli N, et al. Histopathology of the supraspinatus tendon in rotator cuff tears. *Am J Sports Med*. Mar 2008;36(3):533-8. Epub 2007/11/17.
38. Tom S, Parkinson J, Ilic MZ, Cook J, Feller JA, Handley CJ. Changes in the composition of the extracellular matrix in patellar tendinopathy. *Matrix Biology*. 2009;28(4):230-6.
39. Mustafa I, Jüri-Toomas K, Sonja ES, Randi O, Khaled M. More tendon degeneration in patients with shoulder osteoarthritis. *Knee Surgery, Sports Traumatology, Arthroscopy*. 2018.
40. Cook JL, Feller JA, Bonar SF, Khan KM. Abnormal tenocyte morphology is more prevalent than collagen disruption in asymptomatic athletes' patellar tendons. *Journal of Orthopaedic Research*. 2004;22(2):334-8.
41. Jelinsky SA, Rodeo SA, Li J, Gulotta LV, Archambault JM, Seeherman HJ. Regulation of gene expression in human tendinopathy. *BMC Musculoskeletal Disorders*. 2011;12(1):86.
42. Ueda Y, Inui A, Mifune Y, Takase F, Kataoka T, Kurosawa T, et al. Molecular changes to tendons after collagenase-induced acute tendon injury in a senescence-accelerated mouse model. *BMC Musculoskeletal Disorders*. 2019;20(1).
43. Sugiyama Y, Naito K, Goto K, Kojima Y, Furuhashi A, Igarashi M, et al. Effect of aging on the tendon structure and tendon-associated gene expression in mouse foot flexor tendon. *Biomedical Reports*. 2019.
44. Ma J, Piuze NS, Muschler GF, Iannotti JP, Ricchetti ET, Derwin KA. Biomarkers of Rotator Cuff Disease Severity and Repair Healing. *JBJs Reviews*. 2018;6(9):e9.
45. Klatt-Schulz F, Minkwitz S, Schmock A, Bormann N, Kurtoglu A, Tsitsilonis S, et al. Different Achilles Tendon Pathologies Show Distinct Histological and Molecular Characteristics. *International Journal of Molecular Sciences*. 2018;19(2):404.
46. Minkwitz S, Schmock A, Kurtoglu A, Tsitsilonis S, Manegold S, Wildemann B, et al. Time-Dependent Alterations of MMPs, TIMPs and Tendon Structure in Human Achilles Tendons after Acute Rupture. *International Journal of Molecular Sciences*. 2017;18(10):2199.
47. Buckley MR, Evans EB, Matuszewski PE, Chen YL, Satchel LN, Elliott DM, et al. Distributions of types I, II and III collagen by region in the human supraspinatus tendon. *Connect Tissue Res*. 2013;54(6):374-9. Epub 2013/10/04.
48. Liu H, Xu J, Liu C-F, Lan Y, Wylie C, Jiang R. Whole transcriptome expression profiling of mouse limb tendon development by using RNA-seq. *Journal of Orthopaedic Research*. 2015;33(6):840-8.
49. Vaughn NH, Stepanyan H, Gallo RA, Dhawan A. Genetic Factors in Tendon Injury: A Systematic Review of the Literature. *Orthopaedic Journal of Sports Medicine*. 2017;5(8):232596711772441.

50. Deprés-tremblay G, Chevrier A, Snow M, Hurtig MB, Rodeo S, Buschmann MD. Rotator cuff repair: a review of surgical techniques, animal models, and new technologies under development Rotator cuff anatomy and pathology. *J Shoulder Elbow Surg.* 2016;25:2078-85.
51. Gerber C, Fuchs B, Hodler J. The results of repair of massive tears of the rotator cuff. *J Bone Joint Surg Am.* Apr 2000;82(4):505-15. Epub 2000/04/13.
52. Cancienne JM, Brockmeier SF, Kew ME, Deasey MJ, Werner BC. The Association of Osteoporosis and Bisphosphonate Use With Revision Shoulder Surgery After Rotator Cuff Repair. *Arthroscopy: The Journal of Arthroscopic & Related Surgery.* 2019;35(8):2314-20.
53. Chung SW, Oh JH, Gong HS, Kim JY, Kim SH. Factors Affecting Rotator Cuff Healing After Arthroscopic Repair: Osteoporosis as One of the Independent Risk Factors. *The American Journal of Sports Medicine.* 2011;39(10):2099-107.
54. Entezari V, Lazarus M. Surgical Considerations in Managing Osteoporosis, Osteopenia, and Vitamin D Deficiency During Arthroscopic Rotator Cuff Repair. *Orthopedic Clinics of North America.* 2019/04/01/ 2019;50(2):233-43.
55. Wright NC, Looker AC, Saag KG, Curtis JR, Delzell ES, Randall S, et al. The Recent Prevalence of Osteoporosis and Low Bone Mass in the United States Based on Bone Mineral Density at the Femoral Neck or Lumbar Spine. *Journal of Bone and Mineral Research.* 2014;29(11):2520-6.
56. McClung M, Harris ST, Miller PD, Bauer DC, Davison KS, Dian L, et al. Bisphosphonate Therapy for Osteoporosis: Benefits, Risks, and Drug Holiday. *The American Journal of Medicine.* 2013;126(1):13-20.
57. Lindsay R, Krege JH, Marin F, Jin L, Stepan JJ. Teriparatide for osteoporosis: importance of the full course. *Osteoporosis International.* 2016;27(8):2395-410.
58. Depres-Tremblay G, Chevrier A, Snow M, Hurtig MB, Rodeo S, Buschmann MD. Rotator cuff repair: a review of surgical techniques, animal models, and new technologies under development. *J Shoulder Elbow Surg.* Dec 2016;25(12):2078-85. Epub 2016/08/25.
59. Edelstein L, Thomas SJ, Soslowsky LJ. Rotator cuff tears: what have we learned from animal models? *Journal of musculoskeletal & neuronal interactions.* 2011;11:150-62.
60. Boileau P, Brassart N, Watkinson DJ, Carles M, Hatzidakis AM, Krishnan SG. Arthroscopic repair of full-thickness tears of the supraspinatus: does the tendon really heal? *J Bone Joint Surg Am.* Jun 2005;87(6):1229-40. Epub 2005/06/03.
61. Gazielly DF, Gleyze P, Montagnon C. Functional and anatomical results after rotator cuff repair. *Clin Orthop Relat Res.* Jul 1994(304):43-53. Epub 1994/07/01.
62. Mellado JM, Calmet J, Olona M, Esteve C, Camins A, Perez Del Palomar L, et al. Surgically repaired massive rotator cuff tears: MRI of tendon integrity, muscle fatty degeneration, and muscle atrophy correlated with intraoperative and clinical findings. *AJR American journal of roentgenology.* May 2005;184(5):1456-63. Epub 2005/04/28.
63. Yoo JC, Ahn JH, Koh KH, Lim KS. Rotator cuff integrity after arthroscopic repair for large tears with less-than-optimal footprint coverage. *Arthroscopy : the journal of arthroscopic & related surgery : official publication of the Arthroscopy Association of North America and the International Arthroscopy Association.* Oct 2009;25(10):1093-100. Epub 2009/10/06.

64. Gall TT, Santoni BG, Egger EL, Puttlitz CM, Rooney MB. In Vitro Biomechanical Comparison of Polypropylene Mesh, Modified Three-Loop Pulley Suture Pattern, and a Combination for Repair of Distal Canine Achilles' Tendon Injuries. *Veterinary Surgery*. 2009;38(7):845-51.
65. Hee CK, Dines JS, Dines DM, Roden CM, Wisner-Lynch LA, Turner AS, et al. Augmentation of a Rotator Cuff Suture Repair Using rhPDGF-BB and a Type I Bovine Collagen Matrix in an Ovine Model. *The American Journal of Sports Medicine*. 2011;39:1630-40.
66. Karuppaiah K, Sinha J. Scaffolds in the management of massive rotator cuff tears: current concepts and literature review. *EFORT Open Rev*. Sep 2019;4(9):557-66. Epub 2019/10/11.
67. Thon SG, Belk JW, Bravman JT, McCarty EC, Savoie Iii FH. Regeneten bio-inductive collagen scaffold for rotator cuff tears: indications, technique, clinical outcomes, and review of current literature. *Annals of Joint*. 2020;5:41-.
68. McGilvray KC, Lyons AS, Turner AS, MacGillivray JD, Coleman SH, Puttlitz CM. Shoulder Tendon Repair Biomechanics Using a Polyurethane Patch in a Chronic Ovine Defect Model. 2007(47985):853-4.
69. Ricchetti ET, Aurora A, Iannotti JP, Derwin KA. Scaffold devices for rotator cuff repair. *Journal of Shoulder and Elbow Surgery*. 2012/02/01/ 2012;21(2):251-65.
70. Derwin KA, Codsí MJ, Milks RA, Baker AR, McCarron JA, Iannotti JP. Rotator cuff repair augmentation in a canine model with use of a woven poly-L-lactide device. *J Bone Joint Surg Am*. May 2009;91(5):1159-71. Epub 2009/05/05.
71. Easley J, Puttlitz C, Hackett E, Broomfield C, Nakamura L, Hawes M, et al. A prospective study comparing tendon-to-bone interface healing using an interposition bioresorbable scaffold with a vented anchor for primary rotator cuff repair in sheep. *Journal of Shoulder and Elbow Surgery*. 2019.
72. DeJardin LM, Arnoczky SP, Ewers BJ, Haut RC, Clarke RB. Tissue-Engineered Rotator Cuff Tendon Using Porcine Small Intestine Submucosa. *The American Journal of Sports Medicine*. 2001;29(2):175-84.
73. Gulotta LV, Kovacevic D, Ehteshami JR, Dagher E, Packer JD, Rodeo SA. Application of Bone Marrow-Derived Mesenchymal Stem Cells in a Rotator Cuff Repair Model. *The American Journal of Sports Medicine*. 2009;37(11):2126-33.
74. Gulotta LV, Kovacevic D, Montgomery S, Ehteshami JR, Packer JD, Rodeo SA. Stem Cells Genetically Modified With the Developmental Gene MT1-MMP Improve Regeneration of the Supraspinatus Tendon-to-Bone Insertion Site. *The American Journal of Sports Medicine*. 2010;38(7):1429-37.
75. Gulotta LV, Kovacevic D, Packer JD, Ehteshami JR, Rodeo SA. Adenoviral-Mediated Gene Transfer of Human Bone Morphogenetic Protein-13 Does Not Improve Rotator Cuff Healing in a Rat Model. *The American Journal of Sports Medicine*. 2011;39(1):180-7.
76. Gulotta LV, Kovacevic D, Packer JD, Deng XH, Rodeo SA. Bone Marrow-Derived Mesenchymal Stem Cells Transduced With Scleraxis Improve Rotator Cuff Healing in a Rat Model. *The American Journal of Sports Medicine*. 2011;39(6):1282-9.
77. Kida Y, Morihara T, Matsuda K-I, Kajikawa Y, Tachiiri H, Iwata Y, et al. Bone marrow-derived cells from the footprint infiltrate into the repaired rotator cuff. *Journal of Shoulder and Elbow Surgery*. 2013;22(2):197-205.

78. Oh JH, Chung SW, Kim SH, Chung JY, Kim JY. 2013 Neer Award: Effect of the adipose-derived stem cell for the improvement of fatty degeneration and rotator cuff healing in rabbit model. *Journal of Shoulder and Elbow Surgery*. 2014/04/01/ 2014;23(4):445-55.
79. Shen W, Chen J, Yin Z, Chen X, Liu H, Heng BC, et al. Allogeneous Tendon Stem/Progenitor Cells in Silk Scaffold for Functional Shoulder Repair. *Cell Transplantation*. 2012;21(5):943-58.
80. Wall KC, Toth AP, Garrigues GE. How to Use a Graft in Irreparable Rotator Cuff Tears: A Literature Review Update of Interposition and Superior Capsule Reconstruction Techniques. *Current Reviews in Musculoskeletal Medicine*. 2018;11(1):122-30.
81. Soslowsky LJ, Carpenter JE, DeBano CM, Banerji I, Moalli MR. Development and use of an animal model for investigations on rotator cuff disease. *J Shoulder Elbow Surg*. Sep-Oct 1996;5(5):383-92. Epub 1996/09/01.
82. Grumet RC, Hadley S, Diltz MV, Lee TQ, Gupta R. Development of a new model for rotator cuff pathology: the rabbit subscapularis muscle. *Acta Orthop*. Feb 2009;80(1):97-103. Epub 2009/02/24.
83. Derwin KA, Baker AR, Codsí MJ. Assessment of the canine model of rotator cuff injury and repair. *Journal of Shoulder and Elbow Surgery*. 2007;16:S140-S8.
84. Gerber C, Schneeberger AG, Perren SM, Nyffeler RW. Experimental rotator cuff repair. A preliminary study. *The Journal of bone and joint surgery American volume*. 1999;81:1281-90.
85. Sonnabend DH, Howlett CR, Young AA. Histological evaluation of repair of the rotator cuff in a primate model. *The Journal of Bone and Joint Surgery British volume*. 2010;92-B:586-94.
86. Grumet RC, Hadley S, Diltz MV, Lee TQ, Gupta R. Development of a new model for rotator cuff pathology: the rabbit subscapularis muscle. *Acta orthopaedica*. 2009;80:97-103.
87. Liu Y, Fu SC, Leong HT, Ling SK-K, Oh JH, Yung PS-H. Evaluation of animal models and methods for assessing shoulder function after rotator cuff tear: A systematic review. *Journal of Orthopaedic Translation*. 2021;26:31-8.
88. Liu X, Manzano G, Kim HT, Feeley BT. A rat model of massive rotator cuff tears. *J Orthop Res*. Apr 2011;29(4):588-95. Epub 2010/10/16.
89. Derwin KA, Baker AR, Iannotti JP, McCarron JA. Preclinical models for translating regenerative medicine therapies for rotator cuff repair. *Tissue engineering Part B, Reviews*. Feb 2010;16(1):21-30. Epub 2009/08/12.
90. Turner AS. Experiences with sheep as an animal model for shoulder surgery: Strengths and shortcomings. *Journal of Shoulder and Elbow Surgery*. 2007;16:S158-S63.
91. Easley J, Johnson J, Regan D, Hackett E, Romeo AA, Schlegel T, et al. Partial Infraspinatus Tendon Transection as a Means for the Development of a Translational Ovine Chronic Rotator Cuff Disease Model. *Veterinary and Comparative Orthopaedics and Traumatology*. 2020.
92. Coleman SH, Fealy S, Ehteshami JR, MacGillivray JD, Altchek DW, Warren RF, et al. Chronic rotator cuff injury and repair model in sheep. *The Journal of bone and joint surgery American volume*. 2003;85-A:2391-402.

93. L.M. Galatz * SYR, M. Zaegel, M.J. Silva, N. Havlioglu ST. Delayed Repair of Tendon to Bone Injuries Leads to Decreased Biomechanical Properties and Bone Loss. *J Orthop Res.* 2005;23:1441-7.
94. Gerber C, Meyer DC, Schneeberger AG, Hoppeler H, von Rechenberg B. Effect of tendon release and delayed repair on the structure of the muscles of the rotator cuff: an experimental study in sheep. *The Journal of bone and joint surgery American volume.* 2004;86-A:1973-82.
95. Barton ER, Gimbel JA, Williams GR, Soslowsky LJ. Rat supraspinatus muscle atrophy after tendon detachment. *J Orthop Res.* Mar 2005;23(2):259-65. Epub 2005/03/01.
96. Galatz LM, Sandell LJ, Rothermich SY, Das R, Mastny A, Havlioglu N, et al. Characteristics of the rat supraspinatus tendon during tendon-to-bone healing after acute injury. *J Orthop Res.* Mar 2006;24(3):541-50. Epub 2006/02/04.
97. Gerber C, Schneeberger AG, Beck M, Schlegel U. Mechanical strength of repairs of the rotator cuff. *J Bone Joint Surg Br.* May 1994;76(3):371-80. Epub 1994/05/01.
98. Rodeo SA, Potter HG, Kawamura S, Turner AS, Kim HJ, Atkinson BL. Biologic Augmentation of Rotator Cuff Tendon-Healing with Use of a Mixture of Osteoinductive Growth Factors. *The Journal of Bone and Joint Surgery (American).* 2007;89:2485.
99. Lewis CW, Schlegel TF, Hawkins RJ, James SP, Turner AS. Comparison of tunnel suture and suture anchor methods as a function of time in a sheep model. *Biomed Sci Instrum.* 1999;35:403-8. Epub 2001/01/06.
100. C. W. Lewis TFS, R.J. Hawkins, S.P. James, A.S. Turner. The Effect of Immobilization on Rotator Cuff Healing Using Modified Mason-Allen Stitches- A Biomechanical Study in Sheep. *Biomedical Sciences Instrumentation.* 2001:263-8.
101. Schlegel TF, Hawkins RJ, Lewis CW, Turner AS. An in vivo comparison of the modified Mason-Allen suture technique versus an inclined horizontal mattress suture technique with regard to tendon-to-bone healing: A biomechanical and histologic study in sheep. *Journal of Shoulder and Elbow Surgery.* 2007;16:115-21.
102. Luan T, Liu X, Easley JT, Ravishankar B, Puttlitz C, Feeley BT. Muscle atrophy and fatty infiltration after an acute rotator cuff repair in a sheep model. *Muscles, ligaments and tendons journal.* Apr-Jun 2015;5(2):106-12. Epub 2015/08/12.
103. Kang JR, Gupta R. Mechanisms of fatty degeneration in massive rotator cuff tears. *Journal of Shoulder and Elbow Surgery.* 2012;21:175-80.
104. Barbolt TA, Odin M, Léger M, Kangas L, Holste J, Liu SH. Biocompatibility evaluation of dura mater substitutes in an animal model. 2001;23(8):813-20.
105. Gibbons MC, Singh A, Anakwenze O, Cheng T, Pomerantz M, Schenk S, et al. Histological Evidence of Muscle Degeneration in Advanced Human Rotator Cuff Disease. *J Bone Joint Surg Am.* Feb 1 2017;99(3):190-9. Epub 2017/02/02.
106. Smith MM, Sakurai G, Smith SM, Young AA, Melrose J, Stewart CM, et al. Modulation of aggrecan and ADAMTS expression in ovine tendinopathy induced by altered strain. *Arthritis and rheumatism.* Apr 2008;58(4):1055-66. Epub 2008/04/03.
107. Lemmon EA, Locke RC, Szostek AK, Ganji E, Killian ML. Partial-width injuries of the rat rotator cuff heal with fibrosis. *Connective Tissue Research.* 2018/09/03 2018;59(5):437-46.

108. Jacobsen E, Dart AJ, Mondori T, Horadogoda N, Jeffcott LB, Little CB, et al. Focal Experimental Injury Leads to Widespread Gene Expression and Histologic Changes in Equine Flexor Tendons. *PloS one*. 2015;10(4):e0122220.
109. Melrose J, Smith MM, Smith SM, Ravi V, Young AA, Dart AJ, et al. Altered stress induced by partial transection of the infraspinatus tendon leads to perlecan (HSPG2) accumulation in an ovine model of tendinopathy. *Tissue and Cell*. 2013/02/01/ 2013;45(1):77-82.
110. Easley J, Johnson J, Regan D, Hackett E, Romeo AA, Schlegel T, et al. Partial Infraspinatus Tendon Transection as a Means for the Development of a Translational Ovine Chronic Rotator Cuff Disease Model. *Vet Comp Orthop Traumatol*. May 2020;33(3):212-9. Epub 2020/04/02.
111. Longo UG, Franceschi F, Ruzzini L, Rabitti C, Morini S, Maffulli N, et al. Histopathology of the Supraspinatus Tendon in Rotator Cuff Tears. *The American Journal of Sports Medicine*. 2008;36(3):533-8.
112. Gerber C, Pennington SD, Nyffeler RW. Reverse Total Shoulder Arthroplasty. *JAAOS - Journal of the American Academy of Orthopaedic Surgeons*. 2009;17(5):284-95.
113. Vourazeris JD, Wright TW, Struk AM, King JJ, Farmer KW. Primary reverse total shoulder arthroplasty outcomes in patients with subscapularis repair versus tenotomy. *J Shoulder Elbow Surg*. Mar 2017;26(3):450-7. Epub 2016/10/19.
114. Somerson JS, Hsu JE, Gorbaty JD, Gee AO. Classifications in Brief: Goutallier Classification of Fatty Infiltration of the Rotator Cuff Musculature. *Clinical Orthopaedics and Related Research*. 2016;474(5):1328-32.
115. Noyes FR, Butler DL, Grood ES, Zernicke RF, Hefzy MS. Biomechanical analysis of human ligament grafts used in knee-ligament repairs and reconstructions. *J Bone Joint Surg Am*. Mar 1984;66(3):344-52. Epub 1984/03/01.
116. McGilvray KC, Santoni BG, Turner AS, Bogdansky S, Wheeler DL, Puttlitz CM. Effects of ⁶⁰Co gamma radiation dose on initial structural biomechanical properties of ovine bone—patellar tendon—bone allografts. *Cell and Tissue Banking*. 2011;12(2):89-98.
117. E. PAUL FRANCE P, LONNIE E. PAULOS, MD, CHRIS D. HARNER, MD, AND CHRIS B. STRAIGHT, MS. Biomechanical evaluation of rotator cuff fixation methods. *Am J Sports Med*. 1989;17(2):176-81.
118. Schlegel TF, Hawkins RJ, Lewis CW, Motta T, Turner AS. The Effects of Augmentation with Swine Small Intestine Submucosa on Tendon Healing under Tension. *Am J Sports Med*. 2006;34:275-80.
119. Rodeo SA, Arnoczky SP, Torzilli PA, Hidaka C, Warren RF. Tendon-healing in a bone tunnel. A biomechanical and histological study in the dog. *J Bone Joint Surg Am*. Dec 1993;75(12):1795-803. Epub 1993/12/01.
120. Sverdlik A, Lanir Y. Time-Dependent Mechanical Behavior of Sheep Digital Tendons, Including the Effects of Preconditioning. *Journal of Biomechanical Engineering*. 2002;124(1):78-84.
121. Troyer KL, Puttlitz CM. Nonlinear viscoelasticity plays an essential role in the functional behavior of spinal ligaments. *Journal of Biomechanics*. 2012;45(4):684-91.
122. Paxton JZ, Hagerty P, Andrick JJ, Baar K. Optimizing an Intermittent Stretch Paradigm Using ERK1/2 Phosphorylation Results in Increased Collagen Synthesis in Engineered Ligaments. *Tissue Engineering Part A*. 2012;18(3-4):277-84.

123. Liao J, Vesely I. Relationship Between Collagen Fibrils, Glycosaminoglycans, and Stress Relaxation in Mitral Valve Chordae Tendineae. *Annals of Biomedical Engineering*. 2004;32(7):977-83.
124. Sikes KJ, Li J, Gao SG, Shen Q, Sandy JD, Plaas A, et al. TGF- β 1 or hypoxia enhance glucose metabolism and lactate production via HIF1A signaling in tendon cells. *Connect Tissue Res*. Sep 2018;59(5):458-71. Epub 2018/02/16.
125. Kim D, Pertea G, Trapnell C, Pimentel H, Kelley R, Salzberg SL. TopHat2: accurate alignment of transcriptomes in the presence of insertions, deletions and gene fusions. *Genome Biology*. 2013;14(4):R36.
126. Sethi PM, Sheth CD, Pauzenberger L, McCarthy MBR, Cote MP, Sonesson E, et al. Macroscopic Rotator Cuff Tendinopathy and Histopathology Do Not Predict Repair Outcomes of Rotator Cuff Tears. *The American Journal of Sports Medicine*. 2018;46(4):779-85.
127. Nakajima T, Rokuuma N, Hamada K, Tomatsu T, Fukuda H. Histologic and biomechanical characteristics of the supraspinatus tendon: Reference to rotator cuff tearing. *Journal of Shoulder and Elbow Surgery*. 1994;3(2):79-87.
128. Roßbach BP, Gülecüyz MF, Kempfert L, Pietschmann MF, Ullmann T, Ficklscherer A, et al. Rotator Cuff Repair With Autologous Tenocytes and Biodegradable Collagen Scaffold: A Histological and Biomechanical Study in Sheep. *The American Journal of Sports Medicine*. 2020;48(2):450-9.
129. Jelinsky SA, Rodeo SA, Li J, Gulotta LV, Archambault JM, Seeherman HJ. Regulation of gene expression in human tendinopathy. 2011;12(1):86.
130. Ireland D, Harrall R, Curry V, Holloway G, Hackney R, Hazleman B, et al. Multiple changes in gene expression in chronic human Achilles tendinopathy. *Matrix Biology*. 2001;20(3):159-69.
131. Alfredson H, Lorentzon M, Bäckman S, Bäckman A, Lerner UH. cDNA-arrays and real-time quantitative PCR techniques in the investigation of chronic achilles tendinosis. *Journal of Orthopaedic Research*. 2003;21(6):970-5.
132. Seitz AL, McClure PW, Finucane S, Boardman ND, Michener LA. Mechanisms of rotator cuff tendinopathy: Intrinsic, extrinsic, or both? *Clinical Biomechanics*. 2011;26(1):1-12.
133. Dean BJ, Franklin SL, Carr AJ. A systematic review of the histological and molecular changes in rotator cuff disease. *Bone Joint Res*. Jul 2012;1(7):158-66. Epub 2013/04/24.
134. VanBaak K, Aerni G. Shoulder Conditions: Rotator Cuff Injuries and Bursitis. *FP Essent*. Apr 2020;491:11-6. Epub 2020/04/22.
135. Neer CS, 2nd. Anterior acromioplasty for the chronic impingement syndrome in the shoulder: a preliminary report. *J Bone Joint Surg Am*. Jan 1972;54(1):41-50. Epub 1972/01/01.
136. Johnson J, Von Stade D, Regan D, Easley J, Chow L, Dow S, et al. Enthesis trauma as a means for the development of translatable chronic rotator cuff degeneration in an ovine model. *Annals of Translational Medicine*. 2021;9(9):741-.
137. Derwin KA, Galatz LM, Ratcliffe A, Thomopoulos S. Enthesis Repair. *The Journal of Bone and Joint Surgery*. 2018;100(16):e109.
138. Broomfield C, Meis N, Johnson J, Regan D, McGilvray K, Puttlitz C. Optimization of ovine bone decalcification for increased cellular detail: a parametric study. *J Histotechnol*. Aug 12 2021:1-7. Epub 2021/08/13.

139. Zellers JA, Pohlig RT, Cortes DH, Grävare Silbernagel K. Achilles tendon cross-sectional area at 12 weeks post-rupture relates to 1-year heel-rise height. *Knee Surgery, Sports Traumatology, Arthroscopy*. 2020;28(1):245-52.
140. Tuckman GA. Abnormalities of the long head of the biceps tendon of the shoulder: MR imaging findings. *American Journal of Roentgenology*. 1994;163(5):1183-8.
141. Buck FM, Grehn H, Hilbe M, Pfirrmann CWA, Manzanell S, Hodler J. Degeneration of the Long Biceps Tendon: Comparison of MRI With Gross Anatomy and Histology. *American Journal of Roentgenology*. 2009;193(5):1367-75.
142. Gladstone JN, Bishop JY, Lo IK, Flatow EL. Fatty infiltration and atrophy of the rotator cuff do not improve after rotator cuff repair and correlate with poor functional outcome. *Am J Sports Med*. May 2007;35(5):719-28. Epub 2007/03/06.
143. Kirchhoff C, Kirchhoff S, Sprecher CM, Ahrens P, Imhoff AB, Hinterwimmer S, et al. X-treme CT analysis of cancellous bone at the rotator cuff insertion in human individuals with osteoporosis: superficial versus deep quality. *Archives of Orthopaedic and Trauma Surgery*. 2013;133(3):381-7.
144. Kirchhoff C, Braunstein V, Milz S, Sprecher CM, Fischer F, Tami A, et al. Assessment of Bone Quality within the Tuberosities of the Osteoporotic Humeral Head. *The American Journal of Sports Medicine*. 2010;38(3):564-9.
145. Oh JH, Song BW, Kim SH, Choi JA, Lee JW, Chung SW, et al. The measurement of bone mineral density of bilateral proximal humeri using DXA in patients with unilateral rotator cuff tear. *Osteoporosis International*. 2014;25(11):2639-48.
146. Chen X, Giambini H, Ben-Abraham E, An K-N, Nassr A, Zhao C. Effect of Bone Mineral Density on Rotator Cuff Tear: An Osteoporotic Rabbit Model. *PloS one*. 2015;10(10):e0139384.
147. Cadet ER, Vorys GC, Rahman RK, Park S-H, Gardner TR, Lee FY, et al. Improving bone density at the rotator cuff footprint increases supraspinatus tendon failure stress in a rat model. *Journal of Orthopaedic Research*. 2009:n/a-n/a.
148. Black DM, Cummings SR, Karpf DB, Cauley JA, Thompson DE, Nevitt MC, et al. Randomised trial of effect of alendronate on risk of fracture in women with existing vertebral fractures. *The Lancet*. 1996;348(9041):1535-41.
149. James AW, Shen J, Zhang X, Asatrian G, Goyal R, Kwak JH, et al. NELL-1 in the treatment of osteoporotic bone loss. *Nature Communications*. 2015;6(1):7362.
150. Haffner-Luntzer M, Hankenson KD, Ignatius A, Pfeifer R, Khader BA, Hildebrand F, et al. Review of Animal Models of Comorbidities in Fracture-Healing Research. *Journal of Orthopaedic Research*. 2019.
151. Gaytan F, Morales C, Reymundo C, Tena-Sempere M. A novel RGB-trichrome staining method for routine histological analysis of musculoskeletal tissues. *Scientific Reports*. 2020;10(1).
152. Choi S, Kim MK, Kim GM, Roh YH, Hwang IK, Kang H. Factors associated with clinical and structural outcomes after arthroscopic rotator cuff repair with a suture bridge technique in medium, large, and massive tears. *J Shoulder Elbow Surg*. Nov 2014;23(11):1675-81. Epub 2014/05/28.
153. Fearon A, Dahlstrom JE, Twin J, Cook J, Scott A. The Bonar score revisited: Region of evaluation significantly influences the standardized assessment of tendon degeneration. *Journal of Science and Medicine in Sport*. 2014;17(4):346-50.

154. Thomopoulos S, Genin GM, Galatz LM. The development and morphogenesis of the tendon-to-bone insertion - what development can teach us about healing. *J Musculoskeletal Neuronal Interact.* Mar 2010;10(1):35-45. Epub 2010/03/02.
155. Troyer KL, Puttlitz CM. Human cervical spine ligaments exhibit fully nonlinear viscoelastic behavior. *Acta Biomater.* Feb 2011;7(2):700-9. Epub 2010/09/14.
156. Landis JR, Koch GG. The measurement of observer agreement for categorical data. *Biometrics.* Mar 1977;33(1):159-74. Epub 1977/03/01.
157. Doschak MR, Lamothe JM, Cooper DML, Hallgrímsson B, Hanley DA, Bray RC, et al. Bisphosphonates reduce bone mineral loss at ligament entheses after joint injury. *Osteoarthritis and Cartilage.* 2005;13(9):790-7.
158. Shah SA, Kormpakis I, Havlioglu N, Ominsky MS, Galatz LM, Thomopoulos S. Sclerostin Antibody Treatment Enhances Rotator Cuff Tendon-to-Bone Healing in an Animal Model. *Journal of Bone and Joint Surgery.* 2017;99(10):855-64.
159. Thomopoulos S, Matsuzaki H, Zaegel M, Gelberman RH, Silva MJ. Alendronate prevents bone loss and improves tendon-to-bone repair strength in a canine model. *Journal of Orthopaedic Research.* 2007;25(4):473-9.
160. Kim DM, Shim IK, Shin MJ, Choi JH, Lee YN, Jeon I-H, et al. A Combination Treatment of Raloxifene and Vitamin D Enhances Bone-to-Tendon Healing of the Rotator Cuff in a Rat Model. *The American Journal of Sports Medicine.* 2020;48(9):2161-9.
161. Schanda JE, Keibl C, Heimel P, Monforte X, Tangl S, Feichtinger X, et al. Zoledronic Acid Substantially Improves Bone Microarchitecture and Biomechanical Properties After Rotator Cuff Repair in a Rodent Chronic Defect Model. *The American Journal of Sports Medicine.* 2020;48(9):2151-60.
162. Tipton DA, Seshul BA, Dabbous MK. Effect of bisphosphonates on human gingival fibroblast production of mediators of osteoclastogenesis: RANKL, osteoprotegerin and interleukin-6. *Journal of Periodontal Research.* 2011;46(1):39-47.
163. Ziebart T, Halling F, Heymann P, Neff A, Blatt S, Jung J, et al. Impact of Soft Tissue Pathophysiology in the Development and Maintenance of Bisphosphonate-Related Osteonecrosis of the Jaw (BRONJ). *Dentistry Journal.* 2016;4(4):36.
164. Manzano-Moreno FJ, Illescas-Montes R, Melguizo-Rodríguez L, Costela-Ruiz VJ, García-Martínez O, Ruiz C, et al. Impact of bisphosphonates on the proliferation and gene expression of human fibroblasts. *International Journal of Medical Sciences.* 2019;16(12):1534-40.
165. Jones IA, Togashi R, Hatch GFR, Weber AE, Vangsnæs CT. Anabolic steroids and tendons: A review of their mechanical, structural, and biologic effects. *Journal of Orthopaedic Research®.* 2018;36(11):2830-41.
166. Blomgran P, Hammerman M, Aspenberg P. Systemic corticosteroids improve tendon healing when given after the early inflammatory phase. *Scientific Reports.* 2017;7(1).
167. Agrawal D, Dougherty K, Dilisio M. Vitamin D and the immunomodulation of rotator cuff injury. *Journal of Inflammation Research.* 2016:123.
168. Angeline ME, Ma R, Pascual-Garrido C, Voigt C, Deng XH, Warren RF, et al. Effect of Diet-Induced Vitamin D Deficiency on Rotator Cuff Healing in a Rat Model. *The American Journal of Sports Medicine.* 2014;42(1):27-34.
169. Torricelli P, Veronesi F, Pagani S, Maffulli N, Masiero S, Frizziero A, et al. In vitro tenocyte metabolism in aging and oestrogen deficiency. *AGE.* 2013;35(6):2125-36.

170. Fryhofer GW, Freedman BR, Hillin CD, Salka NS, Pardes AM, Weiss SN, et al. Postinjury biomechanics of Achilles tendon vary by sex and hormone status. *Journal of Applied Physiology*. 2016;121(5):1106-14.
171. Minagawa H, Yamamoto N, Abe H, Fukuda M, Seki N, Kikuchi K, et al. Prevalence of symptomatic and asymptomatic rotator cuff tears in the general population: From mass-screening in one village. *Journal of Orthopaedics*. 2013;10(1):8-12.
172. Iannotti JP, Codsí MJ, Kwon YW, Derwin K, Ciccone J, Brems JJ. Porcine small intestine submucosa augmentation of surgical repair of chronic two-tendon rotator cuff tears. A randomized, controlled trial. *J Bone Joint Surg Am*. Jun 2006;88(6):1238-44. Epub 2006/06/08.
173. Walton JR, Bowman NK, Khatib Y, Linklater J, Murrell GA. Restore orthobiologic implant: not recommended for augmentation of rotator cuff repairs. *J Bone Joint Surg Am*. Apr 2007;89(4):786-91. Epub 2007/04/04.
174. Soler JA, Gidwani S, Curtis MJ. Early complications from the use of porcine dermal collagen implants (Permacol) as bridging constructs in the repair of massive rotator cuff tears. A report of 4 cases. *Acta Orthop Belg*. Aug 2007;73(4):432-6. Epub 2007/10/18.
175. Wang JHC, Guo Q, Li B. Tendon Biomechanics and Mechanobiology—A Minireview of Basic Concepts and Recent Advancements. *Journal of Hand Therapy*. 2012;25(2):133-41.
176. Zhang J, Wang JHC. Mechanobiological response of tendon stem cells: Implications of tendon homeostasis and pathogenesis of tendinopathy. *Journal of Orthopaedic Research*. 2010;28(5):639-43.
177. Zhang J, Wang JHC. Production of PGE2 increases in tendons subjected to repetitive mechanical loading and induces differentiation of tendon stem cells into non-tenocytes. *Journal of Orthopaedic Research*. 2009:n/a-n/a.
178. Langberg H, Rosendal L, Kjær M. Training-induced changes in peritendinous type I collagen turnover determined by microdialysis in humans. *The Journal of Physiology*. 2001;534(1):297-302.
179. Zhang J, Pan T, Liu Y, Wang JHC. Mouse treadmill running enhances tendons by expanding the pool of tendon stem cells (TSCs) and TSC-related cellular production of collagen. *Journal of Orthopaedic Research*. 2010;28(9):1178-83.
180. Soslowky LJ, Thomopoulos S, Esmail A, Flanagan CL, Iannotti JP, Williamson IJD, et al. Rotator Cuff Tendinosis in an Animal Model: Role of Extrinsic and Overuse Factors. *Annals of Biomedical Engineering*. 2002;30(8):1057-63.
181. Parks AN, McFaline-Figueroa J, Coogan A, Poe-Yamagata E, Guldberg RE, Platt MO, et al. Supraspinatus tendon overuse results in degenerative changes to tendon insertion region and adjacent humeral cartilage in a rat model. *Journal of Orthopaedic Research*. 2017;35(9):1910-8.
182. Newton JB, Fryhofer GW, Rodriguez AB, Kuntz AF, Soslowky LJ. Mechanical properties of the different rotator cuff tendons in the rat are similarly and adversely affected by age. *Journal of Biomechanics*. 2021;117:110249.
183. Johnson GA, Tramaglino DM, Levine RE, Ohno K, Choi N-Y, L-Y. Woo S. Tensile and viscoelastic properties of human patellar tendon. *Journal of Orthopaedic Research*. 1994;12(6):796-803.
184. Maganaris CN, Paul JP. In vivo human tendon mechanical properties. *The Journal of Physiology*. 1999;521(1):307-13.

185. Kempf J-F, Gleyze P, Bonnomet F, Walch G, Mole D, Frank A, et al. A Multicenter Study of 210 Rotator Cuff Tears Treated by Arthroscopic Acromioplasty. *Arthroscopy: The Journal of Arthroscopic & Related Surgery*. 1999;15(1):56-66.
186. Shim SB, Jeong JY, Yum TH, Yoo JC. A Comparative Study to Evaluate the Risk Factors for Medium-Sized Rotator Cuff Tear in Patients Younger Than 50 Years of Age. *Arthroscopy : the journal of arthroscopic & related surgery : official publication of the Arthroscopy Association of North America and the International Arthroscopy Association*. Nov 2018;34(11):2971-9. Epub 2018/11/06.
187. Khazzam M, Sager B, Box HN, Wallace SB. The effect of age on risk of retear after rotator cuff repair: a systematic review and meta-analysis. *JSES Int*. Sep 2020;4(3):625-31. Epub 2020/09/18.
188. Johnson J vSD, Regan D, Easley J., Chow L DS, Romeo T, Schlegel T, McGilvray K. Tendon midsubstance trauma as a means for the development of translatable chronic rotator cuff degeneration in an ovine model. *Ann Translation Medicine*. 2021.
189. Maffulli N, Barrass V, Ewen SWB. Light Microscopic Histology of Achilles Tendon Ruptures. *The American Journal of Sports Medicine*. 2000;28(6):857-63.
190. Miller RM, Thunes J, Maiti S, Musahl V, Debski RE. Effects of Tendon Degeneration on Predictions of Supraspinatus Tear Propagation. *Annals of Biomedical Engineering*. 2019;47(1):154-61.
191. Sano H, Ishii H, Yeadon A, Backman DS, Brunet JA, Uhthoff HK. Degeneration at the insertion weakens the tensile strength of the supraspinatus tendon: A comparative mechanical and histologic study of the bone-tendon complex. *Journal of Orthopaedic Research*. 1997;15(5):719-26.
192. Nourissat G, Berenbaum F, Duprez D. Tendon injury: from biology to tendon repair. *Nature Reviews Rheumatology*. 2015/04/01 2015;11(4):223-33.
193. Lejard V, Blais F, Guerquin M-J, Bonnet A, Bonnin M-A, Havis E, et al. EGR1 and EGR2 Involvement in Vertebrate Tendon Differentiation. *Journal of Biological Chemistry*. 2011;286(7):5855-67.
194. Scott A, Sampaio A, Abraham T, Duronio C, Underhill TM. Scleraxis expression is coordinately regulated in a murine model of patellar tendon injury. *Journal of Orthopaedic Research*. 2011;29(2):289-96.
195. Liu W, Watson SS, Lan Y, Keene DR, Ovitt CE, Liu H, et al. The Atypical Homeodomain Transcription Factor Mohawk Controls Tendon Morphogenesis. *Molecular and Cellular Biology*. 2010;30(20):4797-807.
196. Page M, Baer K, Schon B, Mekhileri N, Woodfield T, Puttlitz C. Biaxial mechanics of 3D fiber deposited ply-laminate scaffolds for soft tissue engineering part I: Experimental evaluation. *Journal of the Mechanical Behavior of Biomedical Materials*. 2019;98:317-26.
197. Page M, Puttlitz C. Biaxial mechanics of 3D fiber deposited ply-laminate scaffolds for soft tissue engineering part II: Finite element analyses. *Journal of the Mechanical Behavior of Biomedical Materials*. 2019;100:103395.
198. Loppini M, Longo UG, Niccoli G, Khan WS, Maffulli N, Denaro V. Histopathological scores for tissue-engineered, repaired and degenerated tendon: a systematic review of the literature. *Current stem cell research & therapy*. 2015;10(1):43-55. Epub 2014/07/12.